Evidence for Electroweak Production of $W^{\pm}W^{\pm}jj$ in Proton-Proton Collisions at $\sqrt{s} = 8$ TeV with the ATLAS Detector at the LHC

by

Lulu Liu

A dissertation submitted in partial fulfillment
of the requirements for the degree of
Doctor of Philosophy
(Physics)
in the University of Michigan
2015

Doctoral Committee:

Assistant Professor Junjie Zhu, Chair
Professor Gordon L. Kane
Professor Bing Zhou
Professor Ji Zhu

2015

ACKNOWLEDGMENTS

Doing a physics PhD is in many ways like running a marathon. I have now come to the finish line and I would like to thank all the people who have helped me getting here. First and foremost, I would like to thank my advisor Prof. Junjie Zhu. I started working with Junjie in the summer of 2010 and it has been an amazing ride since. His instructions, encouragement and patience have always been a source of energy and navigation. Special thanks go to Prof. Bing Zhou, who is always willing to listen to my problems and give me advice and whom I have always considered a mentor. I have had the privilege to collaborate with many excellent colleagues over a few projects, whom I constantly get inspired by and learn from. They are Tiesheng Dai, Jianbei Liu, Jake Searcy, Sara Borroni, Christian Gumpert, Ulrike Schnoor, Phillip Anger, Anja Vest, Michael Kobel, Alex Sood, Simone Pagan Griso, Marc-Andre Pleier, Jessica Metcalfe, Merlin Davies, Peter Loscutoff, Georges Azuelos and Huilin Wang. I would like to thank Bob Ball, Shawn McKee and Ben Meekhof, who have maintained a wonderful computing facility in our group without which I would not have run a single analysis job. I would like to thank my fellow runners along the way, who have shared with me and shouldered together all the stress, frustration and confusion about being a graduate student: Jiaming Yu, Yusheng Wu, Haolu Feng, Xiaoxiao Wang, Diedi Hu, Mingming Yang and many others. Last but not least, I would like to thank my parents, who always have faith in me and support me no matter what adventures I head for.

TABLE OF CONTENTS

Acknowledgments . . . . . **ii**

List of Figures . . . . . **v**

List of Tables . . . . . **xi**

List of Appendices . . . . . **xiv**

List of Abbreviations . . . . . **xv**

Abstract . . . . . **xvii**

Chapter

Introduction **1**

1 Theory **2**

1.1 The Standard Model 2
1.2 Gauge Boson and Higgs Interactions 3
1.3 Vector Boson Scattering 9
1.4 Anomalous Quartic Gauge Coupling 11

2 The LHC and ATLAS **13**

2.1 The Large Hadron Collider 13
2.2 The ATLAS Detector 14
2.2.1 The Coordinate System 15
2.2.2 Magnet System 16
2.2.3 Inner Detector 16
2.2.4 Calorimeters 18
2.2.5 Muon Spectrometer 21
2.2.6 Trigger System 22

3 Object Reconstruction and Identification **24**

3.1 Electrons 24
3.2 Muons 26
3.3 Jets 28
3.4 Missing Transverse Energy 31
3.5 Flavor Tagging 32

4 $W^{\pm}W^{\pm}jj$ Cross Section Measurement **34**

4.1 Introduction . . . 34
4.2 Data Set . . . 36
4.3 Signal Simulation . . . 37
4.4 Event Selection . . . 38
4.4.1 Fiducial Signal Region Definition . . . 38
4.4.2 Reconstructed Vertices and Pileup Correction . . . 39
4.4.3 Muons . . . 39
4.4.4 Electrons . . . 40
4.4.5 Jets . . . 41
4.4.6 Missing Transverse Energy . . . 42
4.4.7 Overlapping Object Treatment . . . 42
4.4.8 Signal Region Definition . . . 43
4.5 Signal Production Cross Section in Fiducial Regions . . . 44
4.5.1 $W^{\pm}W^{\pm}jj$-Ewk . . . 44
4.6 Background Estimation . . . 49
4.6.1 Charge Mis-ID Backgrounds . . . 50
4.6.2 Non-prompt Backgrounds . . . 59
4.6.3 Prompt Backgrounds . . . 72
4.6.4 Low m_{jj} Control Region . . . 76
4.7 Systematic Uncertainty . . . 77
4.8 Signal Regions . . . 80
4.9 Cross Section Measurement . . . 84
4.10 aQGC Limits . . . 87

5 Conclusion and Outlook . . . 92

Appendices . . . 94

Bibliography . . . 109

LIST OF FIGURES

1.1 The Higgs potential as a function of $\sqrt{\Phi^\dagger\Phi}$ for the case of $\mu^2 > 0$ and $\mu^2 < 0$. 6
1.2 The s-channel (left) and t-channel (right) VBS processes involving TGC. 9
1.3 VBS processes involving QGC. 9
1.4 VBS processes involving Higgs boson. 9
1.5 The projection of a real amplitude $a(s)$ onto the Argand circle. 12

2.1 The LHC accelerator complex. 13
2.2 The four collision points at LHC. 14
2.3 The ATLAS detector. 15
2.4 Magnetic field integral along trajectories in the ATLAS detector with $\phi = 0$ (red) and $\phi = \pi/8$ (black) as a function of η for infinite-momentum muons. 17
2.5 Layout of the ATLAS inner detector. 17
2.6 The ATLAS calorimeter system. 19
2.7 Total amount of material before and in the EM calorimeter in units of EM radiation length. 20
2.8 Total amount of material before the first active layer of the muon system in units of nuclear interaction length. 20
2.9 Layout of a quarter of the muon system. The MDT's are shown in green color in the barrel and blue color in the endcap. The CSC's, TGC's and RPC's are marked in the plot. 21
2.10 Schematic of the ATLAS trigger system. 23

3.1 Different interactions between final state objects and the detector. 25
3.2 Electron reconstruction efficiencies as a function of the electron E_{T} (left) integrated over the whole η range and η (right) for electrons with 15 GeV $< p_{\mathrm{T}} <$ 50 GeV. An improvement in the 2012 run is due to a new track reconstruction algorithm and improved track-cluster matching. . . 26
3.3 Electron energy scale correction factor and its uncertainty as a function of E_{T} for electrons with $|\eta| < 0.6$ (left) and electron energy resolution and its uncertainty as a function of E_{T} for electrons with $|\eta| = 0.2$. . . . 26
3.4 Measured combined electron reconstruction and identification efficiencies as a function of the electron E_{T} (left) and η (right). Here "LH" stands for "likelihood" and marks the multivariate-based menus. Only the cut-based "loose" and "tight" menus are used in this thesis. 27

3.5 Muon reconstruction efficiencies measured in data and simulated $Z \to \mu\mu$ events as a function of η for different muon types (Chain 1). The significant drop in the range $1.0 < \eta < 1.3$ is due to some missing MS chambers not installed until after the 2012 data run. 28
3.6 Muon reconstruction efficiencies measured in data and simulated $Z \to \mu\mu$ events as a function of p_{T} for CB muons alone (left) and CB+ST muons combined (right). 29
3.7 Di-muon invariant mass distribution for $Z \to \mu\mu$ reconstructed using CB muons (left) and the mass resolution as a function of the leading-p_{T} muon η (right). 29
3.8 Uncertainties on the jet energy scale for central jets with $|\eta| = 0.5$ (left) and forward jets with $|\eta| = 2.0$ (right). 30
3.9 Fractional jet energy resolution as a function of the average jet transverse momenta measured with di-jet events. The errors are statistical uncertainties only. 31
3.10 E_x^{miss} and E_y^{miss} resolution as a function of the E_{T} sum of the event for minimum biase events in 2012 data without 20 GeV jets (left) and inclusively (right). Improvement is observed after introducing pileup suppression techniques. 32
3.11 The tagging efficiency for b-jets using the MV1 tagging tool at the 70% efficiency operating point as a function of the b-jet p_{T}. 33
3.12 The mis-tag rate for light jets using the MV1 tagging tool at the 70% efficiency operating point as a function of the jet p_{T} for jets with $|\eta| < 1.2$ (left) and $1.2 < |\eta| < 2.5$ (right). 33

4.1 Feynman diagrams of VBS production at the LHC. All these diagrams have $\mathcal{O}(\alpha_{\mathrm{EW}}^6)$ dependence. The s-channel diagrams do not exist for same-sign $W^{\pm}W^{\pm}jj$ final state. 34
4.2 Non-VBS production of the $VVjj$ final state with $\mathcal{O}(\alpha_{\mathrm{EW}}^6)$. The first two diagrams from the left are not gauge-invariantly seperable from VBS production. The two diagrams on the right (tri-W production and non-resonant production) can be suppressed in the event selections. This list is not exaustive but more diagrams exist than displayed here. . 35
4.3 Strong production of the $VVjj$ final state with $\mathcal{O}(\alpha_{\mathrm{EW}}^4)\mathcal{O}(\alpha_{\mathrm{S}}^2)$. This list is not exaustive but more diagrams exist than displayed here. The gluon-quark and gluon-gluon initial state diagrams do not exist for same-sign $W^{\pm}W^{\pm}jj$ final state. 35
4.4 VBS event topology in the ATLAS detector. 35
4.5 Generator-level comparison between electroweak and strong production of $W^{\pm}W^{\pm}jj$. Here the rapidity separation (left) and invariant mass (right) of the two leading jets are shown. All histograms are normalized to unity area. The electroweak production has a clear feature of large rapidity separation and high di-jet invariant mass, which is characteristic for VBS. 36

4.6 A hard photon is radiated off an electron and later converts to a pair of electrons. The light blue box represents the material in the inner detector which is needed for the radiation and photon conversion to happen. Only the final positron is matched to the original electron track and eventually reconstructed as a positron. The other two electrons are not reconstructed due to low momentum. 51
4.7 The electron charge mis-ID rate as a function of p_{T} and η (left) and as a function of η (right). 52
4.8 The charge mis-ID rate in the MC sample measured using the likelihood method and derived using truth level information. The uncertainties are statistical only and should be considered fully correlated since the same MC sample is used for deriving both. 53
4.9 The difference between the truth electron energy and the reconstructed electron energy for electrons with correct charge measurement (Good), electrons with wrong charge measurement through photon conversion (Trident) and electrons with wrong charge measurement not through photon conversion (Mismeasured). 54
4.10 Electron energy loss correction parameters: linear shift term (left) and resolution smearing term (right). The unit of the y-axis is GeV. 55
4.11 Di-electron invariant mass distribution for opposite-sign events (dashed curve), same-sign events (red) and opposite-sign events after applying the energy loss correction (blue). 56
4.12 The m_{ee} distribution of selected same-sign ee data sample and charge mis-ID prediction using opposite-sign sample. In the left plot, energy loss correction derived using MC $Z \rightarrow ee$ sample is applied to the opposite-sign sample for prediction. In the right plot, the energy shift term E_{bias} and smearing term $E_{\Delta\mathrm{res}}$ is increased by 35% and 25% respectively to bring the prediction in better agreement with data. 58
4.13 The di-electron invariant mass (m_{ee}) distribution (top left), leading-p_{T} lepton η distribution (top right), subleading-p_{T} lepton η distribution (bottom left) in the Low N_{jet} Charge Mis-ID CR and the number of jets (N_{jet}) distribution in the Same-Sign Inclusive CR. The process shown in yellow is the charge mis-ID background estimated using the opposite-sign control sample. 60
4.14 The event topology of a tight electron+loose muon event (left) and a jet+loose muon event (right). 63
4.15 Average tagging jet p_{T} versus loose lepton $p_{\mathrm{T}} + E_{\mathrm{T}}^{\mathrm{cone30}}$ for jet+loose muon events (left) and jet+loose electron events (right). The error bar is the RMS of the tagging jet p_{T} in each bin of the loose lepton $p_{\mathrm{T}} + E_{\mathrm{T}}^{\mathrm{cone30}}$. 64
4.16 The tagging jet p_{T} distribution from the di-jet sample and the derived underlying jet p_{T} distribution from tight+loose sample for electrons (left) and muons (right). The derived underlying jet p_{T} distribution is obtained after the $N_{jet} \geq 2$ cut in the ee and $\mu\mu$ channel. 65

4.17 The $p_{\mathrm{T}}^{\mathrm{cone30}}/p_{\mathrm{T}}$ and $E_{\mathrm{T}}^{\mathrm{cone30}}/p_{\mathrm{T}}$ distributions for loose electrons (top) and loose muons (bottom). Distributions shown are for the di-jet sample without reweighting, the di-jet sample with tagging jet p_{T} reweighting, and the tight+loose sample. After the reweighting, good agreement is observed between the di-jet sample and the tight+loose sample. The distributions for the tight+loose sample are obtained after the $N_{jet} \geq 2$ cut. 66
4.18 Fake factors measured using reweighted di-jet sample for electrons (top) and muons (bottom) as a function of the lepton p_{T} and η. The error bar contains only the statistical uncertainty. 67
4.19 Fake factors as a function of the lepton p_{T} for electrons (left) and muons (right) with the prompt background estimation varied by 4% and 12% respectively. The fake factor for muons in the high-p_{T} region is consistent with zero given the uncertainties. 68
4.20 Fake factors as a function of the lepton p_{T} for electrons (left) and muons (right) with the tagging jet p_{T} cut value varied by 5 GeV. 68
4.21 Fake factors as a function of the lepton p_{T} for electrons (left) and muons (right) with the mapping slope varied by 15% in deriving the underlying jet p_{T} distribution in the tight+loose sample. 69
4.22 Fake factors as a function of the lepton p_{T} for electrons (left) and muons (right) with statistical uncertainties (inner error bar) and statistical and systematic uncertainties combined (outer error bar). 69
4.23 The trigger efficiency scale factors for tight e+loose e events (top left), tight e+loose μ events (top right), tight μ+loose e events (bottom left) and tight μ+loose μ events (bottom right). The scale factors are shown as a function of the loose lepton p_{T} (labeled here as *Bad Lepton* p_{T}) and tight lepton p_{T} (labeled as *Good Lepton* p_{T}. 70
4.24 Trigger efficiencies measured in W+jets and $t\bar{t}$ MC samples for loose electrons (top left) and loose muons (top right) and trigger efficiencies measured in Z+jets and $t\bar{t}$ MC samples for tight electrons and muons (bottom). 71
4.25 The leading lepton p_{T} distribution (left) and the sub-leading lepton p_{T} distribution (right) in the Top Control Region. The non-prompt background dominates the low p_{T} region. The error band includes all statistical and systematic uncertainties. 73
4.26 The m_{jj} (left) and $\Delta y(jj)$ (right) distributions in the Tri-lepton CR. . . . 76
4.27 The $\Delta y(jj)$ distribution in the Low m_{jj} CR. 77
4.28 The leading-p_{T} and sub-leading-p_{T} jet η distribution in the Low m_{jj} CR. 78
4.29 The leading-p_{T} and sub-leading-p_{T} lepton η distribution in the Low m_{jj} CR. 78

4.30 The m_{jj} distribution in ee, $e\mu$, $\mu\mu$ and combined channels before the $m_{jj} > 500$ GeV cut and the $\Delta y(jj) > 2.4$ cut. The dashed line marks the position of 500 GeV. The region on the right to the dashed line is defined as the Inclusive Signal Region. In the plot for the combined channel, the ratio of data over background only is shown in the bottom. As the m_{jj} gets large, the ratio deviates from one, indicating the background only assumption does not describes the data any more. After adding the signal expectation in, the gap between the background and data is nicely filled. 83
4.31 The $\Delta y(jj)$ distribution in ee, $e\mu$, $\mu\mu$ and combined channels in the Inclusive Signal Region. The dashed line marks the position of 2.4. The region on the right to the dashed line is defined as the VBS Signal Region. As can be seen from the plots, the cut $\Delta y(jj) > 2.4$ helps further remove the $W^{\pm}W^{\pm}jj$-Strong production. 84
4.32 The lepton centrality (ξ) distribution for the combined channel in the Inclusive Signal Region (left) and the VBS Signal Region (right). The $\Delta y(jj) > 2.4$ cut applied for the VBS Signal Region has caused the ζ distribution for the background to shift towards the positive direction. 85
4.33 The $m_{\mathrm{T}}(\ell, \ell, E_{\mathrm{T}}^{\mathrm{miss}})$ distribution for the combined channel in the VBS Signal Region. In the highest bin (including overflow), 6 events are observed and 4 events are expected. 85
4.34 Production cross section of $W^{\pm}W^{\pm}jj$-Electroweak plus the interference term in the VBS Fiducial SR as a function of the aQGC parameters α_4 and α_5. 88
4.35 Detector efficiency for aQGC in ee (top left), $e\mu$ (top right) and $\mu\mu$ (bottom) channel as a function of the fiducial cross section. 90
4.36 Exclusion limits on aQGC parameters (α_4, α_5). The limit contour is obtained by mapping the upper limit on the fiducial cross section onto the (α_4, α_5) plane. Points outside the light blue ellipse are excluded at 95% CL. Points outside the dark blue ellipse are excluded at 68% CL. The expected 95% CL exclusion is given by the solid line. 91

5.1 Summary of SM production cross section measurements at ATLAS, as of July 2014. 92

B.1 The `EF_mu24_tight` trigger efficiency with respect to the tight (left) and loose (right) muon definitons. 98
B.2 The ratio between the `EF_mu24_tight` trigger efficiencies with respect to the loose and tight muon definitons. 98
B.3 From top to bottom: the tagging jet p_{T} and Z p_{T}, the $E_{\mathrm{T}}^{\mathrm{cone30}}/p_{\mathrm{T}}$ and $p_{\mathrm{T}}^{\mathrm{cone30}}/p_{\mathrm{T}}$ for the di-jet, Z+jets and tight+loose sample. The plots for muons are on the left and the electron on the right. The tight+loose sample is after the $N_{jet} \geq 2$ cut as in the nominal analysis. 100

B.4 The loose lepton $E_{\mathrm{T}}^{\mathrm{cone30}}/p_{\mathrm{T}}$ and $p_{\mathrm{T}}^{\mathrm{cone30}}/p_{\mathrm{T}}$ distributions for the di-jet, Z+jets and tight+loose sample after the tagging jet p_{T} distribution in the di-jet sample is reweighted to the Z boson p_{T} distribution in the Z+jets sample. These plots indicate that it is important to have the right jet kinematics for the fake factor measurement. 101
B.5 The $\Delta\phi(\ell, j)$ distribution of jet+tight lepton events after all di-jet selections but the $m_{\mathrm{T}}(\ell, E_{\mathrm{T}}^{\mathrm{miss}})$ <40 GeV cut. The region $\Delta\phi < 2.0$ is defined as the control region for W+jets and Z+jets contribution. The error band corresponds to a 4% uncertainty for jet+tight electron channel and 12% uncertainty for jet+tight muon channel. 102
B.6 The $m_{\mathrm{T}}(\ell, E_{\mathrm{T}}^{\mathrm{miss}})$ distribution of the jet+tight lepton events after all other selection cuts. 103
B.7 The $m_{\mathrm{T}}(\ell, E_{\mathrm{T}}^{\mathrm{miss}})$ distribution of the jet+tight lepton events after all other selection cuts. 103
B.8 The $m_{\mathrm{T}}(\ell, E_{\mathrm{T}}^{\mathrm{miss}})$ distribution of the jet+tight lepton events after all other selection cuts. 104
B.9 The truth underlying jet p_{T} distributions for non-prompt electrons and muons. 104
B.10 The fake factors using the MC samples without any jet p_{T} reweighting. 105
B.11 The fake factors measured using the di-jet and W+jets MC samples. The truth underlying jet p_{T} distribution of the di-jet sample has been reweighted to that of the W+jets sample for electron events and muon events respectively. In the di-jet sample, the jet p_{T} threshold has been required to be larger than 40 (35) GeV for muon (electron) events to further suppress the low p_{T} jet events. The overall fake factor as a flat number in the di-jet sample is 0.012 $\pm$ 0.005 (stat.) for electrons and 0.003 $\pm$ 0.001 for muons. The overall fake factor as a flat number in the W+jets sample is 0.014 $\pm$ 0.002 (stat.) for electrons and 0.014 $\pm$ 0.003 for muons. 105
B.12 The fake factors measured using the di-jet and $t\bar{t}$ MC samples. The truth underlying jet p_{T} distribution of the di-jet sample has been reweighted to that of the $t\bar{t}$ sample for electron events and muon events respectively. In the di-jet sample, the jet p_{T} threshold has been required to be larger than 40 (35) GeV for muon (electron) events to further suppress the low p_{T} jet events. The overall fake factor as a flat number in the di-jet sample is 0.007 $\pm$ 0.002 (stat.) for electrons and 0.003 $\pm$ 0.001 for muons. The overall fake factor as a flat number in the $t\bar{t}$ sample is 0.010 $\pm$ 0.001 (stat.) for electrons and 0.0018 $\pm$ 0.0002 for muons. 106
B.13 The averaged truth underlying jet p_{T} versus the lepton $p_{\mathrm{T}} + E_{\mathrm{T}}^{\mathrm{cone30}}$. . . 107
B.14 The truth underlying jet p_{T} distribution and the derived underlying jet p_{T} distribution using the mapping with different slopes. 108

LIST OF TABLES

1.1 Leptons and quarks. 3
1.2 Gauge bosons and the Higgs boson. 3
1.3 Feynman rules for the gauge and Higgs interactions. The momenta and charge flow into the vertex. We have defined $\mathcal{C}_{\mu\nu\rho}(p,q,r) \equiv g_{\mu\nu}(q-p)_\sigma + g_{\mu\sigma}(p-r)_\nu + g_{\nu\sigma}(r-q)_\mu$ and $\mathcal{Q}_{\mu\nu\rho\sigma} = 2g_{\mu\nu}g_{\rho\sigma} - g_{\mu\rho}g_{\nu\sigma} - g_{\mu\sigma}g_{\nu\rho}$. . 8

4.1 Production cross sections of different $VVjj$ final states at 8 TeV and the ratio between the electroweak and strong production. The calculation is done using SHERPA MC generator at leading order. Two generator-level leptons with $p_{\mathrm{T}} > 5$ GeV are required with the dilepton invariant mass $m_{\ell\ell} > 4$ GeV. At least two jets with $p_{\mathrm{T}} > 10$ GeV are required. . . . 36
4.2 Production cross sections of electroweak $W^\pm W^\pm jj$ in fiducial signal regions calculated at NLO parton level using VBFNLO and POWHEG-BOX without parton showering. Only the $e^\pm\mu^\pm$ final state is included here. 44
4.3 NLO production cross section of electroweak $W^\pm W^\pm jj$ in the two fiducial signal regions calculated using POWHEG-BOX at parton level and particle level using different parton shower models. The $e^\pm\mu^\pm$ final state is used for the calculation and a factor of two has been multiplied to account for other final states, excluding the tau final states. The LO cross sections calculated using SHERPA at parton level and particle level are also shown for comparison. 45
4.4 Fiducial cross section at NLO parton level with the nominal dynamic renormalization scale varied by a factor of ξ_R and the factorization scale varied by a factor of ξ_F. The cross section is for $e^\pm e^\pm$ final state only. The largest deviation from the nominal setup ($\xi_R = \xi_F = 1$) among all combinations, excluding the case when two scales are varied in opposite directions, is given in the bottom row in percentage. 45
4.5 PDF uncertainties on the $W^\pm W^\pm jj$-Ewk production cross section in fiducial regions due to CT10 eigenvector variations. The difference between CT10 and MSTW2008 is also shown for comparison but not quoted as systematic uncertainty. 46
4.6 Summary of systematic uncertainties on $W^\pm W^\pm jj$-Ewk production cross sections in the two fiducial regions. 46
4.7 Summary of systematic uncertainties on $W^\pm W^\pm jj$-Strong production cross sections in the two fiducial regions. 47

4.8 Inclusive, electroweak and strong production of $W^{\pm}W^{\pm}jj$. The interference term is calculated as the difference between the inclusive production and the sum of electroweak and strong pdocutions. Only the $e^{+}\mu^{+}$ final state is included in this table. 49
4.9 Expected and observed numbers of events in different control regions. Only statistical uncertainties for the charge mis-ID estimation are shown in the second column. The combined statistical and systematic uncertainties are shown for other backgrounds in the third column. The Expected/Observed ratio in the last column has included all systematic uncertainties of charge mis-ID estimation as described in the previous section. 59
4.10 Estimated charge mis-ID background yield in the two signal regions. Statistical and systematic uncertainties are also given. 60
4.11 Expected and observed numbers of events in Top Control Region. The non-prompt background makes up 17% to 40% of the total background in different channels. Good agreement is observed between data and expectation. 72
4.12 Number of events subtracted for loose+loose, prompt and charge mis-ID contributions from the tight+loose estimation. 73
4.13 Expected non-prompt background contributions to the signal regions. Both statistical and systematic uncertainties are given. 73
4.14 Summary of systematic uncertainties on $W^{\pm}Zjj$-Ewk (without b-quark in the initial state) production cross sections in the two fiducial regions. 74
4.15 Summary of systematic uncertainties on $W^{\pm}Zjj$-Strong production cross sections in the two fiducial regions. 75
4.16 Expected and observed numbers of events in the Tri-lepton CR. The uncertainties listed include both statistical and systematic uncertainties combined. 76
4.17 Expected and observed numbers of events in the Low m_{jj} CR. The uncertainties listed include both statistical and systematic uncertainties combined. 77
4.18 Summary of major systematic uncertainties in the Inclusive Signal Region. Relevant sources have been combined and the uncertainties are shown as relative uncertainties on the total number of background and signal events. The dominant source of uncertainty is the jet reconstruction uncertainties, including jet energy scale, jet energy resolution and pile-up jet simulation. 80
4.19 Summary of major systematic uncertainties in the VBS Signal Region. Relevant sources have been combined and the uncertainties are shown as relative uncertainties on the total number of background and signal events. The dominant source of uncertainty is the jet reconstruction uncertainties, including jet energy scale, jet energy resolution and pile-up jet simulation. 81

4.20 Expected and observed numbers of events in the Inclusive Signal Region. In this signal region, the electroweak and strong production of $W^{\pm}W^{\pm}jj$ are both taken as the signal. The uncertainties listed include both the statistical and systematic uncertainties. 81
4.21 Expected and observed numbers of events in the VBS Signal Region. In this signal region, only the electroweak production of $W^{\pm}W^{\pm}jj$ is taken as the signal while the strong production is taken as a background. The uncertainties listed include both the statistical and systematic uncertainties. 82
4.22 The fraction of each di-lepton channel relative to the total production as calculated at truth level using the SHERPA MC simulation. 86
4.23 The detector efficiency for each channel of the signal region. The efficiency is calculated as the fraction of the total expected events in the fiducial signal region which are eventually selected in the signal region at reconstruction level. The uncertainties listed are only statistical uncertainties. 87
4.24 Summary of cross section measurement results. The signal significance is reported in units of standard deviation. The uncertainties on the measured cross section include both statistical and systematic uncertainties. The 95% CL upper limits are also reported given that the $W^{\pm}W^{\pm}jj$ production has not been observed at the LHC. 88
4.25 The aQGC points with fully simulated MC samples. The cross section is given in the total produced sample phase space. The acceptance into the VBS Fiducial SR and the detector efficiency for each di-lepton channel are also presented. The uncertainties listed only include the statistical uncertainties. 89

A.1 Di-boson Monte Carlo samples used in this thesis. 94
A.2 Top Monte Carlo samples used in this thesis. 94
A.3 Z+jets Monte Carlo samples used in this thesis. 95
A.4 W+jets Monte Carlo samples used in this thesis. 96
A.5 $W\gamma$ Monte Carlo samples used in this thesis. 96

B.1 The observed and expected numbers of events in the prompt process control region in di-jet sample. A 4% and 12% uncertainty on the overall W+jets and Z+jets MC prediction will be applied for the electron and muon channel respectively. 102

LIST OF APPENDICES

A Monte Carlo Samples **94**

B Non-prompt Background Estimation **97**

LIST OF ABBREVIATIONS

EWSB electroweak symmetry breaking

SM Standard Model

VBS Vector Boson Scattering

LO leading order

TGC triple gauge couplings

aTGC anomalous triple gauge couplings

QGC quartic gauge couplings

aQGC anomalous quartic gauge couplings

2HDM two-Higgs doublet model

ID Inner Detector

SCT Semi-Conductor Tracker

TRT Transition Radiation Tracker

EM electromagnetic

LAr liquid Argon

MDT Monitored Drift Tube

CSC Cathode Strip Chamber

RPC Resistive Plate Chamber

tgc Thin Gap Chamber

RoI Regions-of-Interest

GRL Good Runs List

MC Monte Carlo

PDF parton distribution function

JVF Jet Vertex Fraction

CL confidence level

mis-ID mis-identification

ABSTRACT

Evidence for Electroweak Production of $W^{\pm}W^{\pm}jj$ in Proton-Proton Collisions at $\sqrt{s} = 8$ TeV with the ATLAS Detector at the LHC

by

Lulu Liu

Chair: Junjie Zhu

This thesis presents the first study of the same-electric-charge $W^{\pm}W^{\pm}jj$ production using 20.3 fb^{-1} of proton-proton collision data at $\sqrt{s} = 8$ TeV recorded by the ATLAS detector at the LHC during the year of 2012. Only the leptonic decays of both W's are considered. Events are selected with two same-electric-charge leptons ($e^{\pm}e^{\pm}$, $e^{\pm}\mu^{\pm}$, $\mu^{\pm}\mu^{\pm}$) and at least two jets. The inclusive and electroweak productions of $W^{\pm}W^{\pm}jj$ are studied in two fiducial signal regions and the production cross sections are measured. First evidence for inclusive and electroweak production is observed with a significance of 4.5 and 3.6 standard deviations respectively. The measured cross sections are in agreement with the Standard Model prediction. First set of constraints on the anomalous $WWWW$ quartic gauge couplings are derived.

Introduction

The Standard Model (SM) of particle physics has been very successful in describing all known elementary particles and their interactions. Only one piece remained missing in the SM until the Higgs discovery in July 2012 [1, 2]. The Higgs boson is the centerpiece in the SM for electroweak symmetry breaking (EWSB), the mechanism for generating mass for the particles. The newly discovered Higgs particle has been found to be consistent with the SM one [3, 4]. However, it still remains to be confirmed whether the Higgs mechanism is fully responsible for EWSB.

In the SM, Vector Boson Scattering (VBS) processes involve the Higgs boson and the absence of the Higgs would lead to unitarity violation at high di-boson invariant mass [5–7]. If the Higgs mechanism is not fully responsible for EWSB, other mechanisms have to exist to avoid the unitarity violation and deviations of VBS processes from the SM predictions will be observed. It is thus crucial to study VBS processes at the LHC to ascertain the nature of EWSB. VBS processes also involve quartic gauge couplings (QGC) vertices. No direct evidence has been observed for processes involving QGC in previous attempts made in other experiments [8–12]. Among all VBS processes at the LHC, same-electric-charge $W^{\pm}W^{\pm}jj$ has the best signal-to-background ratio and is one of the most promising candidates for the first study of VBS at the LHC.

This thesis presents the first study of the inclusive and electroweak productions of $W^{\pm}W^{\pm}jj$ process with the ATLAS detector at 8 TeV. First evidence has been observed for both the inclusive and electroweak productions, where the latter indicates evidence for $W^{\pm}W^{\pm}$ VBS process. Constraints on anomalous quartic gauge couplings (aQGC) are set for the first time on $WWWW$ vertex.

This thesis is organized as follows. Chapter 1 discusses the theory. Chapter 2 gives an overview of the LHC and the ATLAS detector. Chapter 3 presents the object reconstruction and selections. Chapter 4 presents the details about the $W^{\pm}W^{\pm}jj$ measurement. Chapter 5 gives the conclusion and outlook.

CHAPTER 1

Theory

1.1 The Standard Model

The SM describes three fundamental interactions among the elementary particles: the strong interaction, the weak interaction and the electromagnetic interaction, based on the gauge symmetry $SU(3)_C \times SU(2)_L \times U(1)_Y$, where $SU(3)_C$ is the symmetry group of the strong interaction and $SU(2)_L \times U(1)_Y$ is the symmetry group of the unified electroweak interaction. The charge associated with each of the three symmetries is called color for $SU(3)_C$, weak isospin for $SU(2)_L$ and weak hypercharge for $U(1)_Y$. The electromagnetic $U(1)_{em}$ symmetry appears as a subgroup of $SU(2)_L \times U(1)_Y$ after the electroweak symmetry breaking.

The elementary particles in the SM, apart from the Higgs boson, can be put into two categories: the matter particles and the force carriers. All matter particles are fermions with spin 1/2, which are summarized in Table 1.1. All force carriers are vector bosons with spin 1, which appear in the SM theory as gauge fields and thus called gauge bosons, summarized in Table 1.2. The Higgs boson is a scalar with spin 0 and mass measured to be around 125 GeV [1, 2]. In Table 1.1 the neutrinos are listed as weak (or flavor) eigenstates, which are mixtures of mass eigenstates and the mass is defined as the average $m_{\nu_\ell}^{\text{eff}} = \sqrt{\sum_i |U_{\ell i}|^2 m_{\nu i}^2}$, where $\ell = e, \mu, \tau$ and i denotes the three mass eigenstates. The matrix $U_{\ell i}$ specifies the mixings. By historical convention, the quarks are instead listed as mass eigenstates which are mixtures of weak eigenstates, and the mass is given as calculated using $\overline{\text{MS}}$ renormalization scheme except the top mass as the measured pole mass.

The SM is a chiral theory, in the sense that the chiral left-handed and right-handed fermions behave differently in weak interactions, described by the $SU(2)_L$ doublets and singlets respectively. The physical fermions are mixtures of both chiralities except the neutrinos. The neutrinos are found to be always chiral left-handed.

Generation	Leptons	Charge [e]	Mass [MeV]	Quarks	Charge [e]	Mass [MeV]
1st	e^-	-1	0.511	u	+2/3	$2.3^{+0.7}_{-0.5}$
	ν_e	0	$< 2 \times 10^{-6}$ (95% CL)	d	-1/3	$4.8^{+0.5}_{-0.3}$
2nd	μ^-	-1	105.658	c	+2/3	$(1.275 \pm 0.025) \times 10^3$
	ν_μ	0	< 0.19 (90% CL)	s	-1/3	95 ± 5
3rd	τ^-	-1	1776.82 ± 0.16	t	+2/3	$(173.21 \pm 0.87) \times 10^3$
	ν_τ	0	< 18.2 (95% CL)	b	-1/3	$(4.18 \pm 0.03) \times 10^3$

Table 1.1: Leptons and quarks. [13]

Particle	Interaction	Spin	Charge [e]	Mass [GeV]
g (gluon)	strong	1	0	0
$W^\pm$	weak	1	± 1	80.385 ± 0.015
Z	weak	1	0	91.1876 ± 0.0021
γ (photon)	electromagnetic	1	0	0
H	-	0	0	125.7 ± 0.4

Table 1.2: Gauge bosons and the Higgs boson. [13]

1.2 Gauge Boson and Higgs Interactions

The dynamics of the SM are specified by the Lagrangian density of the theory, which can be put as [14]:

$$\mathcal{L}_{\text{SM}} = \mathcal{L}_{\text{gauge}} + \mathcal{L}_{\text{fermion}} + \mathcal{L}_{\text{Higgs}} + \mathcal{L}_{\text{Yukawa}}, \tag{1.1}$$

where

$$\mathcal{L}_{\text{gauge}} = -\frac{1}{4} G^i_{\mu\nu} G^{i\mu\nu} - \frac{1}{4} W^i_{\mu\nu} W^{i\mu\nu} - \frac{1}{4} B_{\mu\nu} B^{\mu\nu}, \tag{1.2}$$

$$\begin{aligned} \mathcal{L}_{\text{fermion}} = &\sum_\ell i\bar{\ell}_{\text{L}} \gamma^\mu D_\mu \ell_{\text{L}} + \sum_q i\bar{q}_{\text{L}} \gamma^\mu D_\mu q_{\text{L}} + \sum_u i\bar{u}_{\text{R}} \gamma^\mu D_\mu u_{\text{R}} \\ &+ \sum_d i\bar{d}_{\text{R}} \gamma^\mu D_\mu d_{\text{R}} + \sum_e i\bar{e}_{\text{R}} \gamma^\mu D_\mu e_{\text{R}}, \end{aligned} \tag{1.3}$$

$$\mathcal{L}_{\text{Higgs}} = (D_\mu \Phi)^\dagger (D_\mu \Phi) - V(\Phi) = (D_\mu \Phi)^\dagger (D_\mu \Phi) - \mu^2 \Phi^\dagger \Phi - \lambda (\Phi^\dagger \Phi)^2, \tag{1.4}$$

$$\mathcal{L}_{\text{Yukawa}} = -\sum_{q,u} y_{qu} \bar{q}_{\text{L}} \tilde{\Phi} u_{\text{R}} - \sum_{q,d} y_{qd} \bar{q}_{\text{L}} \Phi d_{\text{R}} - \sum_{\ell,e} y_{\ell e} \bar{\ell}_{\text{L}} \Phi e_{\text{R}} + h.c.. \tag{1.5}$$

The gauge fixing and ghost terms have been ignored here.

The lepton and quark fileds are given in weak eigenstates. The $SU(2)_L$ doublet

fields for leptons and quarks are defined as

$$\ell_{\rm L} = \begin{pmatrix} \nu_\ell \\ \ell^- \end{pmatrix}_{\rm L}, \quad q_{\rm L} = \begin{pmatrix} u \\ d \end{pmatrix}_{\rm L}, \tag{1.6}$$

where ℓ can be e, μ or τ and (u, d) can be also (c, s) and (t, b). The $SU(2)_L$ singlet field is denoted as $e_{\rm R}$, $u_{\rm R}$ and $d_{\rm R}$, where e, u and d actually runs over all charged leptons and u- and d-type quarks. The chiral left- and right-handed field for a fermion ψ is defined as

$$\psi_{\rm L} = P_{\rm L}\psi = \frac{1-\gamma^5}{2}\psi, \quad \psi_{\rm R} = P_{\rm R}\psi = \frac{1+\gamma^5}{2}\psi. \tag{1.7}$$

The chiral right-handed neutrino field has been ignored here, which can be introduced similarly in the kinematic and mass terms.

The gauge field strength tensors are given as

$$G^i_{\mu\nu} = \partial_\mu G^i_\nu - \partial_\nu G^i_\mu - g_s f_{ijk} G^j_\mu G^k_\nu, \;\; i,j,k = 1, \cdots, 8 \tag{1.8}$$

$$W^i_{\mu\nu} = \partial_\mu W^i_\nu - \partial_\nu W^i_\mu - g_1 \epsilon_{ijk} W^j_\mu W^k_\nu, \;\; i,j,k = 1, \cdots, 3 \tag{1.9}$$

$$B_{\mu\nu} = \partial_\mu B_\nu - \partial_\nu B_\mu, \tag{1.10}$$

where G^i_μ ($i = 1, \cdots, 8$), W^i_μ ($i = 1, 2, 3$) and B_μ are the gauge fields for $SU(3)_C$, $SU(2)_L$ and $U(1)_Y$ respectively. The covariant derivative is

$$D_\mu = \partial_\mu + \frac{ig_1}{2}\vec{\tau}\cdot\vec{W}_\mu + \frac{ig_2}{2}YB_\mu + \frac{ig_s}{2}\vec{\lambda}\cdot\vec{G}_\mu, \tag{1.11}$$

where $\vec{\lambda}$, $\vec{\tau}$ and Y are the generators for the corresponding gauge symmetry groups and $g_{1,2,s}$ is the coupling strength factor.

In the Lagrangian 1.1, there are no bare mass terms for fermions or gauge bosons due to the requirement of gauge invariance. The Higgs field Φ is introduced to break the $SU(2)_L \times U(1)_Y$ symmetry and generate the mass terms in a gauge invariant way [15–17]. The Higgs field Φ is a complex scalar which can be put as

$$\Phi = \begin{pmatrix} \phi^+ \\ \phi^0 \end{pmatrix} = \begin{pmatrix} \frac{1}{\sqrt{2}}(\phi_1 + i\phi_2) \\ \frac{1}{\sqrt{2}}(\phi_3 + i\phi_4) \end{pmatrix}. \tag{1.12}$$

where $\phi_i = \phi_i^\dagger$ are Hermitian fields. The Higgs potential in Eqn. 1.4 now becomes

$$V(\Phi) = \frac{1}{2}\mu^2 \left(\sum_{i=1}^{4} \phi_i^2 \right) + \frac{1}{4}\lambda \left(\sum_{i=1}^{4} \phi_i^2 \right)^2 . \tag{1.13}$$

$V(\Phi)$ has an $O(4)$ symmetry and one can always choose the axis such that $\langle 0| \phi_i |0\rangle = 0$ for $i = 1, 2, 4$ and $\langle 0| \phi_3 |0\rangle = v \geq 0$ (unitary gauge). Then the vacuum expectation value of the field and the potential can be written as

$$\Phi_0 = \frac{1}{\sqrt{2}} \begin{pmatrix} 0 \\ v \end{pmatrix}, \tag{1.14}$$

$$V(v) = \frac{1}{2}\mu^2 v^2 + \frac{1}{4}\lambda v^4. \tag{1.15}$$

For $V(v)$ to be bounded from below, one needs $\lambda > 0$. For $\mu^2 > 0$, the minimum of $V(v)$ happens at $v = 0$ with $SU(2)_L \times U(1)_Y$ unbroken. For $\mu^2 < 0$, $V(v)$ has the minimum at

$$v = \sqrt{\frac{-\mu^2}{\lambda}}. \tag{1.16}$$

The Higgs potential is shown in Figure 1.1 qualitatively for $\mu^2 > 0$ and $\mu^2 < 0$. The Higgs field Φ can be expanded around the minimum with

$$\Phi = \frac{1}{\sqrt{2}} \begin{pmatrix} 0 \\ v + H \end{pmatrix} \tag{1.17}$$

where H is a Hermitian scalar field which represents the physical Higgs boson. The other three degrees of freedom, which have been chosen to be zero in the unitary gauge, correspond to the massless Goldstone bosons.

The Higgs kinematic term can now be expanded as

$$\begin{aligned} (D_\mu \Phi)^\dagger D^\mu \Phi =& \frac{1}{2}(\partial_\mu H)^2 + \frac{g_1^2}{8}(W^{1\mu} + iW^{2\mu})(W_\mu^1 - iW_\mu^2)(v+H)^2 \\ &+ \frac{1}{8}(g_1 W^{3\mu} - g_2 B^\mu)(g_1 W_\mu^3 - g_2 B_\mu)(v+H)^2 \\ =& \frac{1}{2}(\partial_\mu H)^2 + \frac{g_1^2}{4} W^{+\mu} W_\mu^- (v+H)^2 + \frac{1}{2}\frac{g_1^2 + g_2^2}{4} Z^\mu Z_\mu (v+H)^2, \end{aligned} \tag{1.18}$$

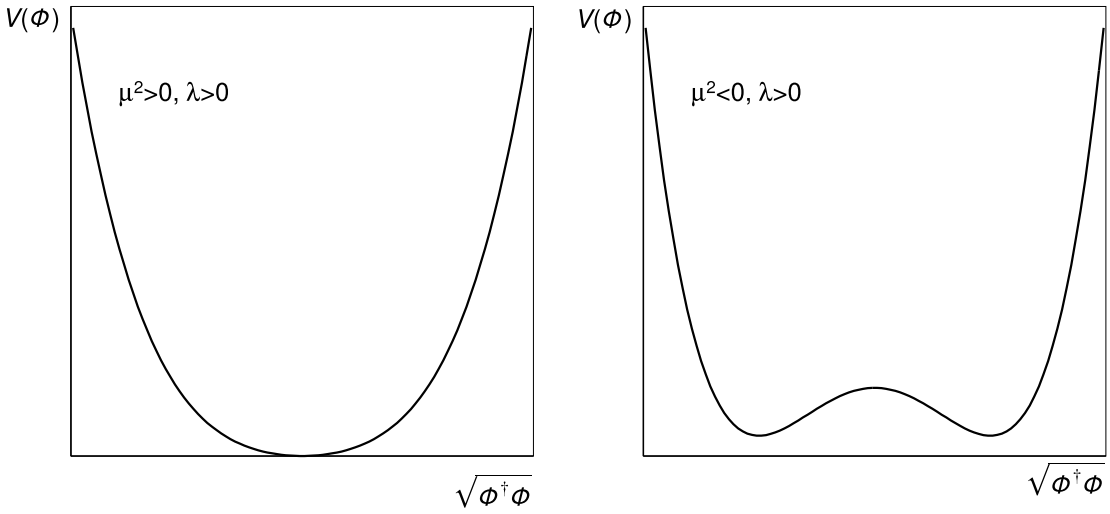

Figure 1.1: The Higgs potential as a function of $\sqrt{\Phi^\dagger\Phi}$ for the case of $\mu^2 > 0$ and $\mu^2 < 0$.

where we have defined the new fields

$$W^\pm = \frac{W^1 \mp iW^2}{\sqrt{2}}, \tag{1.19}$$

$$Z = \frac{g_1 W^3 - g_2 B}{\sqrt{g_1^2 + g_2^2}} \tag{1.20}$$

which are the physical $W^\pm$ and Z bosons. The photon field is identified as

$$A = \frac{g_1 B + g_2 W^3}{\sqrt{g_1^2 + g_2^2}}. \tag{1.21}$$

The weak mixing angle θ_W is defined by

$$\sin\theta_W = \frac{g_2}{\sqrt{g_1^2 + g_2^2}}, \cos\theta_W = \frac{g_1}{\sqrt{g_1^2 + g_2^2}} \tag{1.22}$$

The terms in Eqn. 1.18 not involving H give the masses for $W^\pm$ and Z, while the other terms specify the couplings between the Higgs boson and the gauge bosons.

If we define the $W^{\pm}$ and Z mass as

$$m_W = \frac{g_1 v}{2}, \tag{1.23}$$

$$m_Z = \frac{v\sqrt{g_1^2 + g_2^2}}{2} \tag{1.24}$$

Eqn. 1.18 becomes

$$\begin{aligned}(D_\mu \Phi)^\dagger D^\mu \Phi =& \frac{1}{2}(\partial_\mu H)^2 + m_W^2 W^{+\mu} W_\mu^- + \frac{2m_W^2}{v} W^{+\mu} W_\mu^- H + \frac{m_W^2}{v^2} W^{+\mu} W_\mu^- H^2 \\ &+ \frac{1}{2} m_Z^2 Z^\mu Z_\mu + \frac{m_Z^2}{v} Z^\mu Z_\mu H + \frac{m_Z^2}{2v} Z^\mu Z_\mu H^2.\end{aligned} \tag{1.25}$$

The Lagrangian term 1.2 can now be spelled out using the newly defined $W^{\pm}$, giving a 3-point triple gauge couplings (TGC) term

$$\begin{aligned}\mathcal{L}_{W^3} =& - ig_1(\partial_\rho W_\nu^3) W_\mu^+ W_\sigma^- [g^{\rho\mu} g^{\nu\sigma} - g^{\rho\sigma} g^{\nu\mu}] \\ &- ig_1(\partial_\rho W_\mu^+) W_\nu^3 W_\sigma^- [g^{\rho\sigma} g^{\mu\nu} - g^{\rho\nu} g^{\mu\sigma}] \\ &- ig_1(\partial_\rho W_\sigma^-) W_\nu^3 W_\mu^+ [g^{\rho\nu} g^{\mu\sigma} - g^{\rho\mu} g^{\nu\sigma}]\end{aligned} \tag{1.26}$$

and a 4-point QGC term

$$\mathcal{L}_{W^4} = \frac{g_1^2}{4} \left[W_\mu^+ W_\nu^+ W_\sigma^- W_\rho^- \mathcal{Q}^{\mu\nu\rho\sigma} - 2 W_\mu^+ W_\nu^3 W_\sigma^3 W_\rho^- \mathcal{Q}^{\mu\rho\nu\sigma} \right], \tag{1.27}$$

where

$$\mathcal{Q}_{\mu\nu\rho\sigma} = 2 g_{\mu\nu} g_{\rho\sigma} - g_{\mu\rho} g_{\nu\sigma} - g_{\mu\sigma} g_{\nu\rho}. \tag{1.28}$$

These two terms generate the gauge boson self-interactions after replacing W^3 with $\frac{g_1 Z + g_2 A}{\sqrt{g_1^2 + g_2^2}}$. The TGC and QGC involving only the neutral Z and γ bosons are absent at LO in the SM given the $SU(2)_L \times U(1)_Y$ symmetry group structure.

The feynman rules are summarized in Table 1.3 [14] for the gauge boson and Higgs interactions which are most relevant for VBS processes.

In this section, we have presented the gauge and Higgs sectors of the SM Lagrangian, which generate the W/Z mass, the gauge boson - Higgs couplings and the gauge boson self-interactions. The fermion mass and the fermion couplings to the gauge boson and Higgs boson can be derived from Eqn. 1.3 and 1.5 [14] and will be skipped here.

Vertex	Diagram	Feynman rule
$W^+_\mu W^-_\nu H$	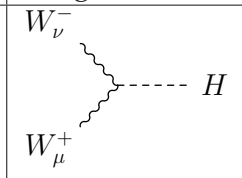	$2ig_{\mu\nu}\dfrac{m_W^2}{v}$
$Z_\mu Z_\nu H$	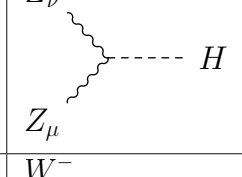	$2ig_{\mu\nu}\dfrac{m_Z^2}{v}$
$W^+_\mu(p)\gamma_\nu(q)W^-_\sigma(r)$	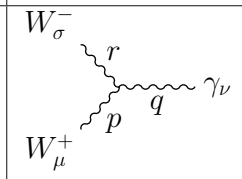	$ie\mathcal{C}_{\mu\nu\sigma}(p,q,r)$
$W^+_\mu(p)Z_\nu(q)W^-_\sigma(r)$	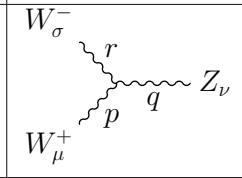	$ig_1\cos\theta_W\mathcal{C}_{\mu\nu\sigma}(p,q,r)$
$W^+_\mu W^+_\nu W^-_\rho W^-_\sigma$	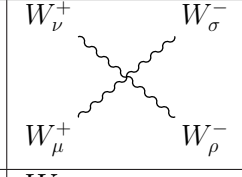	$ig_1^2\mathcal{Q}_{\mu\nu\rho\sigma}$
$W^+_\mu Z_\nu \gamma_\sigma W^-_\rho$	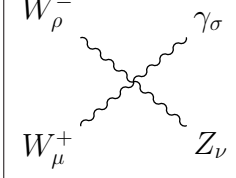	$-ieg_1\cos\theta_W\mathcal{Q}_{\mu\rho\nu\sigma}$
$W^+_\mu Z_\nu Z_\sigma W^-_\rho$	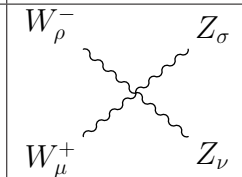	$-ig_1^2\cos^2\theta_W\mathcal{Q}_{\mu\rho\nu\sigma}$
$W^+_\mu \gamma_\nu \gamma_\sigma W^-_\rho$	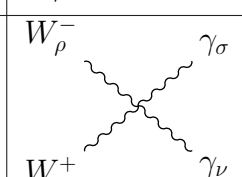	$-ie^2\mathcal{Q}_{\mu\rho\nu\sigma}$

Table 1.3: Feynman rules for the gauge and Higgs interactions. The momenta and charge flow into the vertex. We have defined $\mathcal{C}_{\mu\nu\rho}(p,q,r) \equiv g_{\mu\nu}(q-p)_\sigma + g_{\mu\sigma}(p-r)_\nu + g_{\nu\sigma}(r-q)_\mu$ and $\mathcal{Q}_{\mu\nu\rho\sigma} = 2g_{\mu\nu}g_{\rho\sigma} - g_{\mu\rho}g_{\nu\sigma} - g_{\mu\sigma}g_{\nu\rho}$.

1.3 Vector Boson Scattering

In general, VBS processes involve the following diagrams at leading order (LO) as shown in Figure 1.2, 1.3 and 1.4. In choosing the vacuum expectation value as in Eqn. 1.14 for the Higgs field, the other three degrees of freedom, or Goldstone bosons, have disappeared and are absorbed by the $W^{\pm}$ and Z bosons to form the longitudinal components [1]. At high energies, the longitudinal components of the vector bosons act just like the Goldstone bosons and are intimately related to the Higgs. Thus the lontigudinal component of VBS $V_L V_L \rightarrow V_L V_L$ is of particular interest and has been extensively studied theoretically [5–7].

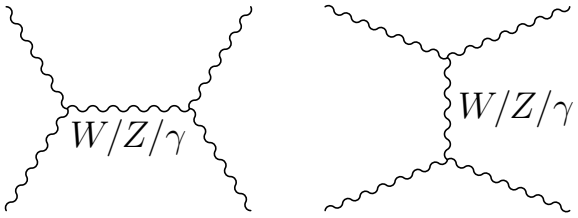

Figure 1.2: The s-channel (left) and t-channel (right) VBS processes involving TGC.

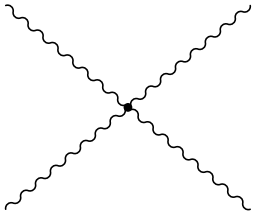

Figure 1.3: VBS processes involving QGC.

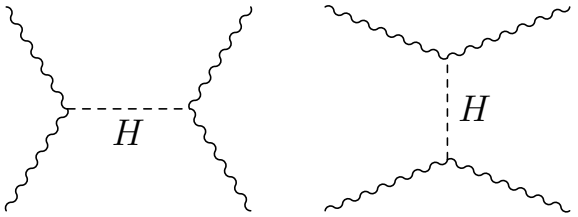

Figure 1.4: VBS processes involving Higgs boson.

[1] The massless gauge bosons, photon and gluon, do not have the longitudinal components of polarization.

As an example, the leadng term in the $W_L^+W_L^-$ scattering amplitude [18, 19] is [2]

$$i\mathcal{M}_{\text{TGC}}^{\text{s-channel}} = -i\frac{g_1^2}{4m_W^4}\left[s(t-u) - 3m_W^2(t-u)\right], \tag{1.29}$$

$$i\mathcal{M}_{\text{TGC}}^{\text{t-channel}} = -i\frac{g_1^2}{4m_W^4}\left[t(s-u) - 3m_W^2(s-u) + \frac{8m_W^2}{s}u^2\right], \tag{1.30}$$

$$i\mathcal{M}_{\text{QGC}} = i\frac{g_1^2}{4m_W^4}\left[s^2 + 4st + t^2 - 4m_W^2(s+t) - \frac{8m_W^2}{s}ut\right], \tag{1.31}$$

$$i\mathcal{M}_{\text{Higgs}} = -i\frac{C_v^2 g_1^2}{4m_W^2}\left[\frac{(s-2m_W^2)^2}{s-m_H^2} + \frac{(t-2m_W^2)^2}{t-m_H^2}\right]. \tag{1.32}$$

Here we have listed the amplitudes separatly for the s-channel and t-channel TGC diagrams in Figure 1.2, the QGC diagram in Figure 1.3 and the Higgs diagrams in Figure 1.4. A coupling scale factor C_v^2 is inserted for the Higgs term which should be exactly 1 in the SM. The TGC terms Eqn. 1.29 and 1.30 combine to give

$$i\mathcal{M}_{\text{TGC}} = -i\frac{g_1^2}{4m_W^4}\left[s^2 + 4st + t^2 + 3m_W^2 t - 5m_W^2 s + 8m_W^2\frac{t^2}{s}\right] \tag{1.33}$$

which cancels the QGC term to give

$$i\mathcal{M}_{\text{TGC}} + i\mathcal{M}_{\text{QGC}} = i\frac{g_1^2}{4m_W^2}(s+t) + \mathcal{O}((s/m_W^2)^0). \tag{1.34}$$

In the high energy limit,

$$i\mathcal{M}_{\text{Higgs}} = -i\frac{C_v^2 g_1^2}{4m_W^2}(s+t), \tag{1.35}$$

which nicely cancels the term 1.34 to give $\mathcal{O}((s/m_W^2)^0)$ dependence for the total amplitude if C_v^2 is exactly equal to 1. In the absence of the Higgs boson, with $C_v^2 = 0$, the scattering amplitude Eqn. 1.34 grows as a function of the center-of-mass energy squared s and violates unitarity in the TeV regime. This is one of the reasons the Higgs boson is needed in the SM. In some new physics scenarios, for example the two-Higgs doublet model (2HDM) [20–22], where C_v^2 is not exactly

[2] Mandelstam variables s, t and u are defined for a two-particle scattering process with incoming 4-momenta p_1, p_2 and outcoming 4-momenta p_3, p_4 as:

$$s = (p_1+p_2)^2 = (p_3+p_4)^2,\ \ t = (p_1-p_3)^2 = (p_2-p_4)^2,\ \ u = (p_1-p_4)^2 = (p_2-p_3)^2.$$

1, the $\mathcal{O}(s)$ energy dependence should be observed at high energies [18, 19] until new physics comes in to complete the cancellation.

1.4 Anomalous Quartic Gauge Coupling

New physics may exist at an energy scale well beyond the reach of LHC. The low energy effects of new physics at high energy scale can be parameterized using effective field theory by adding higher dimensional operators to the SM Lagrangian

$$\mathcal{L}_{\text{eff}} = \mathcal{L}_{\text{SM}} + \sum_{d\geq 4}\sum_{i}\frac{\alpha_i^{(d)}}{\Lambda^{d-4}}O_i^{(d)}. \tag{1.36}$$

The chiral Lagrangian approach [23, 24] is taken in this thesis. The new operators added can affect the TGC and QGC vertices depending on the fields involved. The anomalous triple gauge couplings (aTGC) have been constrained tightly in other studies and are not considered here. The lowest-order operators which contribute to the QGC vertices are dimensional-4 operators

$$\alpha_4 O_4^{(4)} = \alpha_4\left[\text{Tr}(V_\mu V_\nu)\right]^2, \alpha_5 O_5^{(4)} = \alpha_5\left[\text{Tr}(V_\mu V^\mu)\right]^2, \tag{1.37}$$

where V_μ is defined as

$$V_\mu = \Sigma(D_\mu\Sigma)^\dagger \tag{1.38}$$

and the field Σ is built out of the Goldstone scalar triplet with

$$\Sigma = \exp\left(-\frac{i}{v}\vec{w}\right) \tag{1.39}$$

V_μ can reduce to $-ig_1\vec{W}_\mu + ig_2 B_\mu$ in the unitary gauge where $\Sigma = 1$.

Adding operators to the SM Lagrangian usually violates unitarity. The K-matrix method [25–27] is used in this thesis to restore unitarity for the aQGC implementation. For partial wave amplitude a_l, the optical theorem requires for the Argand-circle unitarity condition

$$|a_l - i/2| = 1/2, \tag{1.40}$$

which can be also put as

$$\mathrm{Im}\frac{1}{a_l} = -1. \tag{1.41}$$

In K-matrix model, for an arbitrary amplitude $a(s)$, it can be transformed into a unitary amplitude by taking the real part of $1/a(s)$ and adding $-i$ as the imaginary part

$$a(s) \to a_K(s) = \frac{1}{\mathrm{Re}(1/a(s)) - i}. \tag{1.42}$$

which is equivalent to projecting the amplitude onto the Argand circle, as illustrated in Figure 1.5, where the amplitude is already taken as real.

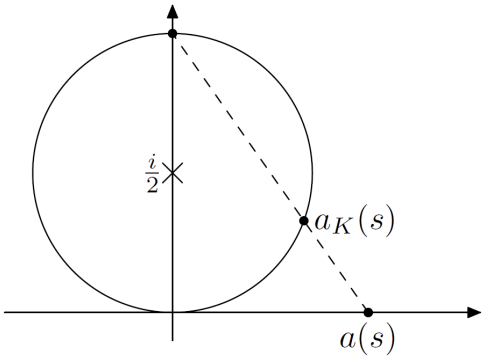

Figure 1.5: The projection of a real amplitude $a(s)$ onto the Argand circle.

CHAPTER 2

The LHC and ATLAS

2.1 The Large Hadron Collider

The Large Hadron Collider (LHC) [28] is a particle accelerator and collider operated by CERN, located on the border between France and Switzerland. It makes use of a multi-stage complex to accelerate charged particle beams to multi-TeV energy. The LHC complex is shown in Figure 2.1, which consists of the Linac, Proton Synchrotron Booster (PSB), Proton Synchrotron (PS), Super Proton Synchrotron (SPS) and the LHC main ring with a circumference of 27 km. The energy at each stage of the acceleration chain is listed and proton beams are accelerated to energy 450 GeV before they are injected into the main ring, where the final stage of the acceleration is done.

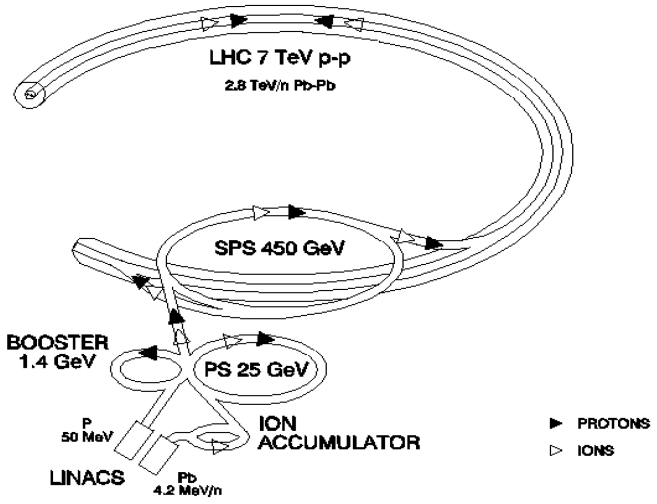

Figure 2.1: The LHC accelerator complex.

There are four collision points on the main ring, each hosting one of the four

main experiments: ATLAS, CMS, LHCb and ALICE [29–32], as shown in Figure 2.2.

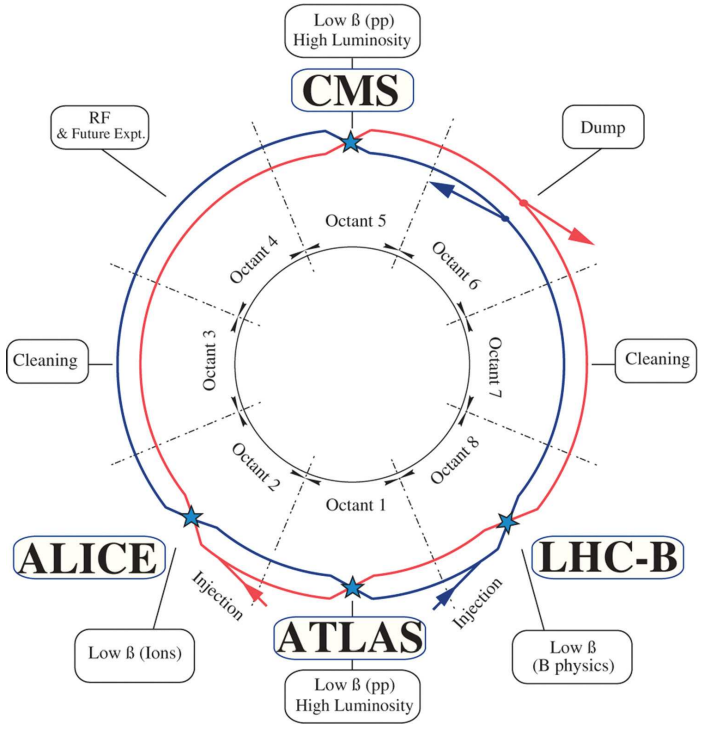

Figure 2.2: The four collision points at LHC.

The LHC has a design center-of-mass energy of 14 TeV for proton-proton collisions. So far it has only operated at reduced energies of 900 GeV (2009), 7 TeV (2010 and 2011) and 8 TeV (2012). The proton beam is not continuous but organized in bunches. For the run in 2012, proton bunches were seperated with 50 ns. Peak instantaneous luminosity of 7.7×10^{33} cm^{-2}s^{-1} was reached. The data sample analyzed in this thesis was collected during the 2012 operation, with an integrated luminosity of 20.3 fb^{-1}.

2.2 The ATLAS Detector

ATLAS (A Toroidal LHC ApparatuS) [29] is one of the two general-purpose detectors at the LHC. (The other one is CMS [30].) To fully exploit the discovery potentials provided by the LHC collisions, the ATLAS detector has been designed with the full capacity for detecting final state particles with high performance. The

ATLAS detector consists of the magnet system, inner tracking detector, calorimeters, muon spectrometer and the trigger system. A cut-away view of the detector is shown in Figure 2.3. The detector is a 44 m long cylinder with a 25 m diameter which weighs around 7000 tonnes. A brief summary of the detector system is given in this section. More details can be found in Ref. [29].

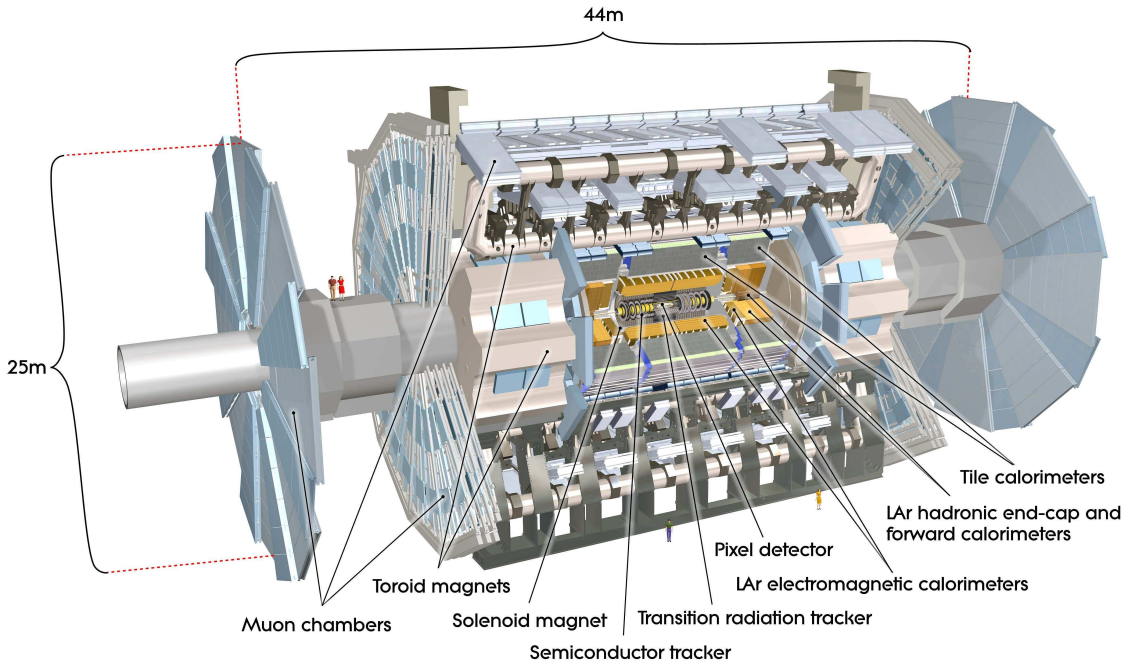

Figure 2.3: The ATLAS detector.

2.2.1 The Coordinate System

The ATLAS detector uses a right-handed coordinate system, with the nominal interaction point as the origin, the x-axis pointing to the center of the LHC ring, the y-axis pointing up and the z-axis along the tunnel. The x-y plane defines the transverse plane. The A-side of the detector is defined as that with positive z and the C-side with negative z. The polar angle θ is measured from the positive z-axis and the azimuthal angle ϕ is measured in the transverse plane relative to the positive y-axis. The rapidity of particles is defined as $y = 1/2 \ln [(E + p_z)/(E - p_z)]$. In the massless limit, where the particle mass is small compared to the momentum, the rapidity can be approximated using pseudorapidity $\eta = -\ln \tan(\theta/2)$. This applies to all leptons we discuss in this thesis. The transverse momentum p_{T}, transverse

energy E_{T} and transverse missing energy $E_{\mathrm{T}}^{\mathrm{miss}}$ are all defined in the transverse plane. The distance ΔR is defined using the pseudorapidity and the azimuthal angle as $\Delta R = \sqrt{(\Delta\eta)^2 + (\Delta\phi)^2}$. It is worth noting that differences in rapidity (Δy) and pseudorapidity ($\Delta\eta$), distance ΔR, transverse momentum (p_{T}) and transverse energy (E_{T}) are Lorentz invariant with respect to boosts along the z axis. Since we do not know for each data event what the z-momenta of the colliding partons are, it is important to work with variables which are not sensitive to boosts along the z-axis.

2.2.2 Magnet System

The ATLAS magnet system consists of the solenoid magnet, which provides magnetic field for the inner detector, and the toroid magnets, which provide magnetic field for the muon spectrometer. The solenoid magnet is 5.8 m long and has an inner diameter of 2.46 m and an outer diameter of 2.56 m. The superconducting windings provide the inner detector with a peak axial magnetic field of 2 T when it's operated at the nominal 7.730 kA current. There are three toroid magnets, two in the endcap and one in the barrel, each consisting of eight coils working at a nominal current of 20.5 kA. The barrel toroid is 25.3 m long with inner and outer diameters of 9.4 m and 20.1 m. The endcap toroid is 5.0 m in length, 1.65 m in inner diameter and 10.7 m in outer diameter. The magnetic field in the toroids is not uniform and peaks at 3.9 T and 4.1 T in the barrel and endcap respectively. The total field integral ($\int \vec{B} d\vec{L}$), which characterizes the total bending power of the magetic field, is shown in Figure 2.4.

2.2.3 Inner Detector

The Inner Detector (ID) is designed to measure the tracks of charged particles within $|\eta| < 2.5$, which can be used for charged particle momentum measurement, particle pattern recognition and primary and secondary vertex reconstruction. The ID is contained in a cylinder of length $\pm$ 3512 mm and of radius 1150 mm, immersed in a 2 T axial magnetic field. From the inner layer to the outer layer, it consists of the Pixel detector, the Semi-Conductor Tracker (SCT) and the Transition Radiation Tracker (TRT). A detailed layout is shown in Figure 2.5 for one quarter of the inner detector.

Closest to the beam, the Pixel detector has the finest granularity. Using the

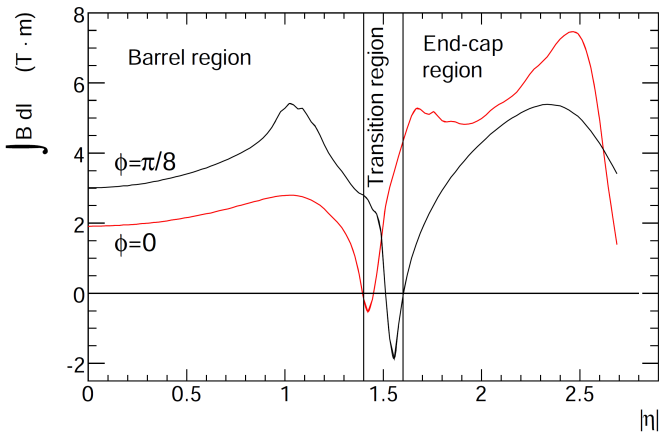

Figure 2.4: Magnetic field integral along trajectories in the ATLAS detector with $\phi = 0$ (red) and $\phi = \pi/8$ (black) as a function of η for infinite-momentum muons.

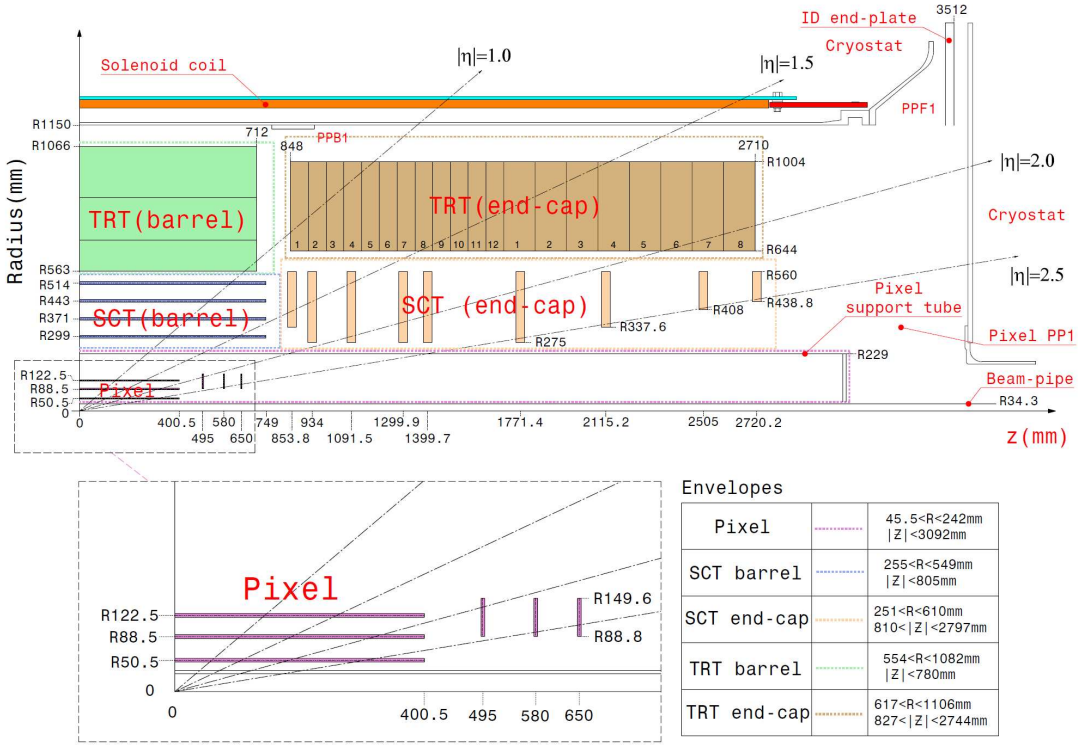

Figure 2.5: Layout of the ATLAS inner detector.

pixel technology, it can achieve a spatial resolution of 10 μm $\times$ 115 μm, which is important for the interaction vertex reconstruction. There are three barrel layers

and three endcap disks on each side. The pixel strip is in parallel with the beam in the barrel and perpendicular in the endcap. With a total of 1744 sensors and 47232 pixels on each sensor, the total number of readout channels is over 82 million.

The SCT is made of four barrel layers and nine endcap disks on each side. It uses the silicon micro-strip technology which can provide measurements with a resolution of 17 μm in the ϕ direction and 580 μm in z (in the barrel) or R (in the endcap) direction. The total area of detectors is 61 m^2 with 6.2 million readout channels.

The TRT is based on straw tubes, which are aligned in parallel with the beam in the barrel region and radially in the endcap region. The straw tube is made of a cathode tube with an anode wire in the center, filled with a mixture of 70% Xe, 27% CO_2 and 3% O_2 gas. The tube measures the drift time of ionization charges caused by charged particles passing by and provides a spatial resolution of ~ 130 μm. The gap between tubes are filled with transition radiator material. The Xe gas can absorb transition radiation and cause a much higher signal than the minimum-ionising charged particles. This feature is used for separating electrons with other charged particles given the electron mass is much smaller than other particles and electrons produce more transition radiation. The total number of readout channels is around 351,000 for the TRT.

A typical track on average causes 3 hits in the Pixel, 8 hits in the SCT and 36 hits in the TRT.

2.2.4 Calorimeters

The ATLAS calorimeter system consists of the electromagnetic (EM) calorimeter and the hadronic calorimeter. It covers the range of $|\eta| < 4.9$ and provides identification and energy measurement for electrons, photons, τ's, hadronic jets and $E_{\mathrm{T}}^{\mathrm{miss}}$. A cut-away view of the calorimeter system is given in Figure 2.6. Both the EM calorimeter and the hadronic calorimeter are designed based on the sampling methodology, which consists of an absorber and an active material. The absorber is usually of high density and serves for electromagnetic and hadronic shower development and the active material collects and measures the energy deposited, which is only a fraction of the total energy of the mother particle. With proper calibration, the energy of the mother particle can be measured using extrapolation.

The EM calorimeter uses liquid Argon (LAr) as the active material and lead plates as the absorber. It is further divided into the barrel ($|\eta| < 1.475$) and the

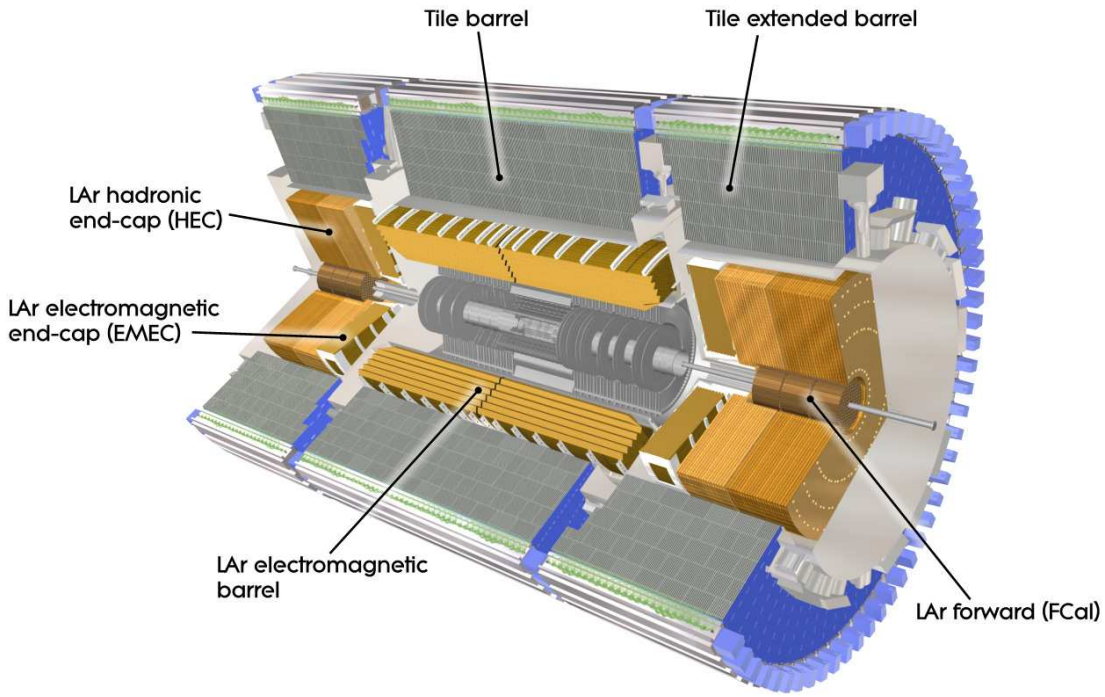

Figure 2.6: The ATLAS calorimeter system.

endcaps ($1.375 < |\eta| < 3.2$). In the region $|\eta| < 1.8$ there is a presampler layer of only LAr to measure the energy lost by electrons and photons to the material before the calorimeter. The EM calorimeter has a finer granularity over $|\eta| < 2.5$ corresponding to the inner detector coverage to better measure the electrons and photons. The coarser granularity in the rest of the calorimeter suffices for the jet reconstruction and $E_{\mathrm{T}}^{\mathrm{miss}}$ measurement. The hadronic calorimeter consists of the tile calorimeter in the barrel ($|\eta| < 1.0$) and extended barrel ($0.8 < |\eta| < 1.7$), LAr hadronic endcap ($1.5 < |\eta| < 3.2$) and the LAr forward calorimeter ($3.1 < |\eta| < 4.9$). The tile calorimeter uses steel as the absorber and scintillating tiles as the active material. The LAr hadronic endcap calorimeter uses copper as the absorber and the LAr forward calorimeter uses copper and tungsten, both with LAr as the active material.

The calorimeter is expected to completely contain the EM and hadronic showers to avoid any punch-through into the muon system which lies just outside. The total amount of material in the ATLAS detector before and in the EM calorimeter is shown in Figure 2.7 in units of EM radiation length (the average length of material

for a high-energy electron to lose all but $1/e$ of its energy). The total amount of material before the muon system is shown in Figure 2.8 in units of nuclear interaction length (the average length of material to reduce the number of particles by $1/e$ when they pass through).

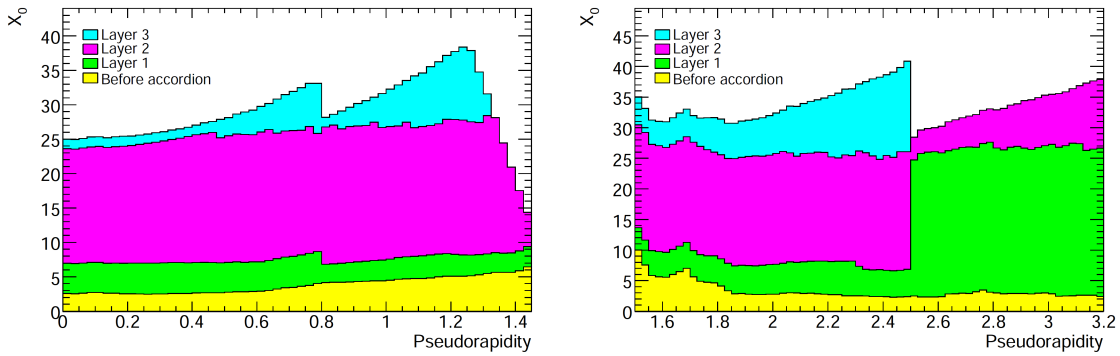

Figure 2.7: Total amount of material before and in the EM calorimeter in units of EM radiation length.

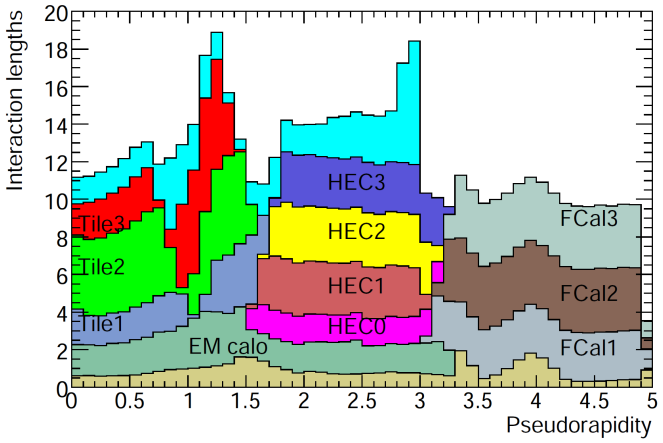

Figure 2.8: Total amount of material before the first active layer of the muon system in units of nuclear interaction length.

The energy resolution of the calorimeters is usually parameterized as

$$\frac{\sigma_E}{E} = \frac{a}{\sqrt{E}} \oplus \frac{b}{E} \oplus c, \tag{2.1}$$

with E in GeV, where a is the stochastic term, b the noise term and c the constant term reflecting local non-uniformities in the calorimeter response. For the

EM calorimeter, the design values are respectively $a \simeq 10\%$, $b \simeq 0.17$ GeV and $c = 0.7\%$ [33]. For the tile calorimeter and LAr hadronic endcap, the resolution is [29]

$$\frac{\sigma_E}{E} = \frac{50\%}{\sqrt{E}} \oplus 3\%, \tag{2.2}$$

and for the LAr forward calorimeter

$$\frac{\sigma_E}{E} = \frac{100\%}{\sqrt{E}} \oplus 10\%. \tag{2.3}$$

2.2.5 Muon Spectrometer

The muon spectrometer is stationed outside the calorimeters and forms the outermost part of the whole ATLAS detector. The layout of the muon system is shown in Figure 2.9.

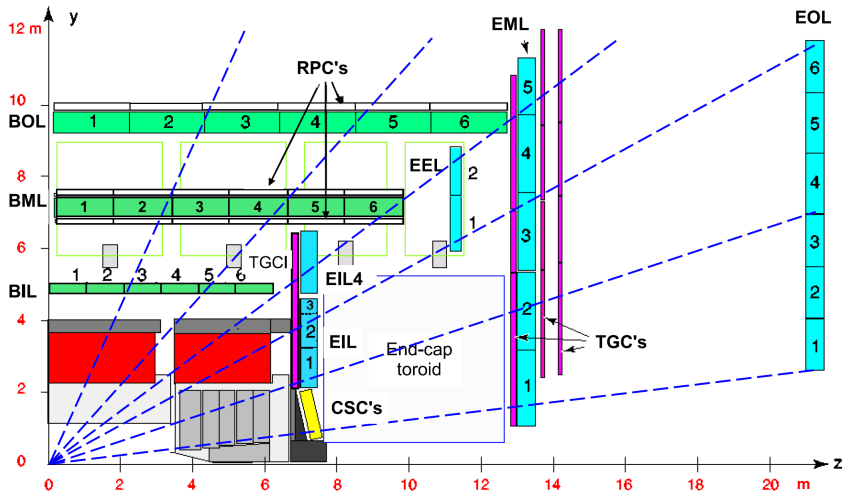

Figure 2.9: Layout of a quarter of the muon system. The MDT's are shown in green color in the barrel and blue color in the endcap. The CSC's, TGC's and RPC's are marked in the plot.

Precision measurements of muon tracks are provided by Monitored Drift Tube (MDT) chambers in most of the detector range. There are three stations of MDT chambers in the barrel ($|\eta| < 1.0$) arranged as three concentric cylinders and four stations in the endcap ($1.0 < |\eta| < 2.7$) arranged as four disks. For the innermost endcap disk in the region $2.0 < |\eta| < 2.7$, the MDT's are replaced with Cathode

Strip Chamber (CSC) to deal with higher particle fluxes.

The MDT's are cathode tubes of diameter 29.970 mm with an anode wire in the center at a potential of 3080 V. The tubes are filled with 93% Ar and 7% CO_2 at a pressure of 3 bar. The secondary ionizations in the gas caused by muons passing by are collected by the wire and the drift time of the charges gives the distance of the muon track to the central wire. On average it can achieve a spatial resolution of ~ 80 μm per tube. Each MDT chamber consists of six to eight layers of MDT's. The CSC's are multi-wire gas chambers, with cathode strip readout. The gas is a mixture of Ar-CO_2 in the ratio 80%-20% and the wire operates at a potential of 1900 V. The spatial resolution of CSC's is ~ 60 μm.

Two types of dedicated fast trigger chambers are employed, the Resistive Plate Chamber (RPC) in the barrel ($|\eta| < 1.0$) and the Thin Gap Chamber (tgc) in the end-cap ($1.0 < |\eta| < 2.4$). Both chambers deliver the track information within a spread of 15-25 ns for triggering. The trigger chambers also complement the measurement of the track coordinates in the non-bending plane with a single hit spatial resolution of 5-10 mm, while precision chambers dominate in measuring the coordinates in the bending plane. The trigger efficiency in the barrel region is slightly lower than the endcap region ($\sim$80% in the barrel and $\sim$95% in the endcap for CB muons) due to smaller geometrical acceptance in the barrel region [34].

The overall performance of the muon spectrometer is expected to achieve a relative momentum resolution better than 3% for a wide range of p_{T} and 10% for a 1 TeV muon when measuring the muon track alone (without the ID).

2.2.6 Trigger System

With a design proton bunch-crossing period of 25 ns, the collisions happen at a rate of 40 MHz, which is way beyond what the readout electronics can handle. Moreover, not all collision events are of interest for physics analysis. A trigger system is thus in need to quickly decide whether an event is interesting and worth recording.

The ATLAS trigger system has a three-level structure, consisting of L1, L2 and the event filter. The L1 trigger uses only a fraction of the total detector information and looks for signatures of high-p_{T} muons, electrons, photons, jets and τ-leptons decaying into hadrons, as well as large missing and total transverse energy. The decision is made through custom-designed on-detector electronics within 2.5 μs to reduce the event rate to about 75 kHz. The L1 trigger also tags a certain number

of Regions-of-Interest (RoI) where it identifies interesting features. The L2 trigger then looks at the RoI's more closely with all the detector information there and reduces the rate to 3.5 kHz. The event filter does offline analysis with an average of four seconds processing time for each event to finally reduce the rate to 400 Hz. A schematic view of the ATLAS trigger system is shown in Figure 2.10 [35].

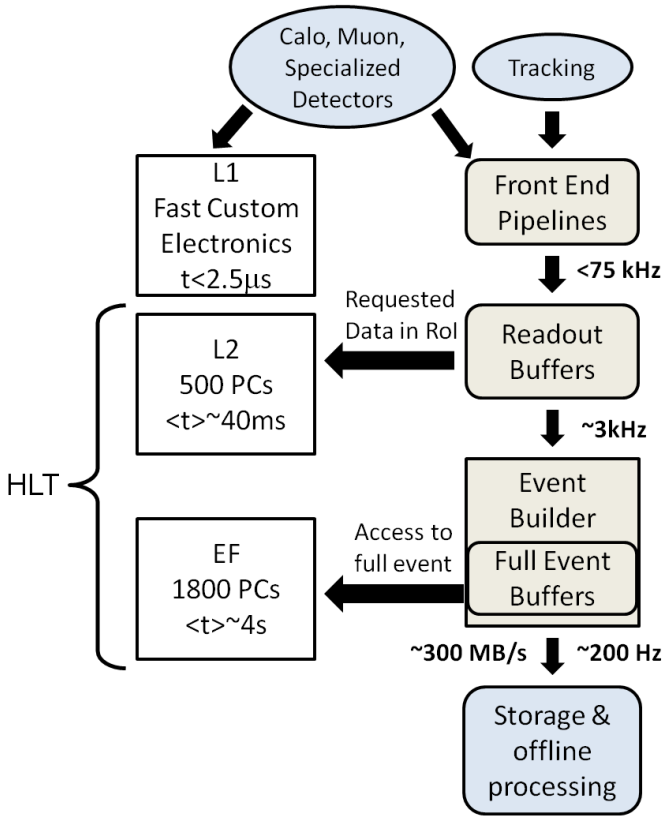

Figure 2.10: Schematic of the ATLAS trigger system.

CHAPTER 3

Object Reconstruction and Identification

In proton-proton collisions, different kinds of particles can be produced. Many are short-lived and decay quickly into other particles, like the W / Z bosons, Higgs boson and top quark. Quarks and gluons hadronize before interacting with the detector. Eventually the detector can only reconstruct a certain range of final state objects. These include electrons, muons, photons, hadronic jets and missing transverse energy and are building blocks for most physics analyses. Different final state objects interact with the ATLAS detector in different ways, as shown briefly in Figure 3.1. In this chapter we discuss the reconstruction and identification of these final state objects used in this thesis.

3.1 Electrons

Electron reconstruction is seeded by energy clusters in the EM calorimeter with at least 2.5 GeV transverse energy. Energy clusters are defined by a *sliding-window* algorithm [36] out of energy showers of size $\Delta\eta \times \Delta\phi = 0.025 \times 0.025$. Seed clusters are then matched to tracks found in the inner detector. When multiple tracks are matched to the same cluster, the one with at least one hit in the Pixel detector is prefered. If more than one track has Pixel hits, the one with the smallest ΔR distance between the extrapolated track in the middle layer of the EM calorimeter and the barycenter of the cluster and with more Pixel hits is chosen as the primary track. All such cluster-track matches are taken as the electron candidates. The electron reconstruction efficiency is shown in Figure 3.2. Each of the candidate clusters is then rebuilt using 3×7 (5×5) cells in $\eta \times \phi$ in the barrel (endcap) of the EM calorimeter. The η and ϕ directions are from the matched track, except for electrons with only tracks having less than four silicon hits the cluster η and ϕ are used. The final electron energy is given by the cluster energy after in-situ calibration using $Z \to ee$ and $J/\psi \to ee$ data events [37]. The electron energy scale

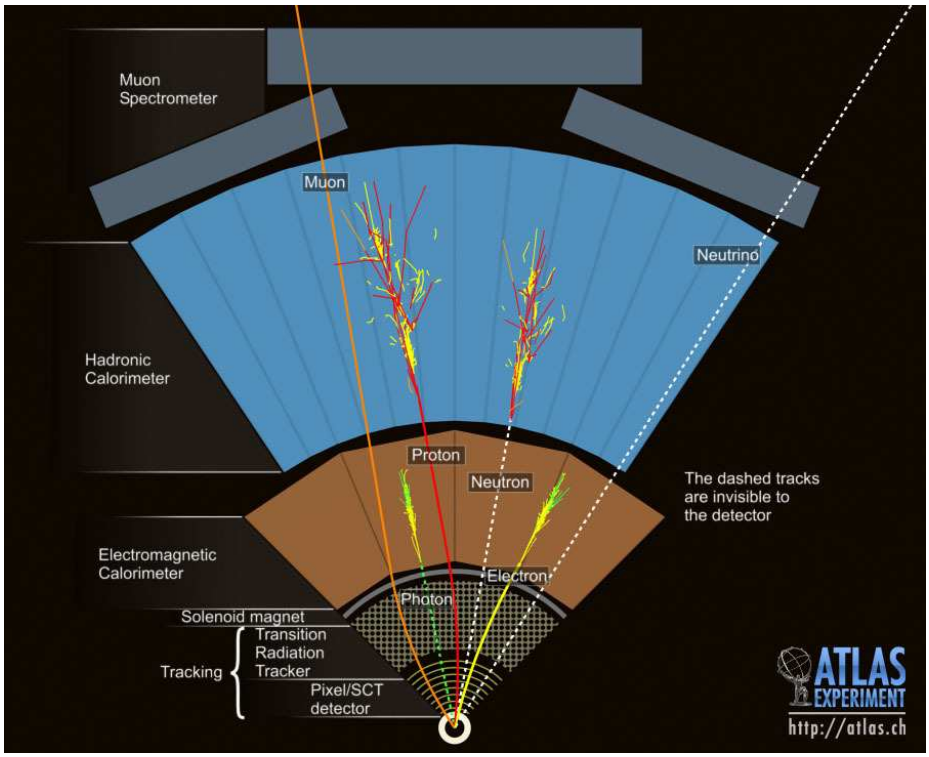

Figure 3.1: Different interactions between final state objects and the detector.

correction applied to the MC simulation is shown in Figure 3.3 together with the uncertainties for central electrons [38]. The electron energy resolution is measured in data and shown in Figure 3.3 for electrons with $|\eta| = 0.2$.

Not all electron candidates are good signal electrons. To suppress background electrons from hadronic jet fakes, photon conversions and hadron decays, a set of electron identification menus are defined based on shower shape of the cluster in the EM calorimeter, the track properties in the inner detector, the matching propertities between the cluster and the track as well as leakage into the hadronic calorimeter and so on. Both cut-based and multivariate-based menus are provided with *loose*, *medium* and *tight* criteria, each giving different signal efficiency and background suppression level. Usually higher signal efficiency also comes with higher background contamination. More details about these identification definitions can be found in Ref. [39] for the 2012 ATLAS data. The efficiencies for different identification menus are shown in Figure 3.4.

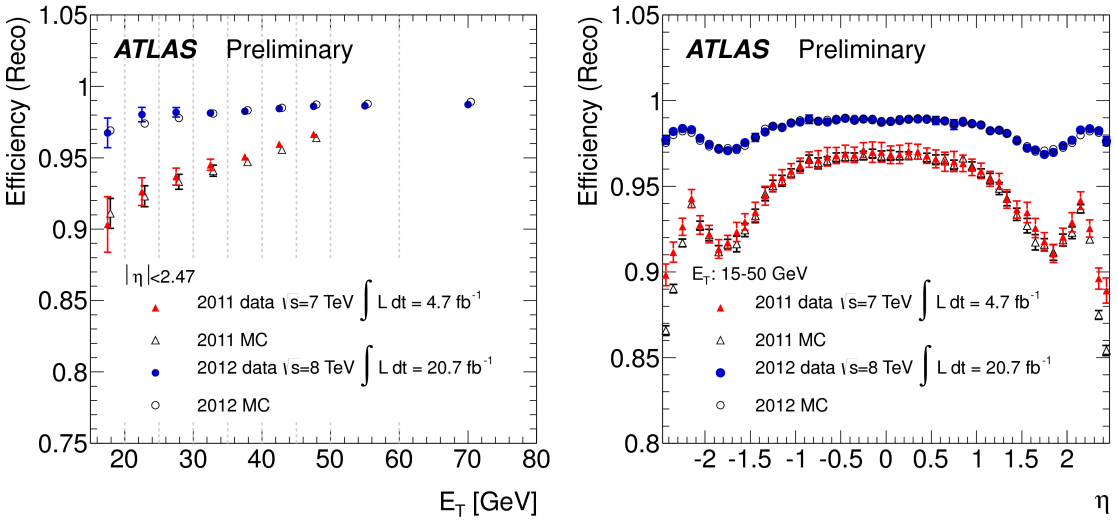

Figure 3.2: Electron reconstruction efficiencies as a function of the electron E_{T} (left) integrated over the whole η range and η (right) for electrons with 15 GeV $< p_{\mathrm{T}} <$ 50 GeV. An improvement in the 2012 run is due to a new track reconstruction algorithm and improved track-cluster matching.

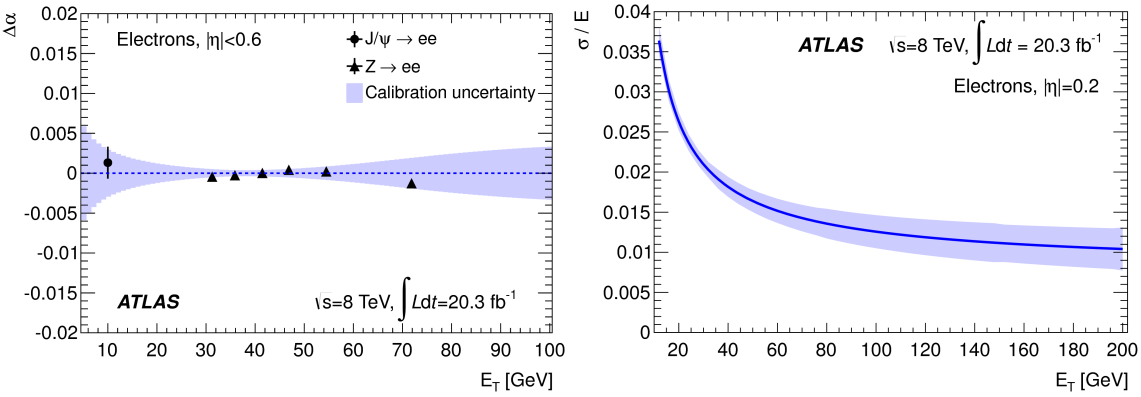

Figure 3.3: Electron energy scale correction factor and its uncertainty as a function of E_{T} for electrons with $|\eta| < 0.6$ (left) and electron energy resolution and its uncertainty as a function of E_{T} for electrons with $|\eta| = 0.2$.

3.2 Muons

The reconstruction of muons mainly relies on the muon spectrometer (MS) and the innder detector (ID) and to a less extent on the calorimeters. Depending on the information available from different sub-detectors for the muon tracks, there are four types of muons reconstructed:

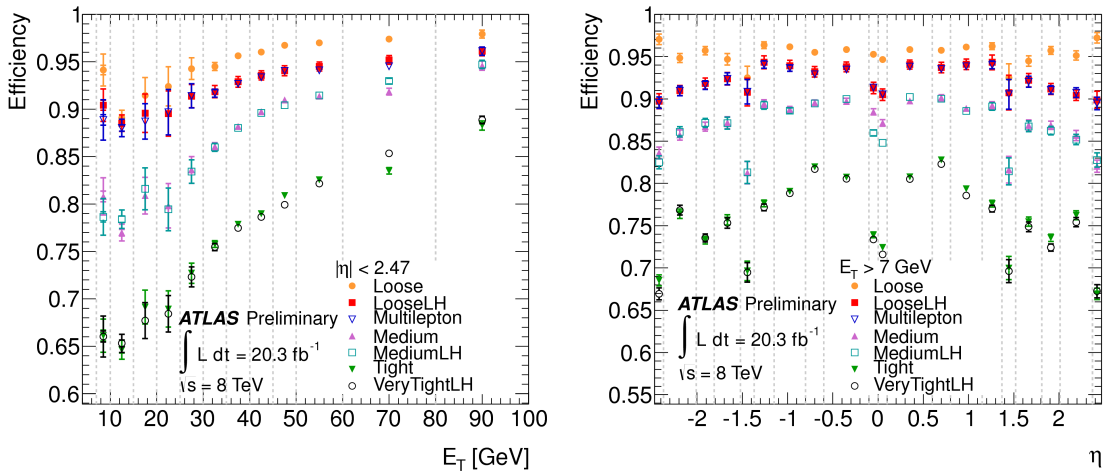

Figure 3.4: Measured combined electron reconstruction and identification efficiencies as a function of the electron E_{T} (left) and η (right). Here "LH" stands for "likelihood" and marks the multivariate-based menus. Only the cut-based "loose" and "tight" menus are used in this thesis.

- Stand-Alone (SA) muons: For the range $2.5 < |\eta| < 2.7$, which is beyond the ID coverage, the muon tracks can only be reconstructed in the MS. The MS track is extrapolated back to the closest point to the beam line to determine the parameters at the interaction point. The energy loss of the muon in the calorimeters is estimated and corrected. In general at least two layers of MS chambers are needed to provide a track measurement.
- Combined (CB) muons: Muons tracks are reconstructed in both the MS and ID and a combination of the two is performed. This is the main type of muons reconstructed and extensively used by most analyses.
- Segment-Tagged (ST) muons: The muon track is only reconstructed in the ID and when extrapolated to the MS it is found to be associated with a local track segment in the MS. These muons only trasverse one layer of MS chamber due to low p_{T} or reduced MS coverage in that area.
- Calorimeter-Tagged (CT) muons: When an ID track is not associated with any MS track segment but found to be associated with energy deposit consistent with an minimum-ionising particle in the calorimenter, it is indentified as a CT muon.

Two different algorithms are available for SA, CB and ST muon reconstruction, the STACO [40], or Chain 1, and the MUID [41], or Chain 2. In this thesis, only CB

and ST muons reconstructed using the STACO algorithm are used. A third chain, which combines the best features of STACO and MUID is also developed for the 2012 data and will be adopted in the future runs.

Some extra requirements on the ID track are usually applied for muons:

- at least one Pixel hit;
- at least five SCT hits;
- at most two active Pixel or SCT sensors traversed by the muon without hits;
- at least five TRT hits if the muon is in the TRT range $0.1 < |\eta| < 1.9$ and the number of outliers should be less than 90% of the total hits;

The first two requirements are loosened accordingly if there are inactive sensors traversed at the time.

The muon reconstruction efficiencies are shown in Figure 3.5 as a function of η and in Figure 3.6 as a function of p_{T} [42]. In Figure 3.7, the di-muon invariant mass distribution for $Z \to \mu\mu$ by selecting two CB muons and the mass resolution as a function of the leading-p_{T} muon η are shown, indicating good performance of the muon momentum measurement.

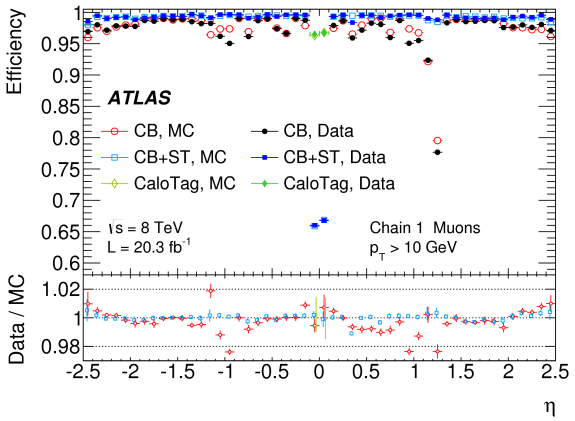

Figure 3.5: Muon reconstruction efficiencies measured in data and simulated $Z \to \mu\mu$ events as a function of η for different muon types (Chain 1). The significant drop in the range $1.0 < \eta < 1.3$ is due to some missing MS chambers not installed until after the 2012 data run.

3.3 Jets

Quarks and gluons hadronize before interacting with the detector due to the QCD confinement and appear as collimated clusters of particles. Such a cluster of parti-

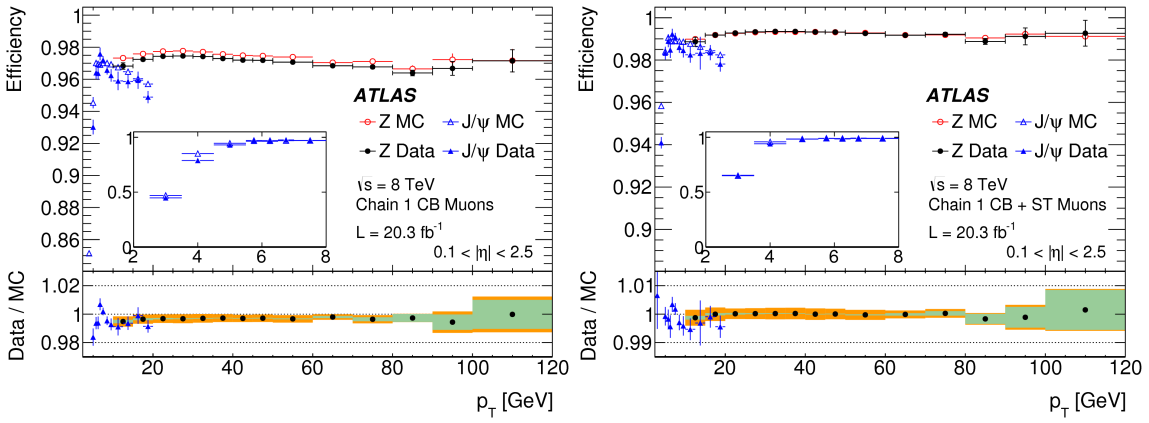

Figure 3.6: Muon reconstruction efficiencies measured in data and simulated $Z \to \mu\mu$ events as a function of p_{T} for CB muons alone (left) and CB+ST muons combined (right).

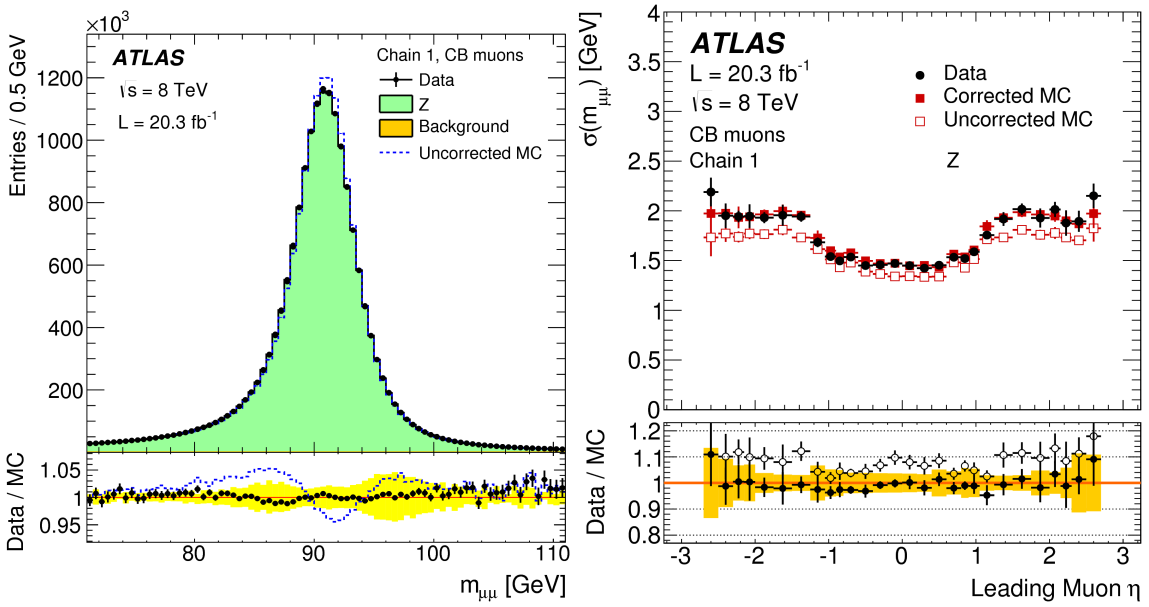

Figure 3.7: Di-muon invariant mass distribution for $Z \to \mu\mu$ reconstructed using CB muons (left) and the mass resolution as a function of the leading-p_{T} muon η (right).

cles is called a *jet*. A specific jet algorithm is needed to define how to cluster either particles (at truth level) or energy deposits (at detector level) to form a single jet. At ATLAS, the anti-k_t clustering algorithm [43] is employed. For an object pair ij

(either particles or energy deposits), two distances are compared:

$$d_{ij} = min(p_{\mathrm{T},i}^{-2}, p_{\mathrm{T},j}^{-2}) \frac{\Delta R_{ij}^2}{R^2}, \tag{3.1}$$

$$d_{iB} = p_{\mathrm{T},i}^{-2}. \tag{3.2}$$

Here $p_{\mathrm{T},i}$ is the transverse momentum of object i, ΔR_{ij} is the spatial distance between the two objects in the $\eta - \phi$ plane and R is a distance parameter. If $d_{ij} < d_{iB}$, the two objects will be combined together. This is done iteratively for all pairs of ij until all possible combinations are done. The distance parameter R used in this thesis is 0.4.

At ATLAS, the most used inputs to the jet clustering algorithm are topological clusters (*topocluster*) of calorimeter energy cells. The topocluster is built up starting from a seed cell which has a signal size above four times of the noise $E_{\mathrm{cell}} > 4\sigma_{\mathrm{cell\ noise}}$. All directly neighbouring cells around the seed cell are collected, independent of their signal significance. If the neighbouring signal is above $2\sigma_{\mathrm{cell\ noise}}$, its neighbours are collected as well. This is done iteractively until all signals are collected. Finally, local maxima are searched for within the topocluster and used as seeds to split it into multiple topoclusters.

The jet energy measurement is calibrated in situ using di-jet, γ+jet, Z+jet and multijet events [44]. The uncertainties on the jet energy scale are shown in Figure 3.8 for 2011 7 TeV data. The fractional jet energy resolution measured in the 2010 7 TeV data is shown in Figure 3.9 [45].

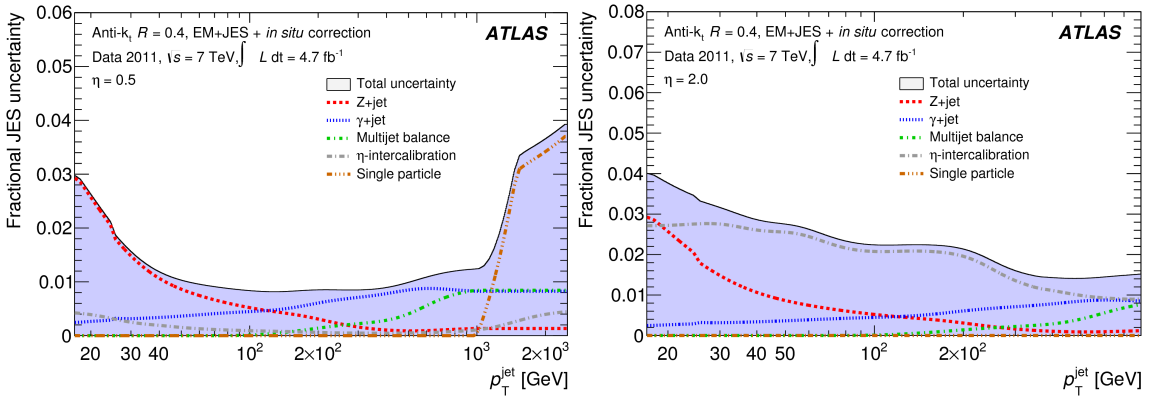

Figure 3.8: Uncertainties on the jet energy scale for central jets with $|\eta| = 0.5$ (left) and forward jets with $|\eta| = 2.0$ (right).

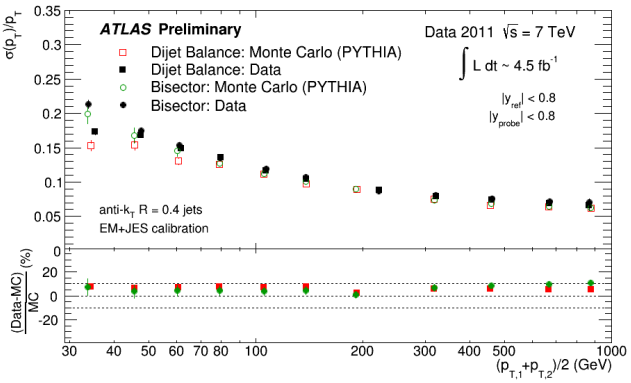

Figure 3.9: Fractional jet energy resolution as a function of the average jet transverse momenta measured with di-jet events. The errors are statistical uncertainties only.

3.4 Missing Transverse Energy

Non-interacting particles, such as neutrinos or potential dark matter candidates, can not be directly detected by the ATLAS detector. Their presence can be infered instead by the imbalance in the observed transverse momenta, the vector sum of which should be exactly zero if all particles have been detected in an event given the conservation of momentum in the transverse plane. The inverse of the vector sum of all transverse momenta is called missing transverse momentum, the magnitude of which is taken as the missing transverse energy, corresponding to a massless particle.

At ATLAS, different kinds of inputs can be used to calculate $E_{\mathrm{T}}^{\mathrm{miss}}$. The $E_{\mathrm{T}}^{\mathrm{miss}}$ used in this thesis is calculated using reconstructed and calibrated physics objects [46]. The energy deposits in the calorimeters are associated with identified and calibrated high-p_{T} objects in the following order: electrons, photons, hadronically-decaying τ-leptons, jets and muons. Jets with $p_{\mathrm{T}} < 20$ GeV, calorimeter topoclusters and tracks not associated with any high-p_{T} objects are also included in the calculation and make up the soft terms. The definition of missing transverse momentum can be put as:

$$E_{x(y)}^{\mathrm{miss}} = E_{x(y)}^{\mathrm{miss},e} + E_{x(y)}^{\mathrm{miss},\gamma} + E_{x(y)}^{\mathrm{miss},\tau} + E_{x(y)}^{\mathrm{miss,jets}} + E_{x(y)}^{\mathrm{miss},\mu} + E_{x(y)}^{\mathrm{miss,SoftTerm}} \tag{3.3}$$

and the missing transverse energy is $E_{\mathrm{T}}^{\mathrm{miss}} = \left|\vec{E}_{\mathrm{T}}^{\mathrm{miss}}\right|$.

The presence of pileup events spoils the balance in the transverse momenta and worsens the $E_{\mathrm{T}}^{\mathrm{miss}}$ resolution. The $E_{x,y}^{\mathrm{miss}}$ resolution as a function of the total summed E_{T} of minimum biase events in 2012 data is shown in Figure 3.10 for $E_{\mathrm{T}}^{\mathrm{miss}}$ calculation with and without pileup suppression techniques [46].

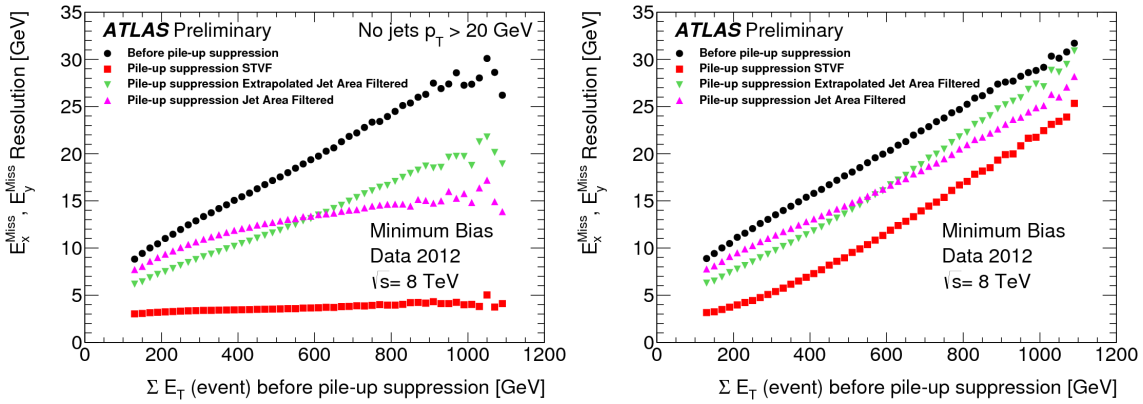

Figure 3.10: E_x^{miss} and E_y^{miss} resolution as a function of the E_{T} sum of the event for minimum biase events in 2012 data without 20 GeV jets (left) and inclusively (right). Improvement is observed after introducing pileup suppression techniques.

3.5 Flavor Tagging

The relatively long life time of b quark gives jets originating from b quark hadronization unique features to be separated from jets of other flavors. At ATLAS, different algorithms have been developed for b-tagging, based on impact parameters (IP3D) [47], secondary vertices (SV1) [48] and decay chain (JetFitter) [49]. A more extensively used algorithm, MV1, uses multivariate technique to combine the most discriminating variables from the above algorithms and further enhance the tagging performance. The b-tagging efficiency is shown in Figure 3.11 as a function of the jet p_{T} for the MV1 tagger at the 70% efficiency point [50]. The mis-tag rate for light jets is shown in Figure 3.12 for the same tagger at the same operation point [51].

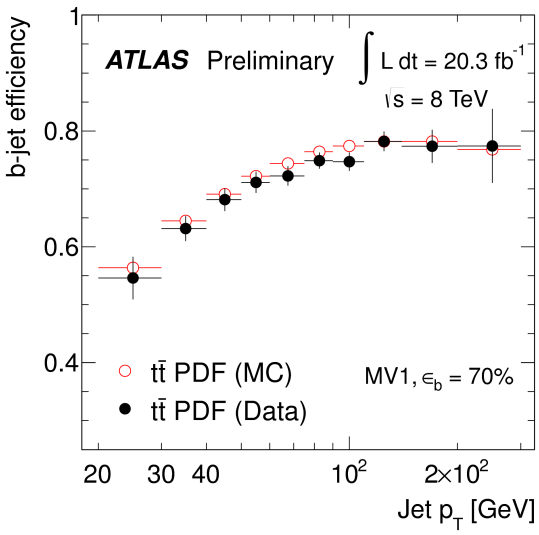

Figure 3.11: The tagging efficiency for b-jets using the MV1 tagging tool at the 70% efficiency operating point as a function of the b-jet p_{T}.

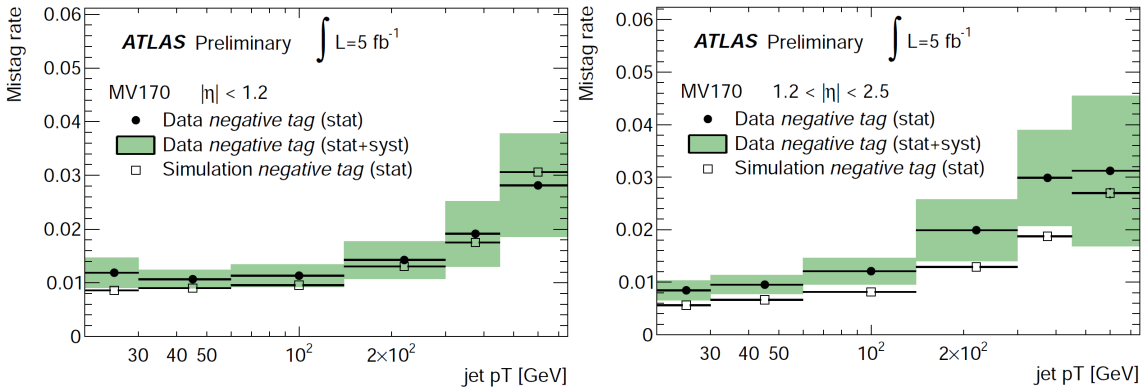

Figure 3.12: The mis-tag rate for light jets using the MV1 tagging tool at the 70% efficiency operating point as a function of the jet p_{T} for jets with $|\eta| < 1.2$ (left) and $1.2 < |\eta| < 2.5$ (right). The mis-tag rate is obtained using the negative tag method as in Ref. [51].

CHAPTER 4

$W^{\pm}W^{\pm}jj$ Cross Section Measurement

4.1 Introduction

This chapter presents the measurement of the same-sign $W^{\pm}W^{\pm}jj$ production cross section. In general, VBS processes are produced at the LHC through the diagrams shown in Figure 4.1. The VBS production alone is not gauge invariant [52]. Other diagrams as shwon in Figure 4.2 with the same order of α_{EW} need to be included. These diagrams only involve electroweak vertices and are called electroweak production. For the same final state of particles, events can be produced involving QCD vertices, as shown in Figure 4.3. These are called the strong production. The electroweak production is of better interest since it contains the VBS processes. The presence of QGC vertex in the electroweak production also provides the sensitivity to aQGC.

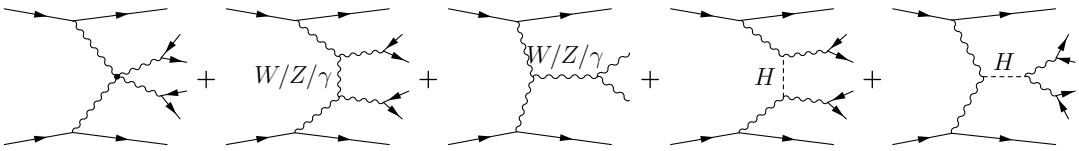

Figure 4.1: Feynman diagrams of VBS production at the LHC. All these diagrams have $\mathcal{O}(\alpha_{\mathrm{EW}}^{6})$ dependence. The s-channel diagrams do not exist for same-sign $W^{\pm}W^{\pm}jj$ final state.

At the LHC, the relative ratio between electroweak production and strong production differs greatly depending on the final state. Using SHERPA [53–56] MC generator, the production cross sections are compared in Table 4.1. The same-sign $W^{\pm}W^{\pm}$ is the one with the largest electroweak to strong ratio due to the lack of leading-order gg/gq initial state production and thus the best candidate for a first study of VBS at the LHC.

The same-sign $W^{\pm}W^{\pm}$ VBS event topology features the presence of two tagging

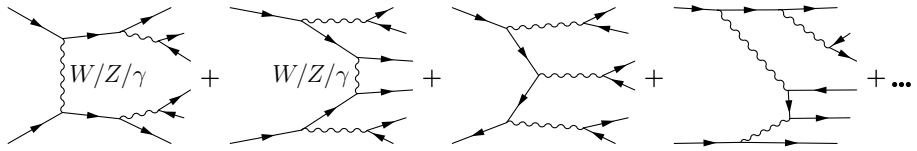

Figure 4.2: Non-VBS production of the $VVjj$ final state with $\mathcal{O}(\alpha_{\mathrm{EW}}^{6})$. The first two diagrams from the left are not gauge-invariantly seperable from VBS production. The two diagrams on the right (tri-W production and non-resonant production) can be suppressed in the event selections. This list is not exaustive but more diagrams exist than displayed here.

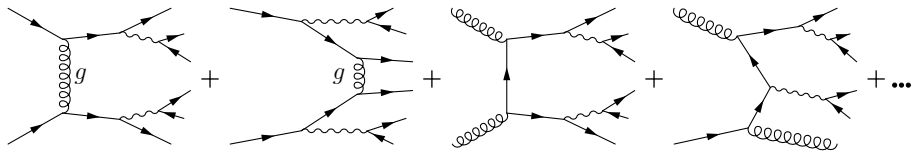

Figure 4.3: Strong production of the $VVjj$ final state with $\mathcal{O}(\alpha_{\mathrm{EW}}^{4})\mathcal{O}(\alpha_{\mathrm{S}}^{2})$. This list is not exaustive but more diagrams exist than displayed here. The gluon-quark and gluon-gluon initial state diagrams do not exist for same-sign $W^{\pm}W^{\pm}jj$ final state.

forward jets, two same-electric-charge isolated leptons and large missing transverse energy due to neutrinos, as shown in Figure 4.4. The two tagging jets are largely separated in rapidity due to the lack of color exchange between the two incoming partons and result in large di-jet invariant mass. This is one of the most unique signatures for VBS processes at LHC. A generator-level comparison of electroweak and strong production of $W^{\pm}W^{\pm}jj$ is shown in Figure 4.5 for the invariant mass and rapidity gap of the two leading jets.

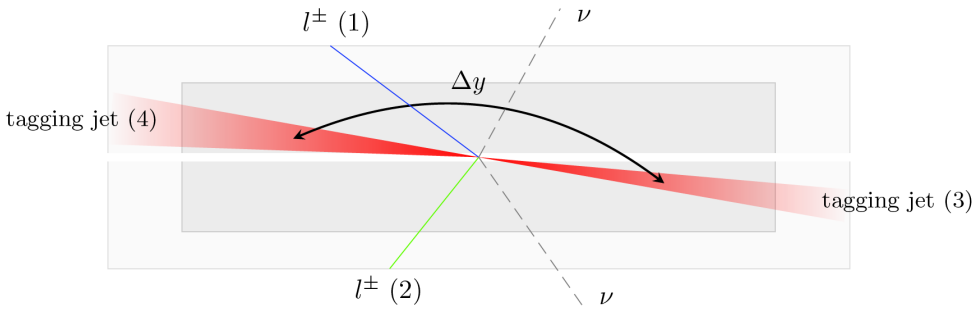

Figure 4.4: VBS event topology in the ATLAS detector.

final state	process	Ewk. [fb]	Strong [fb]	Ewk./Strong
$\ell^{\pm}\nu\ell'^{\pm}\nu' jj$ (same sign)	$W^{\pm}W^{\pm}$	19.5	18.8	1.04
$\ell^{\pm}\nu\ell'^{\mp}\nu' jj$ (opposite sign)	$W^{\pm}W^{\mp}$	91.3	3030	0.030
$\ell^{\pm}\ell^{\mp}\ell'^{\pm}\nu' jj$	$W^{\pm}Z$	30.2	687	0.043
$\ell^{\pm}\ell^{\mp}\ell'^{\pm}\ell'^{\mp} jj$	ZZ	1.5	106	0.014
$\ell^{+}\ell^{-}\nu'\nu' jj$	ZZ	2.4	162	0.015

Table 4.1: Production cross sections of different $VVjj$ final states at 8 TeV and the ratio between the electroweak and strong production. The calculation is done using SHERPA MC generator at leading order. Two generator-level leptons with $p_{\mathrm{T}} > 5$ GeV are required with the dilepton invariant mass $m_{\ell\ell} > 4$ GeV. At least two jets with $p_{\mathrm{T}} > 10$ GeV are required.

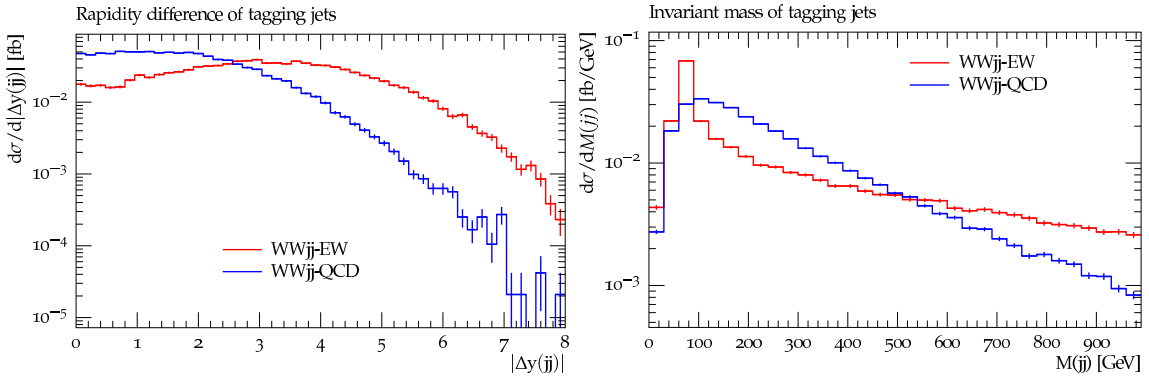

Figure 4.5: Generator-level comparison between electroweak and strong production of $W^{\pm}W^{\pm}jj$. Here the rapidity separation (left) and invariant mass (right) of the two leading jets are shown. All histograms are normalized to unity area. The electroweak production has a clear feature of large rapidity separation and high di-jet invariant mass, which is characteristic for VBS.

Given the fact that the combined electroweak and strong production of $W^{\pm}W^{\pm}jj$ has never been observed at LHC before, the analysis goal is set to measure the inclusive production cross section and also to extract the electroweak component. Limits on the aQGC will also be set.

4.2 Data Set

This analysis is performed on the proton-proton collision data set collected in the 2012 operation, corresponding to an integrated luminosity of 20281.4 pb^{-1} with an uncertainty of 2.8% [57]. The events are selected using a set of unprescaled sin-

gle lepton triggers with the lowest p_{T} threshold, `EF_e24vhi_medium1` for events with at least one electron and `EF_mu24i_tight` for events with at least one muon. `EF_e60_medium1` and `EF_mu36_tight` are also used for leptons with high p_{T} to increase the efficiency. A Good Runs List (GRL) is created depending on the detector run condition and the data quality. Only events with the luminosity blocks containted in the GRL are selected.

4.3 Signal Simulation

Monte Carlo (MC) simulation serves as a bridge from the theory to experiment. Different MC samples have been used in this analysis for understanding signals and estimating backgrounds. The MC sample production starts with the generation of truth level events, which are then passed on to detector response simulation based on GEANT4 [58]. Additional collision events are simulated using PYTHIA [59, 60] and added to the primary event to account for pileup. Finally the same reconstruction as used for the data sample is done for the MC sample. In this section we summarize the simulation of the signal $W^{\pm}W^{\pm}jj$-Ewk and $W^{\pm}W^{\pm}jj$-Strong production. Other MC samples are introduced in Section 4.6 when discussing background estimations. A summary of all MC samples used can be found in Appendix A.

The $W^{\pm}W^{\pm}jj$-Ewk and $W^{\pm}W^{\pm}jj$-Strong production is simulated using the SHERPA [53–56] generator at leading-order QCD with up to one extra parton. A Matrix Element and Parton Shower (MEPS) merging is carried out to remove duplications between real emmissions and parton shower [61] as implemented in SHERPA. The electroweak production is done by fixing the order of electroweak coupling to 6. The strong production instead has electroweak coupling at the order of 4. The CT10 parton distribution function (PDF) [62] is used for both samples. The renormalization and factorization scales are determined for each event dynamically [61].

Next-leading-order (NLO) calculation is available from POWHEG-BOX [63–69] for both electroweak and strong production and VBFNLO [66, 70–72] for electroweak production. POWHEG-BOX can output events at NLO while VBFNLO can only output LO events but can do NLO integration for cross section calculation with configurable selections at parton level. The SHERPA MC samples are eventually normalized to NLO cross sections in the fiducial signal regions as defined

in Section 4.4 calculated using POWHEG-BOX. More details about the calculations and related systematic uncertainty evaluation are discussed in Section 4.5 after we define the fiducial signal regions.

4.4 Event Selection

4.4.1 Fiducial Signal Region Definition

Two *fiducial signal region* definitions are used in this analysis for the fiducial cross section measurements, one for the inclusive production of $W^{\pm}W^{\pm}jj$ and the other for the electroweak production. Fiducial region, or fiducial phase space, is defined at the truth particle level using MC simulation, before adding in the detector response simulation and reconstruction. Results obtained for fiducial region is thus independent of the detector effects and can be more easily compared for different theoretical models. The fraction of total signal events selected into the fiducial region is called *signal acceptance* and the fraction of events in the fiducial region selected at the detector level is called *detector efficiency*. Fiducial region selections are defined as close as possible to the detector level selections, which will be discussed later in Section 4.4.8.

The ***Inclusive Fiducial Signal Region*** is defined as:

- Two leptons (e or μ) with $p_{\mathrm{T}} > 25$ GeV and $|\eta| < 2.5$;
- Same electric charge for the two leptons and dilepton invariant mass $m_{\ell\ell'} > 20$ GeV;
- The two leptons are separated with $\Delta R > 0.3$;
- The missing transverse energy due to neutrinos $E_{\mathrm{T}}^{\mathrm{miss}} > 40$ GeV;
- At least two jets with $p_{\mathrm{T}} > 30$ GeV and $|\eta| < 4.5$;
- The leptons and jets must be all separated with $\Delta R > 0.3$;
- The two jets with the highest p_{T} have invariant mass $m_{jj} > 500$ GeV.

The ***VBS Fiducial Signal Region*** is defined by adding one more cut:

- The two leading jets are separated with $\Delta y(jj) > 2.4$.

Here leptons are the truth level final state electrons and muons, after parton shower, QED final state radiation and tau lepton decay. The two leptons with the highest p_{T} are selected as the candidate leptons. The selected leptons are then dressed with photons within $\Delta R = 0.1$ by adding the four-momenta of the photon to the original particle, to account for the QED radiation. Events with any

selected leptons from tau decays are vetoed. (These events are however selected in the nominal analysis.) This accounts for about 10% of total events in the fiducial region and is left into the detector efficiency. Jets are clustered using anti-k_t algorithm with a distance parameter $R = 0.4$, using all final state particles as the input excluding neutrinos and muons. Jets overlapping with electrons within $\Delta R = 0.05$ are removed. The signal acceptances into the fiducial regions are calculated using `RIVET` as in Ref. [73].

4.4.2 Reconstructed Vertices and Pileup Correction

The proton beam at the LHC is organized in bunches. During the 2012 run, each bunch is spaced 50 ns to the next one. During each bunch crossing, multiple collisions can happen and thus more than one vertex are reconstructed in a single recorded event. The vertex with the largest sum of squared transverse momenta of associated tracks is chosen as the primary vertex. The collision events associated with the vertices other than the primary vertex are called *in-time pileup* events. The detector can be also affected by collision events which happen in neighbouring bunch crossings. This is called *out-of-time pileup*.

The MC samples are usually produced before all data taking is finished and a setup of the average number of interactions per bunch crossing can be only guessed before hand. When analyzing the data, the MC distribution of average number of interactions per bunch crossing is then reweighted at the event level to account for the difference observed in data. The data distribution is scaled by a factor of $1/1.09$ before the reweighting to account for differences in the ATLAS detector fiducial cross section between data and MC in studies of minimum bias events.

4.4.3 Muons

Three different muon selection definitions are used in this analysis.

1. **Nominal Muons**: Nominal muons are used for the selection of muons from the signal W decay.
   - Reconstructed as combined (CB) muons using the STACO algorithm;
   - With $p_{\mathrm{T}} > 25$ GeV and $|\eta| < 2.5$;
   - Muon ID track requirements as specified in Section 3.2;
   - ID and MS tracks have the same charge;

- Consistent with originating from the primary vertex with the impact parameters: $|z_0 \times \sin\theta| < 0.5$ mm and $d_0/\sigma_{d_0} < 3$;
- Isolated in the calorimeter: $\sum_{\Delta R<0.3} E_{\mathrm{T}}/p_{\mathrm{T}}(\mu) < 0.07$;
- Isolated in the inner detector: $\sum_{\Delta R<0.3} p_{\mathrm{T}}/p_{\mathrm{T}}(\mu) < 0.07$.

In the isolation requirement, the sum runs over all energy deposits or tracks within a cone of $\Delta R = 0.3$ around the muon, excluding the energy deposit and the tracks associated with the muon in consideration. Later in this thesis, $\sum_{\Delta R<0.3} E_{\mathrm{T}}$ is also refered to as $E_{\mathrm{T}}^{\mathrm{cone30}}$ and $\sum_{\Delta R<0.3} p_{\mathrm{T}}$ refered to as $p_{\mathrm{T}}^{\mathrm{cone30}}$.

2. **Veto Muons**: Veto muons are used for vetoing events with a third lepton. The p_{T} is lowered and other quality cuts are loosened.
   - Reconstructed as combined (CB) or segment-tagged (ST) muons using the STACO algorithm;
   - With $p_{\mathrm{T}} > 6$ GeV and $|\eta| < 2.5$;
   - Muon ID track requirements as specified in Section 3.2;
   - Consistent with originating from the primary vertex with the impact parameters: $|z_0 \times \sin\theta| < 0.5$ mm and $d_0/\sigma_{d_0} < 3$;
   - Isolated in the inner detector: $\sum_{\Delta R<0.3} p_{\mathrm{T}}/p_{\mathrm{T}}(\mu) < 0.15$.
3. **Loose Muons**: Loose muons are used in the non-prompt background estimation, which will be discussed in Section 4.6.2. Compared to the nominal definitions, the isolation requirements are both reversed. The impact parameter requirements are loosened to avoid anti-correlations. Muons selected using this definition are dominated by non-prompt muons from hadron decay.
   - Reconstructed as combined (CB) muons using the STACO algorithm;
   - With $p_{\mathrm{T}} > 25$ GeV and $|\eta| < 2.5$;
   - Muon ID track requirements as specified in Section 3.2;
   - ID and MS tracks have the same charge;
   - Impact parameters: $|z_0 \times \sin\theta| < 5$ mm and $d_0/\sigma_{d_0} < 10$;
   - Non-isolated in the calorimeter: $0.07 < \sum_{\Delta R<0.3} E_{\mathrm{T}}/p_{\mathrm{T}}(\mu) < 2$;
   - Non-isolated in the inner detector: $0.07 < \sum_{\Delta R<0.3} p_{\mathrm{T}}/p_{\mathrm{T}}(\mu) < 2$.

4.4.4 Electrons

As for muons, there are also three electron selection definitions used in this analysis.

1. **Nominal Electrons**: Nominal electrons are used for the selection of electrons from the signal W decay.
   - Reconstructed as *tight* electrons [39];
   - With $E_{\mathrm{T}} > 25$ GeV, $|\eta| < 2.47$ and not in $1.37 < |\eta| < 1.52$;
   - Consistent with originating from the primary vertex with the impact parameters: $|z_0 \times \sin\theta| < 0.5$ mm and $d_0/\sigma_{d_0} < 3$;
   - Isolated in the calorimeter: $\sum_{\Delta R<0.3} E_{\mathrm{T}}/E_{\mathrm{T}}(e) < 0.14$;
   - Isolated in the inner detector: $\sum_{\Delta R<0.3} p_{\mathrm{T}}/E_{\mathrm{T}}(e) < 0.06$;
2. **Veto Electrons**: Veto electrons are used for vetoing events with a third lepton. The E_{T} is lowered and other quality cuts are loosened.
   - Reconstructed as *loose* electrons [39];
   - With $E_{\mathrm{T}} > 7$ GeV, $|\eta| < 2.47$ and not in $1.37 < |\eta| < 1.52$;
   - Consistent with originating from the primary vertex with the impact parameters: $|z_0 \times \sin\theta| < 0.5$ mm and $d_0/\sigma_{d_0} < 3$;
   - Isolated in the inner detector: $\sum_{\Delta R<0.3} p_{\mathrm{T}}/E_{\mathrm{T}}(e) < 0.13$;
3. **Loose Electrons**: Loose electrons are used in the non-prompt background estimation, which will be discussed in Section 4.6.2. Compared to the nominal definitions, the isolation requirements are both reversed. The impact parameter requirements are loosened to avoid anti-correlations. Electrons selected using this definition are dominated by non-prompt electrons from hadron decay or jets mis-reconstructed as electrons.
   - Reconstructed as *loose* electrons [39];
   - With $E_{\mathrm{T}} > 25$ GeV, $|\eta| < 2.47$ and not in $1.37 < |\eta| < 1.52$;
   - Impact parameters: $|z_0 \times \sin\theta| < 5$ mm and $d_0/\sigma_{d_0} < 10$;
   - Non-isolated in the calorimeter: $0.14 < \sum_{\Delta R<0.3} E_{\mathrm{T}}/E_{\mathrm{T}}(e) < 2$;
   - Non-isolated in the inner detector: $0.06 < \sum_{\Delta R<0.3} p_{\mathrm{T}}/E_{\mathrm{T}}(e) < 2$;

4.4.5 Jets

Jets are reconstructed using calorimeter topoclusters with the anti-k_t algorithm [43] and distance parameter $R = 0.4$. The jet energy is calibrated to hadronic scale using the EM+JES scheme as in Ref. [74]. Jets are required to have:

- $p_{\mathrm{T}} > 30$ GeV, $|\eta| < 4.5$;
- For a jet with $p_{\mathrm{T}} < 50$ GeV and $|\eta| < 2.4$, the summed p_{T} of tracks which are matched with the jet and are associated with the primary vertex must be

more than 50% of the total summed p_{T} of all tracks matched to the jet. This is to suppress jets from pileup events and this cut is refered to as Jet Vertex Fraction (JVF) cut.

Jets passing the above requirements are also considered for b-jet candidate, using the MV1 tagger at the 70% efficiency point [50].

4.4.6 Missing Transverse Energy

The missing transverse energy $E_{\mathrm{T}}^{\mathrm{miss}}$ is reconstructed using calibrated final state objects and calorimeter topoclusters and tracks not associated with any objects as specified in Section 3.4.

4.4.7 Overlapping Object Treatment

Overlapping objects can be found when one particle is identified by different reconstruction algorithms at the same time or different particles happen to overlap in the same detector region. The following procedure is taken to deal with overlapping objects:

1. e/jet overlap: Since electrons are reconstructed using calorimeter clusters which are also always reconstructed as jets, when a jet is found to be within $\Delta R = 0.3$ around a selected electron, the jet is discarded;
2. e/μ overlap: Photons radiated from muons can convert to electron pairs. When an electron is found to be within $\Delta R = 0.1$ around a selected muon, the electron is discarded;
3. μ/jet overlap: Non-prompt muons can come from hadron decays. When a selected muon is found to be within $\Delta R = 0.3$ around a selected jet, the event is likely to be a non-prompt background and is thus discarded.

The above procedure only concerns the selected nominal leptons as defined in the previous sections. For veto electrons (muons), they are discarded only if they overlap with nominal electrons (muons) after the above overlap removal. The overlap removal concerning loose leptons in the non-prompt background estimation will be discussed in Section 4.6.2.

4.4.8 Signal Region Definition

Apart from the trigger and GRL requirements as specified in Section 4.2, a few other data quality criteria are applied:

- Imcomplete and corrupted events are discarded as specified in Ref. [75].
- Events containing jets of bad quality are rejected. Bad jets can affect the reconstruction of $E_{\mathrm{T}}^{\mathrm{miss}}$.
- The primary vertex of the event must have at least three associated tracks with $p_{\mathrm{T}} > 0.5$ GeV.

Given the $W^{\pm}W^{\pm}jj \rightarrow \ell^{\pm}\nu\ell^{\pm}\nu jj$ final state, we expect two isolated high-p_{T} leptons with the same electric charge in the signal event. Depending on the flavor of the two leptons, three channels are considered and they are ee channel, $e\mu$ channel and $\mu\mu$ channel. Due to the presence of neutrinos, large $E_{\mathrm{T}}^{\mathrm{miss}}$ is expected. The two tagging jets are unique features of VBS events. For electroweak production of $W^{\pm}W^{\pm}jj$, the invariant mass of the two tagging jets is expected to be high and the rapidity gap between the two jets is large. To suppress backgrounds which produce more than two leptons, no third lepton is allowed in the event to pass the veto lepton definition. To suppress Z+jets background in the ee channel, the di-electron invariant mass is required to be out of the Z mass window with $|m_{ee} - m_Z| > 10$ GeV. To suppress backgrounds involving top quark, no b-jet candidate is allowed to be present in the event.

The ***inclusive signal region*** is then defined as:

- exactly two selected nominal leptons (electrons or muons)
- no veto leptons in the event
- same electric charge for the two nominal leptons
- invariant mass of the nominal leptons $m_{\ell\ell'} > 20$ GeV
- for events with two nominal electrons, $|m_{ee} - m_Z| > 10$ GeV
- $E_{\mathrm{T}}^{\mathrm{miss}} > 40$ GeV
- at least two jets
- no b-jet candidate
- the invariant mass of the two highest-p_{T} jets $m_{jj} \geq 500$ GeV

The ***VBS signal region*** is defined by adding one more cut:

- the rapidity gap between the two highest-p_{T} jets $\Delta y(jj) > 2.4$.

For validating the background estimations, different control regions are also defined, each characterizing the unique features of the specific background under consideration. The definitions of these control regions will be discussed in details

in Section 4.6.

4.5 Signal Production Cross Section in Fiducial Regions

4.5.1 $W^{\pm}W^{\pm}jj$-Ewk

A comparison of the fiducial signal region cross sections defined at parton level (before parton showering) is shown for POWHEG-BOX and VBFNLO in Table 4.2. The relative difference 5% and 3% is taken as a systematic uncertainty on the cross section in the Inclusive Fiducial SR and VBS Fiducial SR.

	$\sigma_{W^{\pm}W^{\pm}jj-\text{Ewk}}$ [fb]	
	Inclusive Fiducal SR	VBS Fiducial SR
VBFNLO	0.5131±0.0008	0.456±0.001
POWHEG-BOX	0.541±0.007	0.472±0.007
VBFNLO/POWHEG-BOX	0.95±0.01	0.97±0.01

Table 4.2: Production cross sections of electroweak $W^{\pm}W^{\pm}jj$ in fiducial signal regions calculated at NLO parton level using VBFNLO and POWHEG-BOX without parton showering. Only the $e^{\pm}\mu^{\pm}$ final state is included here.

The parton shower effects are checked by interfacing POWHEG-BOX NLO events to different parton shower MC generators:

- PYTHIA8 [60] for parton shower, hadronization and underlying event
- HERWIG++ [76] for parton shower and hadronization and JIMMY for underlying event

The fiducial region cross sections calculated at particle level after the above parton showering are shown in Table 4.3, along with the parton level cross section before parton showering. The correction in the fiducial cross sections after introducing parton shower, hadronization and underlying event is found to be mainly from parton shower effects. The POWHEG-BOX+PYTHIA8 is taken as the baseline and the relative difference between PYTHIA8 and HERWIG++/JIMMY is taken as the systematic uncertainty.

The uncertainties associated with the renormalization and factorization scales are evaluated using VBFNLO at NLO parton level, which is the only practical option given the computing CPU hours needed. In VBFNLO, the renormalization and factorization scale is chosen dynamically for each event as the momentum transfer of the exchanged W/Z bosons. The scales are varied independently by

	$\sigma_{W^\pm W^\pm jj-\text{Ewk}}$ [fb]	
	Inclusive Fiducal SR	VBS Fiducial SR
POWHEG-BOX(parton level)	1.081±0.015	0.945±0.015
POWHEG-BOX+PYTHIA8	1.003±0.015	0.881±0.014
POWHEG-BOX+HERWIG++/JIMMY	1.025±0.015	0.905±0.014
SHERPA(parton level)	1.200±0.014	1.019±0.013
SHERPA(particle level)	1.113±0.014	0.940±0.013

Table 4.3: NLO production cross section of electroweak $W^\pm W^\pm jj$ in the two fiducial signal regions calculated using POWHEG-BOX at parton level and particle level using different parton shower models. The $e^\pm\mu^\pm$ final state is used for the calculation and a factor of two has been multiplied to account for other final states, excluding the tau final states. The LO cross sections calculated using SHERPA at parton level and particle level are also shown for comparison.

a factor of 0.5 or 2 to estimate the uncertainties. Table 4.4 shows the result of all variation combinations. A 1.5% uncertainty is assigned for both regions to cover the largest deviation observed.

		$\sigma_{W^\pm W^\pm jj-\text{Ewk}}$ [fb]	
ξ_R	ξ_F	Inclusive Fiducial SR	VBS Fiducial SR
1	1	0.2571±0.0004	0.2277±0.0005
0.5	0.5	0.2532±0.0008(-1.5%)	0.2265±0.0004(-0.5%)
1	0.5	0.2577±0.0006(+0.2%)	0.2306±0.0004(+1.4%)
2	0.5	[0.2618±0.0006(+1.8%)]	[0.2320±0.0004(+1.9%)]
0.5	1	0.2566±0.0006(-0.2%)	0.2293±0.0008(+0.7%)
2	1	0.2579±0.0006(+0.3%)	0.2292±0.0005(+0.7%)
0.5	2	[0.2582±0.0005(+0.4%)]	[0.2301±0.0004(+1.1%)]
1	2	0.2559±0.0005(-0.5%)	0.2279±0.0004(+0.9%)
2	2	0.2549±0.0005(-0.9%)	0.2267±0.0003(-0.4%)
Max.		+0.3%, -1.5%	+1.3%, -0.5%

Table 4.4: Fiducial cross section at NLO parton level with the nominal dynamic renormalization scale varied by a factor of ξ_R and the factorization scale varied by a factor of ξ_F. The cross section is for $e^\pm e^\pm$ final state only. The largest deviation from the nominal setup ($\xi_R = \xi_F = 1$) among all combinations, excluding the case when two scales are varied in opposite directions, is given in the bottom row in percentage.

The PDF uncertainties are also evaluated using VBFNLO. Each of the 26 eigen-

vectors of CT10 PDF is varied up and down and the error is calculated as:

$$\Delta\sigma^{+}_{\max} = \sqrt{\sum_{i=1}^{26}[max(\sigma_i^{+} - \sigma_0, \sigma_i^{-} - \sigma_0, 0)]^2}, \tag{4.1}$$

$$\Delta\sigma^{-}_{\max} = \sqrt{\sum_{i=1}^{26}[max(\sigma_0 - \sigma_i^{+}, \sigma_0 - \sigma_i^{-}, 0)]^2}, \tag{4.2}$$

where σ_0 is the cross section calculated using central values of CT10 PDF and $\sigma_i^{+,-}$ is the cross section with eigenvector i varied up and down. The variations for CT10 eigenvectors correspond to 90% confidence level (CL) intervals and the resulting variations on the cross section are scaled by a factor of 1.645 to obtain the 68% CL uncertainties. The PDF set MSTW2008 [77–79] is also compared to CT10 as a cross check but not used as a systematic uncertainty. The results are shown in Table 4.5. A 2% and 3% systematic uncertainty is assigned to the inclusive fiducial cross section and VBS fiducial cross section respectively.

	CT10 Eigenvector Variation	CT10 - MSTW2008
Inclusive Fiducial SR	+2.0%, -1.7%	2.7%
VBS Fiducial SR	+2.9%, -1.5%	2.4%

Table 4.5: PDF uncertainties on the $W^{\pm}W^{\pm}jj$-Ewk production cross section in fiducial regions due to CT10 eigenvector variations. The difference between CT10 and MSTW2008 is also shown for comparison but not quoted as systematic uncertainty.

The systematic uncertainties are summarized for $W^{\pm}W^{\pm}jj$-Ewk production cross sections in the two fiducial regions in Table 4.6.

$W^{\pm}W^{\pm}jj$-Ewk			
Source	Inclusive Fiducial SR	VBS Fiducial SR	Comment
MC stat. uncert.	1%	2%	
Generator	5%	3%	POWHEG-BOX vs. VBFNLO
Parton shower	2%	4%	PYTHIA8 vs. HERWIG++
Scale	2%	2%	scale variations
PDF	2%	3%	CT10 eigenvector variations
Total	6%	6%	

Table 4.6: Summary of systematic uncertainties on $W^{\pm}W^{\pm}jj$-Ewk production cross sections in the two fiducial regions.

The $W^{\pm}W^{\pm}jj$-Ewk fiducial cross sections are then:

$$\sigma^{W^{\pm}W^{\pm}jj-\text{Ewk.}}_{\text{Incl. Fid. SR}} = 1.003 \pm 0.060 \text{ fb}, \tag{4.3}$$

$$\sigma^{W^{\pm}W^{\pm}jj-\text{Ewk.}}_{\text{VBS Fid. SR}} = 0.881 \pm 0.053 \text{ fb}, \tag{4.4}$$

where the error includes all systematic uncertainties discussed so far. The fiducial cross section can be extrapolated to the phase space where the SHERPA signal sample is produced and used for normalizing the SHERPA sample. Starting from the Inclusive Fiducial SR and VBS Fiducial SR, the extrapolated cross section is 19.86 fb and 20.77 fb. The difference is due to different $\Delta y(jj)$ shape in POWHEG-BOX and SHERPA. The cross section derived from the Inclusive Fiducial SR is used for the inclusive signal region and all control regions. The cross section derived from the VBS Fiducial SR is used for VBS signal region.

4.5.1.1 $W^{\pm}W^{\pm}jj$-Strong

The production cross sections of $W^{\pm}W^{\pm}jj$-Strong in the two fiducial signal regions are evaluated similarly as for $W^{\pm}W^{\pm}jj$-Ewk. However the NLO calculation is not available in VBFNLO for $W^{\pm}W^{\pm}jj$-Strong and the scale and PDF uncertainties are evaluated using POWHEG-BOX. For the scale uncertainties, only the variations of both scale choices varied in the same direction by a factor of 0.5 or 2 are considered, due to computing time constraint. The PDF uncertainties are evaluated using a reweighting technique instead of carrying out the calculation for each of the eigenvectors. Though VBFNLO is not available for the calculation, a 5% uncertainty is assigned for the generator dependence, as observed in the Inclusive Fiducial SR for $W^{\pm}W^{\pm}jj$-Ewk. The summary of all systematic uncertainties are shown in Table 4.7.

$W^{\pm}W^{\pm}jj$-Strong			
Source	Inclusive Fiducial SR	VBS Fiducial SR	Comment
MC stat. uncert.	4%	8%	
Generator	5%	5%	Ewk. POWHEG-BOX vs. VBFNLO
Parton shower	3%	7%	PYTHIA8 vs. HERWIG++
Scale	12%	13%	scale variations
PDF	2%	2%	CT10 eigenvector variations
Total	14%	18%	

Table 4.7: Summary of systematic uncertainties on $W^{\pm}W^{\pm}jj$-Strong production cross sections in the two fiducial regions.

The $W^{\pm}W^{\pm}jj$-Strong production cross sections in the two fiducial signal regions with the systematic uncertainties are:

$$\sigma^{W^{\pm}W^{\pm}jj-\text{Strong}}_{\text{Incl. Fid. SR}} = 0.352 \pm 0.049 \text{ fb}, \tag{4.5}$$

$$\sigma^{W^{\pm}W^{\pm}jj-\text{Strong}}_{\text{VBS Fid. SR}} = 0.098 \pm 0.018 \text{ fb}, \tag{4.6}$$

The extrapolated cross section in the phase space where the SHERPA sample is produced is 16.65 fb and 13.49 fb, starting from the Inclusive Fiducial SR and VBS Fiducial SR respectively. The cross section derived from the Inclusive Fiducial SR is used for the normalization of the SHERPA sample in the inclusive signal region and control regions. The cross section derived from the VBS Fiducial SR is used for the VBS signal region.

4.5.1.2 Interference Between $W^{\pm}W^{\pm}jj$-Ewk and $W^{\pm}W^{\pm}jj$-Strong

The interference between $W^{\pm}W^{\pm}jj$-Ewk and $W^{\pm}W^{\pm}jj$-Strong production is checked using SHERPA at LO. SHERPA can produce $W^{\pm}W^{\pm}jj$-Ewk and $W^{\pm}W^{\pm}jj$-Strong events separately and also $W^{\pm}W^{\pm}jj$ inclusively with the interference term included. The interference contribution ($W^{\pm}W^{\pm}jj$-Int) is then defined as:

$$\text{Interference} = \text{Inclusive} - \text{Electroweak} - \text{Strong} \tag{4.7}$$

The results are given in Table 4.8. The interference contributes 10.7% of the total production cross section in the Inclusive Fiducial SR and 6.5% in the VBS Fiducial SR. The interference contribution is included in the analysis by scaling up the $W^{\pm}W^{\pm}jj$-Ewk by the corresponding fraction, given the fact that the analysis goal is to observe the electroweak production and if there is no electroweak production there should be no interference. The interference contribution in the VBS Fiducial SR can be parameterized as

$$\sigma^{W^{\pm}W^{\pm}jj-\text{Int}}_{\text{VBS Fid. SR}} = k_{\text{Int}} \cdot \sqrt{\sigma^{W^{\pm}W^{\pm}jj-\text{Ewk}}_{\text{VBS Fid. SR}} \cdot \sigma^{W^{\pm}W^{\pm}jj-\text{Strong}}_{\text{VBS Fid. SR}}} \tag{4.8}$$

and the scale factor k_{Int} is found to be 0.231. The same parameterization will be used for the aQGC studies in Section 4.10.

After including the inteference contribution, the expected signal production

Process	Inclusive Fiducial SR [fb]	VBS Fiducial SR [fb]
$W^{\pm}W^{\pm}jj$-Inclusive	0.662±0.005	0.452±0.004
$W^{\pm}W^{\pm}jj$-Ewk	0.424±0.002	0.370±0.002
$W^{\pm}W^{\pm}jj$-Strong	0.168±0.002	0.053±0.001
Interference	0.071±0.006	0.029±0.005

Table 4.8: Inclusive, electroweak and strong production of $W^{\pm}W^{\pm}jj$. The interference term is calculated as the difference between the inclusive production and the sum of electroweak and strong pdocutions. Only the $e^{+}\mu^{+}$ final state is included in this table.

cross section in the Inclusive Fiducial Signal Region is then

$$\sigma^{W^{\pm}W^{\pm}jj-\text{Ewk+Strong+Int}}_{\text{Incl. Fid. SR}} = 1.52 \pm 0.12 \text{ fb} \tag{4.9}$$

and the signal production cross section in the VBS Fiducial Signal Region is

$$\sigma^{W^{\pm}W^{\pm}jj-\text{Ewk+Int}}_{\text{Incl. Fid. SR}} = 0.949 \pm 0.071 \text{ fb} \tag{4.10}$$

4.6 Background Estimation

After the event selections as described in Section 4.4, background events come from SM processes which can be put into three categories.

The first category of processes produce at least one pair of prompt same-electric-charge leptons from W or Z boson decay and mainly include:

- $W^{\pm}Z/\gamma* \rightarrow \ell^{\pm}\nu\ell'^{+}\ell'^{-}$,
- $ZZ \rightarrow \ell^{+}\ell^{-}\ell'^{+}\ell'^{-}$,
- $t\bar{t}W^{\pm} \rightarrow W^{+}bW^{-}\bar{b}W^{\pm}$ and $t\bar{t}Z \rightarrow W^{+}bW^{-}\bar{b}Z$ with at least two bosons decaying leptonically and giving a same-electric-charge pair.

Only the two same-electric-charge leptons are selected and the rest of the leptons are not reconstructed or do not pass either the nominal or the veto lepton definitions. These backgrounds will be refered to as *prompt backgrounds* and are estimated using MC samples. The $WZ/\gamma*$ process will be labeled simply as WZ in some of the plots and tables presented.

The second category of processes involve photon conversions and mainly include:

- $W^{\pm}\gamma \rightarrow \ell^{\pm}\nu\gamma$ with the photon converted into a pair of electrons,

- $Z \rightarrow e^+e^-$ with one of the electron's charge mis-identified through photon conversion,
- $t\bar{t} \rightarrow \ell^+\nu b\ell^-\nu\bar{b}$ with at least one electron in the final state and the electron's charge mis-identified through photon conversion.

The $W^{\pm}\gamma$ production is estimated using MC simulation. The other photon conversion backgrounds, which have a pair of opposite-electric-charge leptons in the original event, are estimated directly from data and will be refered to as charge mis-identification (mis-ID) backgrounds. In some of the plots charge mis-ID background is also labeled as *OS prompt leptons*.

The third category of processes produce only one prompt lepton from W boson decay and have a non-prompt lepton from mis-reconstruction or hadron decay. They include:

- $W^{\pm} + \text{jets} \rightarrow \ell^{\pm}\nu + \text{jets}$,
- $t\bar{t} \rightarrow \ell^+\nu bjj\bar{b}$,
- $W^{\pm}V \rightarrow \ell^{\pm}\nu jj$.

These *non-prompt backgrounds* are estimated from data. In some of the plots non-prompt background is labeled as *Other non-prompt* given the charge mis-ID background is also non-prompt in some sense.

In all the above background processes spelled out, extra jets can be present in the event apart from the specified boson and top quark production. Details about estimation of the backgrounds are given in the following sections.

4.6.1 Charge Mis-ID Backgrounds

The electron charge mis-ID happens mostly through a photon conversion process as shown in Figure 4.6. It also happens that the electron track is mis-measured or the cluster-track association is wrong leading to a wrong charge measurement but this only accounts for 10-20% of all charge mis-ID cases. It has been found that for muons the charge mis-ID is completely negligible. The probability for an electron to have its charge mis-identified can be measured from data and is called charge mis-ID rate. With the charge mis-ID rate, one can then extrapolate from an opposite-electric-charge control sample to the same-electric-charge signal regions to estimate the backgrounds due to charge mis-ID.

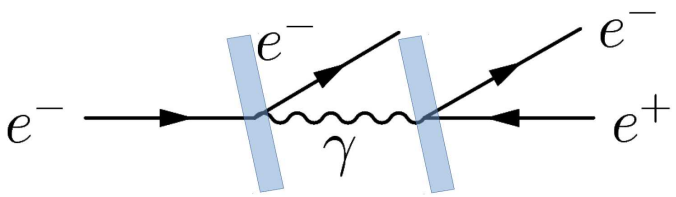

Figure 4.6: A hard photon is radiated off an electron and later converts to a pair of electrons. The light blue box represents the material in the inner detector which is needed for the radiation and photon conversion to happen. Only the final positron is matched to the original electron track and eventually reconstructed as a positron. The other two electrons are not reconstructed due to low momentum.

4.6.1.1 Charge Mis-ID Rate Measurement

The charge mis-ID rate in this analysis is measured in $Z \to ee$ data events. The $Z \to ee$ events are selected by requiring two nominal definition electrons, which have an invariant mass 70 GeV $< m_{ee} <$ 100 GeV. The two electrons are then checked to see whether they have opposite sign (OS) or same sign (SS) of electric charge. Both the OS and SS di-electron samples are dominated by $Z \to ee$ production. In the SS sample, since the two electrons are selected with the same quality requirement, either one could have had its charge mis-identified and the probability to find such an event should be $\epsilon_1 + \epsilon_2$, where $\epsilon_{1,2}$ is the probability to have the charge mis-identified for one of the two electrons respectively. The charge mis-ID rate can be parameterized as a function of the electron p_{T} and η. Given $N^{i,j}$ total events (OS+SS) with the two electrons respectively in bin i and j of the parameterization, the number of SS events with two electrons respectively in bin i and j is expected to be:

$$N^{i,j}_{\mathrm{SS,expected}} = N^{i,j} \cdot (\epsilon_i + \epsilon_j) \tag{4.11}$$

Assuming Poisson statistics, the likelihood function for bin (i,j) is then:

$$L(\epsilon | N^{i,j}, N^{i,j}_{\mathrm{SS}}) = \frac{\left[N^{i,j}(\epsilon_i + \epsilon_j)\right]^{N^{i,j}_{\mathrm{SS}}}}{N^{i,j}_{\mathrm{SS}}!} e^{-N^{i,j}(\epsilon_i + \epsilon_j)} \tag{4.12}$$

The combined log-likelihood function for all bins is:

$$\ln L(\epsilon|N, N_{\rm SS}) = \ln \prod_{i,j} L(\epsilon|N^{i,j}, N_{\rm SS}^{i,j}) \tag{4.13}$$

$$= \sum_{i,j} \ln L(\epsilon|N^{i,j}, N_{\rm SS}^{i,j}) \tag{4.14}$$

$$= \sum_{i,j} \left[N_{\rm SS}^{i,j} \cdot \ln \left(N^{i,j}(\epsilon_i + \epsilon_j) \right) - N^{i,j}(\epsilon_i + \epsilon_j) \right] \tag{4.15}$$

Here $N^{i,j}$ is the total number of events with two electrons (OS or SS) respectively in bin i and j and $N_{\rm SS}^{i,j}$ is the number of SS events in the same bin. In the last step of the above equation we have dropped the term $\sum_{i,j} \ln(N_{\rm SS}^{i,j}!)$, which does not depend on the charge mis-ID rate ϵ.

The charge mis-ID rate ϵ can be derived by maximizing the combined log-likelihood function. It is shown in Figure 4.7 as a function of η and as a function of η and $p_{\rm T}$. For high-$p_{\rm T}$ electrons, which radiate more photons, or electrons which traverse the high-η detector region, which means more detector material to go through, the charge mis-ID rate is higher. In the high-η region, there is discrepancy between the rate measured from data and that predicted by MC. This is due to the imperfect modeling of the material budget in the detector simulation in that region, which is the motivation for estimating this background from data.

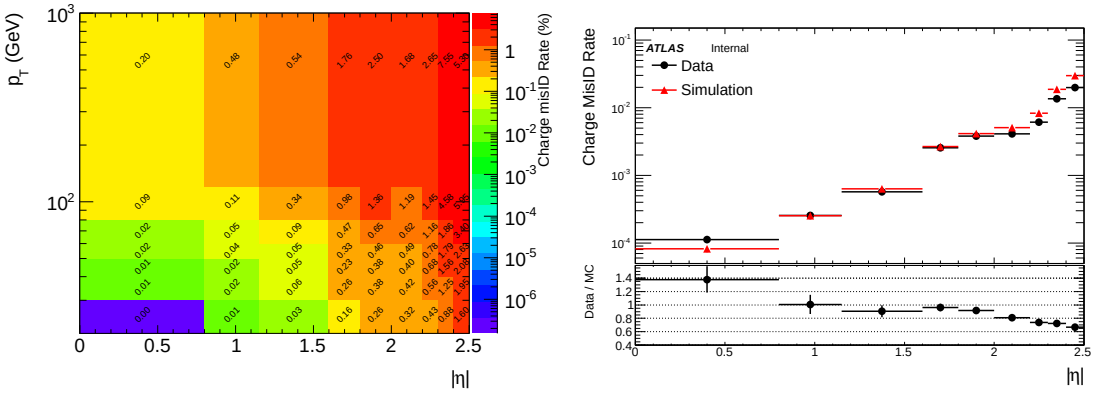

Figure 4.7: The electron charge mis-ID rate as a function of $p_{\rm T}$ and η (left) and as a function of η (right).

A MC closure test is performed on the likelihood method, by comparing the charge mis-ID rate measured in the MC sample using the likelihood method and

the charge mis-ID rate determined using generator level information. The reconstruction level electrons can be matched to generator level truth electrons to see whether the charge has been mis-identified. In Figure 4.8, the charge mis-ID rate is shown in different η ranges as a function of the electron p_{T}. The relative difference is used as a systematic uncertainty on the charge mis-ID rate. In the high-η region, which is more populated with charge mis-ID events, the two methods are found to be in good agreement. In the low-η region, the discrepancy is slightly larger but the charge mis-ID rate is very low in this region and the uncertainty has a small effect on the overall estimation.

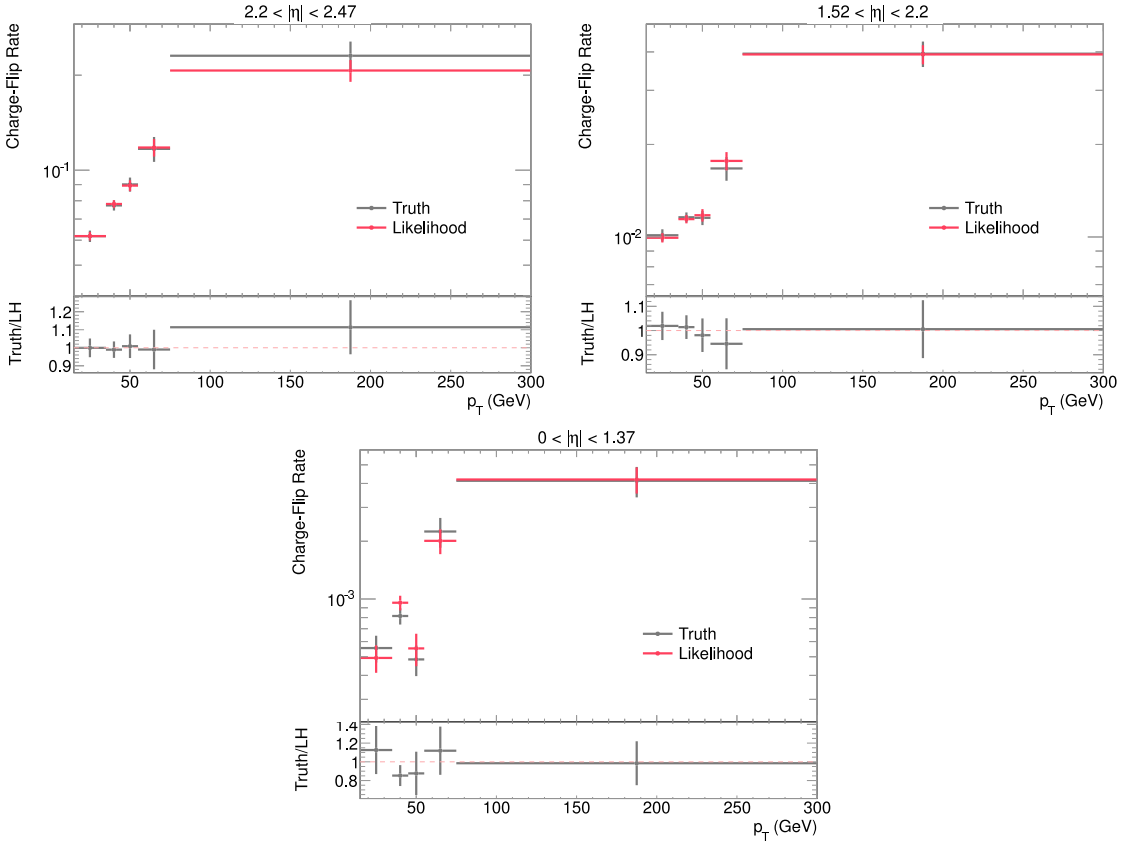

Figure 4.8: The charge mis-ID rate in the MC sample measured using the likelihood method and derived using truth level information. The uncertainties are statistical only and should be considered fully correlated since the same MC sample is used for deriving both.

4.6.1.2 Energy Loss Correction

In the photon conversion process as shown in Figure 4.6, part of the original electron's energy is lost to the soft electrons which are not reconstructed. Since an opposite-electric-charge control sample will be scaled for estimating the charge mis-ID backgrounds and the electrons in this control sample do not undergo such a process, the energy loss of the electron needs to be applied. This energy loss is studied using MC $Z \rightarrow ee$ simulation and a correction scheme is derived. In Figure 4.9, the difference between the truth electron energy and the reconstructed electron energy is compared for electrons with the correct charge measurement, electrons with charge mis-identified through photon conversion (trident) and electrons with charge mis-identified due to track mis-measurement.

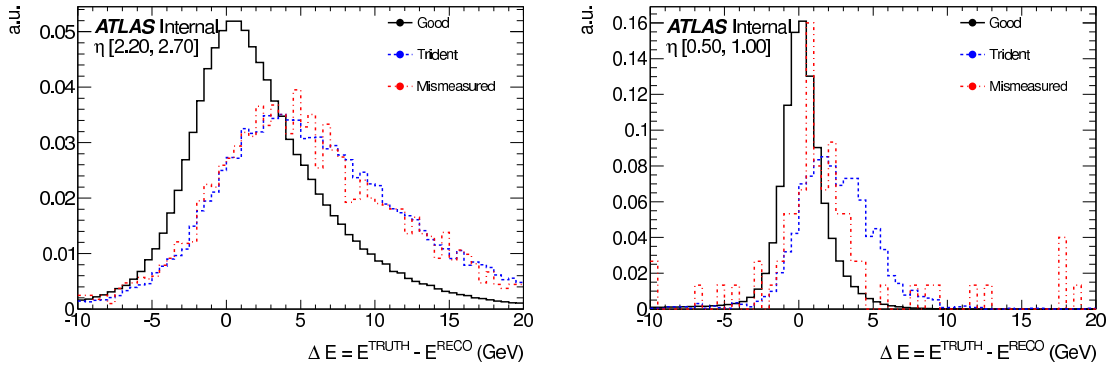

Figure 4.9: The difference between the truth electron energy and the reconstructed electron energy for electrons with correct charge measurement (Good), electrons with wrong charge measurement through photon conversion (Trident) and electrons with wrong charge measurement not through photon conversion (Mismeasured).

The energy loss correction is parameterized in the form of

$$E_{\text{corrected}} = E_{\text{original}} - E_{\text{bias}} + \text{Gauss}(0, E_{\Delta\text{res}}). \tag{4.16}$$

Here E_{bias} is the difference between the mean $\Delta E = E_{\text{truth}} - E_{\text{reconstructed}}$ of *Good* electrons and that of *Trident+Mismeasured* electrons combined. E_{bias} characterizes the linear shift of the electron energy. The Gaussian term with resolution $E_{\Delta\text{res}}$ accounts for the resolution degradation of the electron energy. $E_{\Delta\text{res}}$ is calculated by fitting respectively the ΔE distribution of *Good* electrons and that of *Tri-*

dent+Mismeasured electrons using a Gaussian function and take the quadrature difference of the Gaussian widths. Both E_{bias} and $E_{\Delta\text{res}}$ are measured as a function of the electron η and p_{T}. The dependence on the electron p_{T} is found to be weak and eventually both E_{bias} and $E_{\Delta\text{res}}$ are uased only as a function of η after integrating over the whole p_{T} range, shown in Figure 4.10.

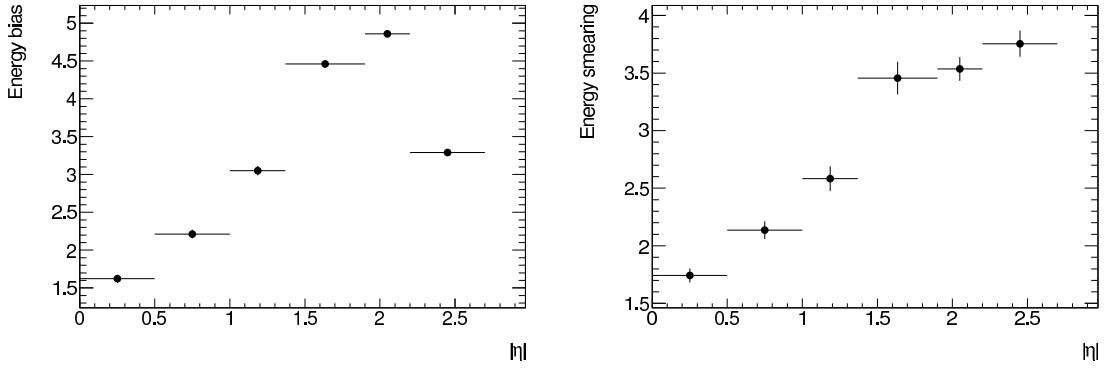

Figure 4.10: Electron energy loss correction parameters: linear shift term (left) and resolution smearing term (right). The unit of the y-axis is GeV.

The energy loss correction is also tested on simulated $Z \to ee$ events. In Figure 4.11, the m_{ee} distribution is compared for three different samples: opposite-electric-charge events, same-electric-charge events, and opposite-electric-charge events after applying the energy loss correction. It can be seen from the figure that the energy loss correction well describes the shift and widening of the di-electron invariant mass distribution in the same-electric-charge sample.

4.6.1.3 Charge Mis-ID Background Estimation

With the charge mis-ID rate and the electron energy loss correction, the charge mis-ID background is estimated in the following procedure:

1. For each signal region or control region, a corresponding opposite-sign control sample is selected with the same set of selection cuts except asking for a pair of opposite-sign leptons. The kinematic cuts on electrons (p_{T}, $m_{\ell\ell}$, etc.) are loosened to make room for the electron energy loss correction.
2. For each electron selected, apply the energy loss correction and check the kinematic cuts again. If all selection cuts are passed, this event is added to the background estimate with the charge mis-ID rate as the new event weight.

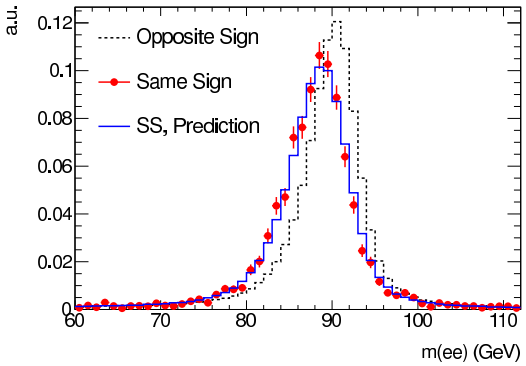

Figure 4.11: Di-electron invariant mass distribution for opposite-sign events (dashed curve), same-sign events (red) and opposite-sign events after applying the energy loss correction (blue).

The corrected electron energy is used for all relevant calculation instead of the original value.

3. For events with two electrons, both electrons should be used in turn as a candidate for the one with charge mis-identified. When one is taken as the candidate, the other one is assumed to have the charge correctly measured and the energy is kept unchanged. Thus each opposite-sign event adds two background estimate events, each weighted with the charge mis-ID rate.

One subtlety arises considering the statistical uncertainties associated with the ee events. Since each ee event in the opposite-sign control sample corresponds to two background estimate events, the statistical uncertainties tied to these two events should be fully correlated. For technical simplicity, throughout the analysis the statistical uncertainties are still taken as un-correlated and are only increased in the final yield by 9-17% depending on the signal region to account for the correlation.

4.6.1.4 Systematic Uncertainties and Control Regions

The following systematic uncertainties on the charge mis-ID background estimation are considered:

- Statistical uncertainty on the charge mis-ID rate: The charge mis-ID rate is applied as a function of the electron p_{T} and η. The statistical uncertainty in each bin is taken as un-correlated and propagated to the background estimation. The net effect on the event yield depends on the control region or signal region under consideration, varying between 1.7% to 4.5%. A univer-

sal 4.5% is eventually assigned to charge mis-ID background in all regions considered.

- Likelihood method: In the closure test as shown in Figure 4.8, a small deviation is observed for the rate measured using the likelihood method compared to the rate derived using truth level information. The relative difference on the rate is taken as a systematic uncertainty and is propagated fully correlated in different p_{T} and η bins. The final effect on the estimation varies from 0.7% to 2.6% for different control and signal regions. An overall 2.6% uncertainty is eventually quoted for charge mis-ID background in all regions.
- Background subtraction in $Z \rightarrow ee$ data sample: The charge mis-ID rate is measured in $Z \rightarrow ee$ data sample. After the selection of two electrons, the sample is dominated by $Z \rightarrow ee$ events. Small contributions from W+jets and diboson (mainly WZ) exist in the same-electric-charge sample. These background events are estimated using di-electron invariant mass sideband extrapolation and the effects are estimated by subtracting the backgrounds from the data sample. The uncertainty is found to be 0.2% on charge mis-ID background for the signal regions and 2% in control regions.
- Double counting between charge mis-ID and prompt backgrounds: The prompt backgrounds (mainly WZ) are estimated using MC simulation, as will be discussed in Section 4.6.3. In the MC simulaion, the selected same-sign events in the signal region can also come from charge mis-ID given that processes like WZ can also produce opposite-sign lepton pairs when the third lepton is not reconstructed. However this part is already directly estimated in the charge mis-ID estimation using data. The double counting is always less than 3% and 5% in the ee and $e\mu$ channel respectively. Half of the double counted contribution is taken as the systematic uncertainty.
- Energy loss correction: The electron energy loss correction is derived from MC simulation. After applying the correction to opposite-sign ee data events and comparing to the same-sign di-electron data sample, it is found that the correction does not fully reproduce the energy loss and resolution degradation in data, as shown in Figure 4.12. The energy shift term E_{bias} and the resolution smearing term $E_{\Delta\mathrm{res}}$ needs to be increased by 35% and 25% respectively. These extra corrections are taken as the systematic uncertainties. In addition, the difference observed in deriving the corrections using $Z \rightarrow ee$ MC and $t\bar{t}$ MC is quoted as systematic uncertainty, which is 15%.

- MC *self test*: The whole charge mis-ID estimation procedure is practiced using only MC samples, for $Z \to ee$ and $t\bar{t}$ sample respectively. The estimated same-sign event yield using opposite-sign sample is then compared to the direct same-sign yield from MC. For $Z \to ee$ channel, a 6% difference is observed at most in various control and signal regions. For $t\bar{t}$ sample, an underestimation from the charge mis-ID prediction is observed compared to direct MC prediction. The contribution from $t\bar{t}$ events to the total charge mis-ID background takes up 30% for ee channel and 80% for $e\mu$ channel. The expected $t\bar{t}$ component is assigned 20% uncertainty in control regions and 40% in signal regions.

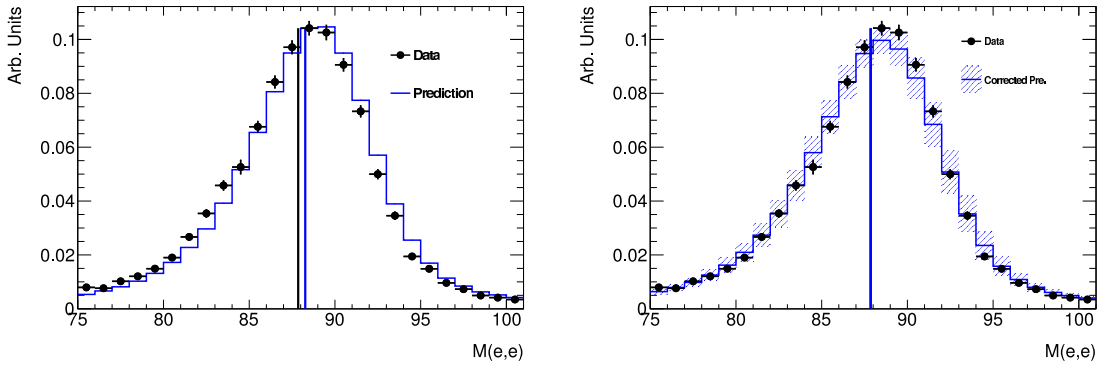

Figure 4.12: The m_{ee} distribution of selected same-sign ee data sample and charge mis-ID prediction using opposite-sign sample. In the left plot, energy loss correction derived using MC $Z \to ee$ sample is applied to the opposite-sign sample for prediction. In the right plot, the energy shift term E_{bias} and smearing term $E_{\Delta\text{res}}$ is increased by 35% and 25% respectively to bring the prediction in better agreement with data.

4.6.1.5 Charge mis-ID Background Control Regions and Estimation in Signal Regions

To further check the charge mis-ID background estimation method using data, a few control regions (CR) which are dominated with charge mis-ID background events are defined:

- Same-Sign Inclusive CR: All selection cuts on leptons and $E_{\text{T}}^{\text{miss}}$ as for signal regions. No cuts on jets.
- Low N_{jet} Charge Mis-ID CR: Same as Same-Sign Inclusive CR but without

the $E_{\mathrm{T}}^{\mathrm{miss}}$ cut and with an extra requirement that at most one jet exists in the event.

- Same-Sign Z CR: For ee channel only, requires two same-sign electrons with invariant mass within 10 GeV around Z mass.
- VBF-Like Same-sign Z CR: Same as Same-Sign Z CR, with an extra requirement that there exists at least two jets and the invariant mass of the two leading-p_{T} jets is greater than 150 GeV.

The observed and expected numbers of events in these control regions are shown in Table 4.11. In all these control regions considered, a good agreement between the observed number of events and the expectation from the background estimation is seen. The m_{ee} distribution in the Low N_{jet} Charge Mis-ID CR is shown in Figure 4.13. The di-electron invariant mass peak is well reproduced by the charge mis-ID estimation using opposite-sign data sample. This indicates both the charge mis-ID rate and the energy loss correction are working as expected. Also shown in Figure 4.13 are the lepton η distributions which outline the material dependence for the charge mis-ID backgrounds. The number of jets distribution in the Same-Sign Inclusive CR indicates the jet activities are well predicted by the estimation.

Control Region Name	Charge Mis-ID	Other Backgrounds	Observed	Expected/Observed
SS Z	11419±12 (stat.)	108±16(stat.⊕syst.)	11820	0.98±0.01
VBF-Like SS Z	313.4±2.4	12.1±1.8	348	0.94±0.05
SS Inclusive	1021.7±3.7	261±41	1318	0.97±0.04
Low N_{jet} Charge Mis-ID	1924.5±5.0	301±56	2370	0.94±0.03

Table 4.9: Expected and observed numbers of events in different control regions. Only statistical uncertainties for the charge mis-ID estimation are shown in the second column. The combined statistical and systematic uncertainties are shown for other backgrounds in the third column. The Expected/Observed ratio in the last column has included all systematic uncertainties of charge mis-ID estimation as described in the previous section.

The estimated charge mis-ID background yields in the two signal regions are given in Table 4.10.

4.6.2 Non-prompt Backgrounds

Non-prompt backgrounds have at least one of the two selected leptons coming from hadron decay or a jet mis-reconstructed as a lepton. The major source of non-prompt backgrounds are SM processes which produce one prompt lepton plus one

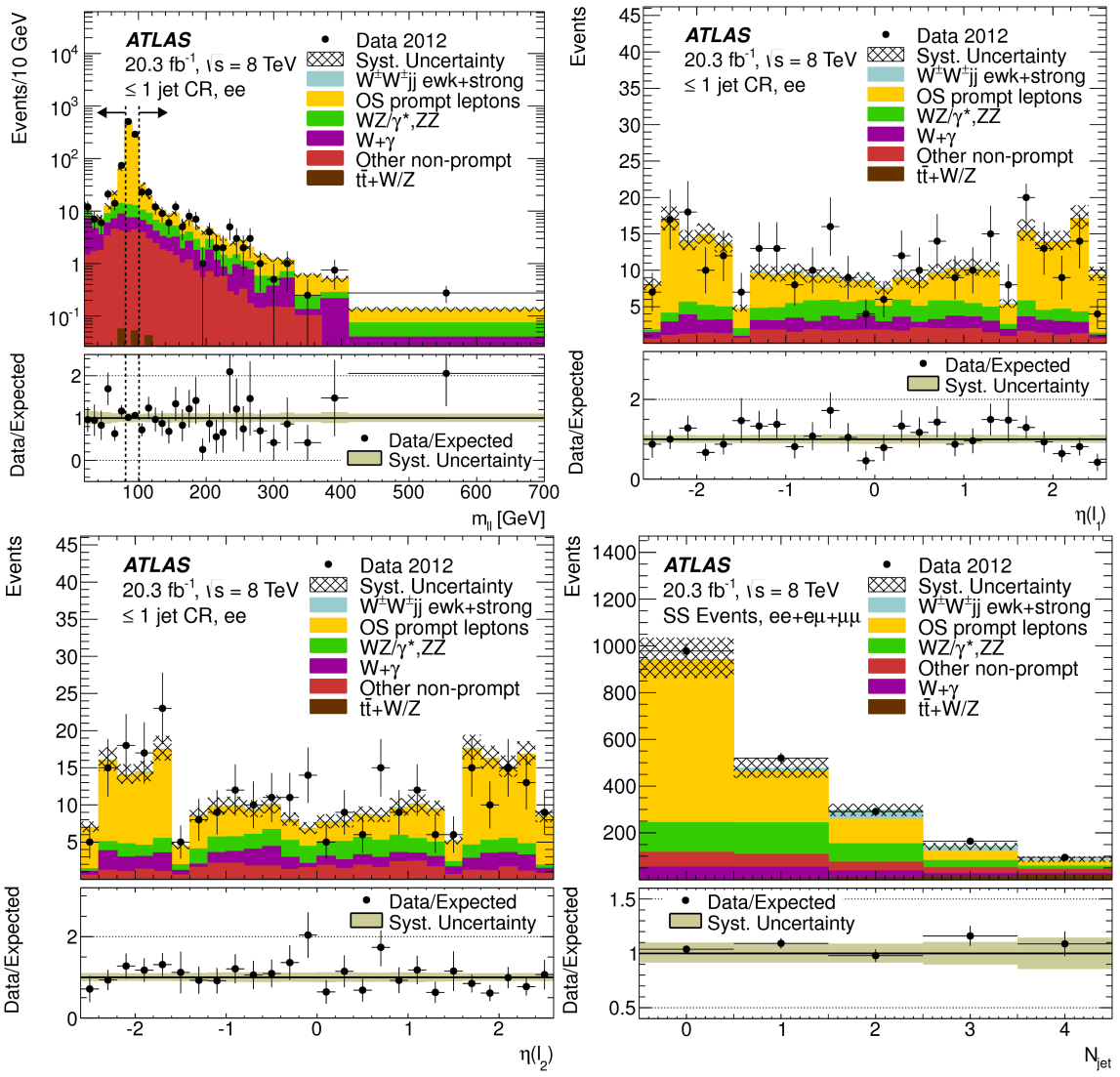

Figure 4.13: The di-electron invariant mass (m_{ee}) distribution (top left), leading-p_{T} lepton η distribution (top right), subleading-p_{T} lepton η distribution (bottom left) in the Low N_{jet} Charge Mis-ID CR and the number of jets (N_{jet}) distribution in the Same-Sign Inclusive CR. The process shown in yellow is the charge mis-ID background estimated using the opposite-sign control sample.

Channel	Inclusive signal region	VBS signal region
ee	2.07±0.21(stat.)±0.31(syst.)	1.39±0.16(stat.)±0.22(syst.)
$e\mu$	0.77±0.09(stat.)±0.25(syst.)	0.64±0.09(stat.)±0.22(syst.)

Table 4.10: Estimated charge mis-ID background yield in the two signal regions. Statistical and systematic uncertainties are also given.

non-prompt lepton. The cases where both leptons are non-prompt are very rare and only contribute no more than 3.5% to the total non-prompt backgrounds in all control and signal regions. The probability for a jet to produce a nominal definition lepton is not easy to measure, unlike the charge mis-ID rate which can be easily meaured using $Z \to ee$ data events. Instead, the ratio of the probability for a jet to produce a nominal lepton and a loose lepton (Section 4.4) can be measured in a jet-enriched data sample. The loose leptons are dominated with non-prompt leptons from jets and can provide a good control sample for non-prompt backgrounds. In the rest of this section, the nominal lepton is refered to as *tight lepton*. The ratio is refered to as *fake factor* and is defined as:

$$f_{\text{lepton}} = \frac{N_{\text{non-prompt tight lepton}}}{N_{\text{non-prompt loose lepton}}} \tag{4.17}$$

Given the fake factor, the non-prompt background estimation is calculated by scaling a *tight+loose* data sample, which is selected in the same way as for any control or signal region but instead requires one of the two leptons to be loose.

$$N_{\text{non-prompt bkg.}} = f_{\text{lepton}} \times N_{\text{tight+loose}} \tag{4.18}$$

The tight+loose sample is dominated by W+jets and $t\bar{t}$ events. Prompt background and charge mis-ID background in the tight+loose sample are estimated using MC simulation and subtracted from data.

4.6.2.1 Fake Factor Measurement Using Di-jet Sample

Di-jet data sample provides a relatively pure jet collection and has large sample size, making it an ideal choice for measring the jet fake factors. To measure the fake factors in di-jet sample and apply the fake factors to tight+loose sample, one has to assume that the jets which are producing the non-prompt leptons in the two samples have similar fake factors. In the rest of this section, the jets producing non-prompt leptons will be refered to as *underlying jets*. It is found that the different p_{T} spectra of underlying jets in di-jet and tight+loose sample will bring some biase to the non-prompt background estimation. This is corrected by introducing a jet p_{T} reweighting to the di-jet sample before measuring the fake factors. More details will be discussed later in this section.

In the di-jet sample selection, jets are defined with $p_{\text{T}} > 25$ GeV and $|\eta| < 4.5$.

Jets overlapping with any tight or loose lepton are removed. Events with jets overlapping with tight muons are removed, to be consistent with the signal region selections. After the jet/lepton overlap removal, one and only one jet is allowed in the event and taken as the tagging jet. The other jet is supposed to have produced the non-prompt lepton and thus should have been removed. After removing electrons overlapping with tight muons, one and only one lepton is allowed to exist. This lepton can be either tight electron (muon) or a loose electron (muon) as defined in Section 4.4 but with the p_{T} cut lowered to 20 GeV. The tagging jet and the lepton is required to be back-to-back in the azimuthal plane with $\Delta\phi(\ell, j) > 2.8$. To suppress the W+jets contamination, the transverse mass of the lepton plus $E_{\mathrm{T}}^{\mathrm{miss}}$ system $m_{\mathrm{T}}(\ell, E_{\mathrm{T}}^{\mathrm{miss}})$ is required to be smaller than 40 GeV. Residual backgrounds from W+jets and Z+jets events, which produce a jet and a prompt lepton in each event, are estimated using MC simulation and subtracted from the data sample. The lepton is then checked to see whether it is a tight lepton or a loose one to determine the ratio between the two.

As can be seen from the previous description, the di-jet sample is actually selected as jet+lepton sample. The event is selected using single lepton trigger. For jet+electron events, a photon trigger `EF_g20_loose` is required, which only uses information from the EM calorimeter clusters and is expected to have little bias on the electron quality or isolation. For jet+muon events, a single muon trigger `EF_mu24_tight` is required, which has no requirement on the muon isolation. The `EF_mu24_tight` trigger is not equally efficient for tight and loose muons. The efficiencies have been measured in data (Appendix B.1) and a 10% difference is observed. This leads to 10% fewer jet+loose muon events selected compared to jet+tight muon events and results in a 10% upward bias to the muon fake factors. For this reason, the measured muon fake factors from the di-jet sample will be multiplied with a factor of 0.9.

The event topology of tight+loose event and di-jet event (or jet+lepton event) is shown in Figure 4.14. The main variable used for discriminating tight and loose leptons is the lepton isolation. For a non-prompt lepton, the part of the energy of the original underlying jet not carried away by the lepton or neutrinos will be deposited in a cone around the lepton, as illustrated in the figure. Thus non-prompt leptons of the same p_{T} which actually come from underlying jets with different p_{T} will have different amount of energy deposited in the isolation cone. A difference in the underlying jet p_{T} distribution between the tight+loose sample and the

di-jet sample will be propagated to the non-prompt lepton isolation distribution and thus cause different fake factors. A study is carried out comparing di-jet sample and Z+jets sample in Appendix B.2, which suggests a jet p_{T} reweighting can largely reduce this biase.

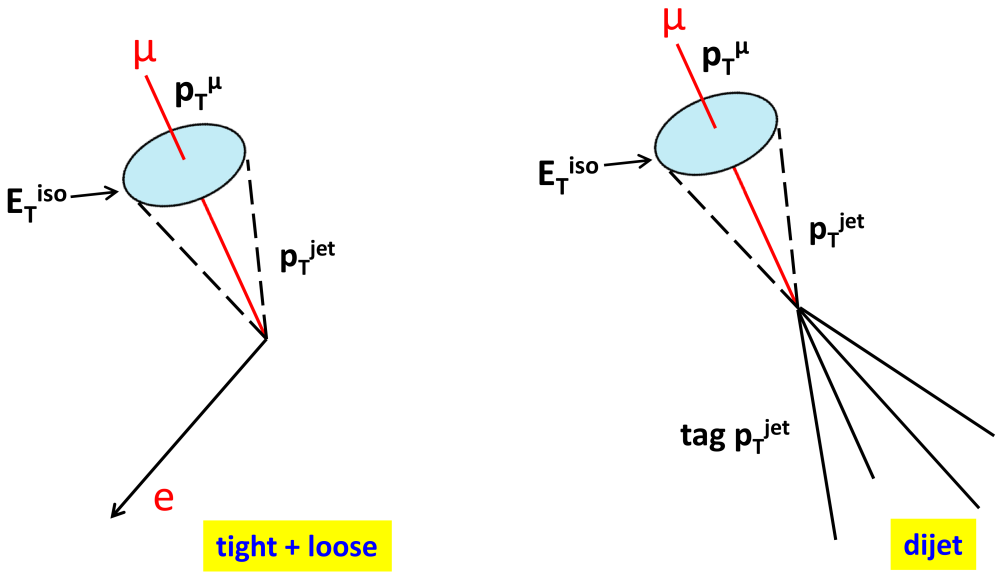

Figure 4.14: The event topology of a tight electron+loose muon event (left) and a jet+loose muon event (right).

To correct the biase introduced by the different underlying jet p_{T} distribution in the tight+loose and di-jet sample, it would be ideal to reweight the underlying jet p_{T} distribution in the di-jet sample to be the same as that in the tight+loose sample. However, the underlying jets are not accessible in either the di-jet sample or the tight+loose sample, given that they have produced the non-prompt lepton plus jets and neutrinos. Instead, in the di-jet sample, the tagging jet p_{T} is used as a representitive of the underlying jet p_{T}, assuming the balance of transverse momenta in the di-jet event. In the tight+loose sample, the non-prompt lepton $p_{\mathrm{T}} + E_{\mathrm{T}}^{\mathrm{cone30}}$ is used together with a mapping function for deriving the underlying jet p_{T} distribution of the tight+loose sample.

The mapping from the non-prompt lepton $p_{\mathrm{T}} + E_{\mathrm{T}}^{\mathrm{cone30}}$ to the underlying jet p_{T} is derived using the di-jet sample, assuming again the balance of transverse momenta. In di-jet sample where one of the two jets is reconstructed as a loose

lepton, the average tagging jet p_{T} versus the loose lepton $p_{\mathrm{T}} + E_{\mathrm{T}}^{\mathrm{cone30}}$ is shown in Figure 4.15. A linear correlation is obvious from the plot, with a larger slope for loose muons than loose electrons. This difference is expected given most of the non-prompt muons come from heavy-flavor hadron decay and it is usually accompanied with neutrinos in the final state, while non-prompt electrons mainly come from jets that deposit a significant part of the energy in the EM calorimeter. The mapping can be parameterized as:

$$p_{\mathrm{T}}(\text{underlying jet}) = \text{p1} \times (p_{\mathrm{T}} + E_{\mathrm{T}}^{\mathrm{cone30}}) + \text{p0} + \text{Gauss}(0,1) \times \text{RMS}, \qquad (4.19)$$

where p0 and p1 are the two linear fitting parameters as shown in Figure 4.15 and the Gauss$(0,1) \times$RMS term is to account for the tagging jet p_{T} distribution width in each bin of the lepton $p_{\mathrm{T}}+E_{\mathrm{T}}^{\mathrm{cone30}}$. The tagging jet p_{T} distribution from di-jet sample and the derived underlying jet p_{T} distribution from tight+loose sample using the mapping are shown in Figure 4.16. In the fake factor measurement, the tagging jet p_{T} distribution in di-jet sample will be reweighted to be the same with the derived underlying jet p_{T} distribution from tight+loose sample.

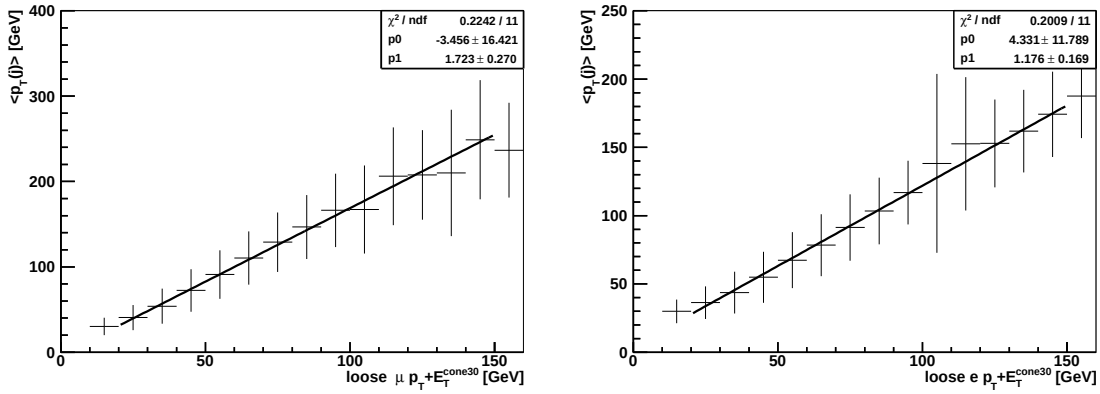

Figure 4.15: Average tagging jet p_{T} versus loose lepton $p_{\mathrm{T}} + E_{\mathrm{T}}^{\mathrm{cone30}}$ for jet+loose muon events (left) and jet+loose electron events (right). The error bar is the RMS of the tagging jet p_{T} in each bin of the loose lepton $p_{\mathrm{T}} + E_{\mathrm{T}}^{\mathrm{cone30}}$.

The loose lepton isolation distribution is shown in Figure 4.17. After reweighting the tagging jet p_{T} distribution in the di-jet sample, the lepton isolation distributions are in better agreement with the tight+loose sample. The distributions from the tight+loose sample are obtained after the $N_{jet} \geq 2$ cut, which already have similar non-prompt background compositions as the final signal regions. Adding

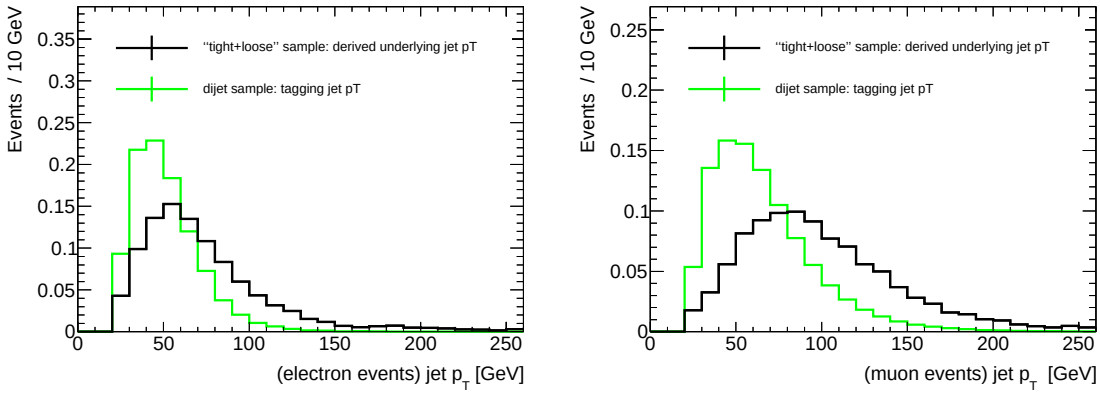

Figure 4.16: The tagging jet p_{T} distribution from the di-jet sample and the derived underlying jet p_{T} distribution from tight+loose sample for electrons (left) and muons (right). The derived underlying jet p_{T} distribution is obtained after the $N_{jet} \geq 2$ cut in the ee and $\mu\mu$ channel.

more cuts to the tight+loose sample increases the statistical uncertainties but does not change the shape of the isolation distributions. Figure 4.15 indicates that on average a 25 GeV non-prompt muon comes from a 40 GeV jet and 25 GeV non-prompt electron comes from a 35 GeV jet. Thus in the di-jet sample, the tagging jet p_{T} is further required to be greater than 40 GeV for muon events and 35 GeV for electron events, to avoid the extreme cases where low-p_{T} jets produce high-p_{T} non-prompt leptons. Fake factors measured using the reweighted di-jet sample is shown in figure 4.18.

The following sources of systematic uncertainties are considered for the fake factor measurement:

- Prompt background subtraction: In the selected di-jet sample, prompt contaminations exist from W+jets and Z+jets events. This prompt contribution is estimated using MC simulation and subtracted from data sample before calculating the fake factors. The MC modeling of the prompt background is checked using a control region as documented in Appendix B.3. A 4% and 12% uncertainty is assigned to the prompt background estimation in electron events and muon events respectively and propaged to the fake factor calculation. The fake factors measured with the prompt MC estimation variation are shown in Figure 4.19. This uncertainty dominates the total systematic uncertainty in the high-p_{T} region where the prompt backgrounds dominate the tight leptons.

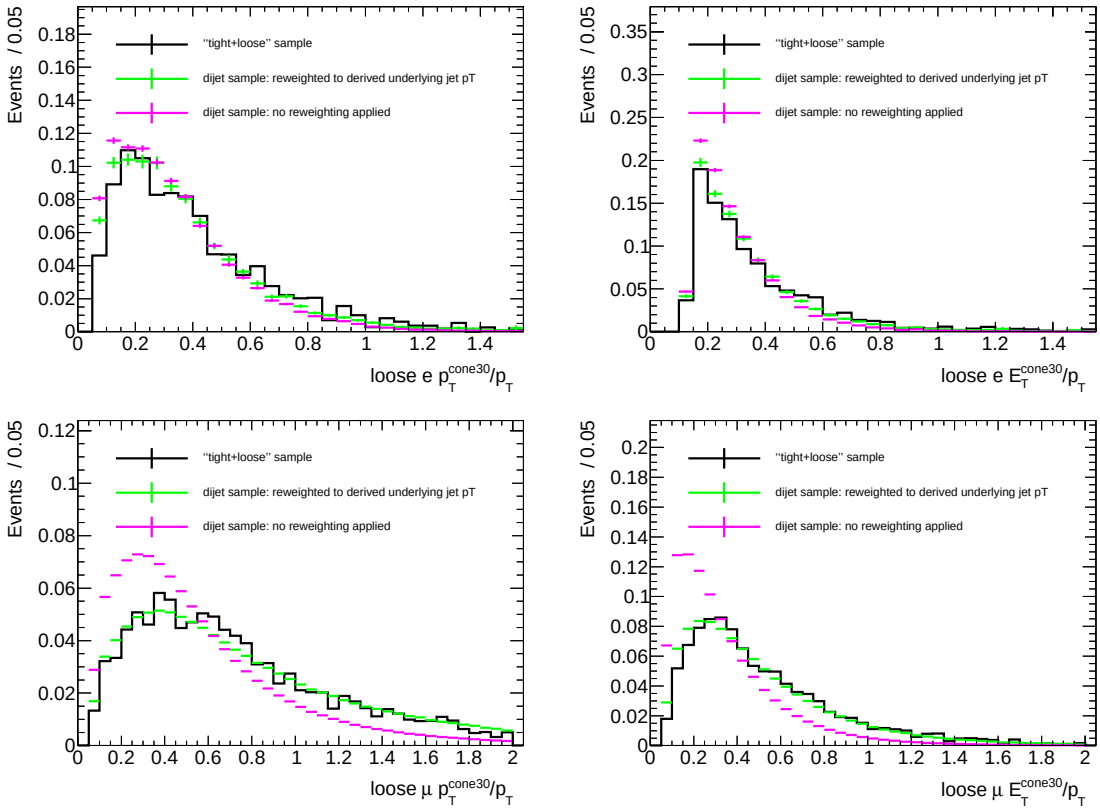

Figure 4.17: The $p_{\mathrm{T}}^{\mathrm{cone30}}/p_{\mathrm{T}}$ and $E_{\mathrm{T}}^{\mathrm{cone30}}/p_{\mathrm{T}}$ distributions for loose electrons (top) and loose muons (bottom). Distributions shown are for the di-jet sample without reweighting, the di-jet sample with tagging jet p_{T} reweighting, and the tight+loose sample. After the reweighting, good agreement is observed between the di-jet sample and the tight+loose sample. The distributions for the tight+loose sample are obtained after the $N_{jet} \geq 2$ cut.

- Tagging jet p_{T} cut: In selecting the di-jet sample, the tagging jet p_{T} is required to be larger than 40 GeV for muon events and 35 GeV for electron events. The cut value is varied by 5 GeV for systematic uncertainties. The fake factors measured with the tagging jet p_{T} cut variation are shown in Figure 4.20. A stronger dependence is seen for muons.
- Residual flavor dependence: The difference between the underlying jet p_{T} distribution in the di-jet sample and that in the tight+loose sample is resolved by the tagging jet p_{T} reweighting. The underlying jet flavor composition, which is different between the di-jet sample and the tight+loose sample, can still affect the fake factors. Such residual flavor dependence is checked by comparing W+jets and $t\bar{t}$ MC samples, documented in Appendix B.4. The

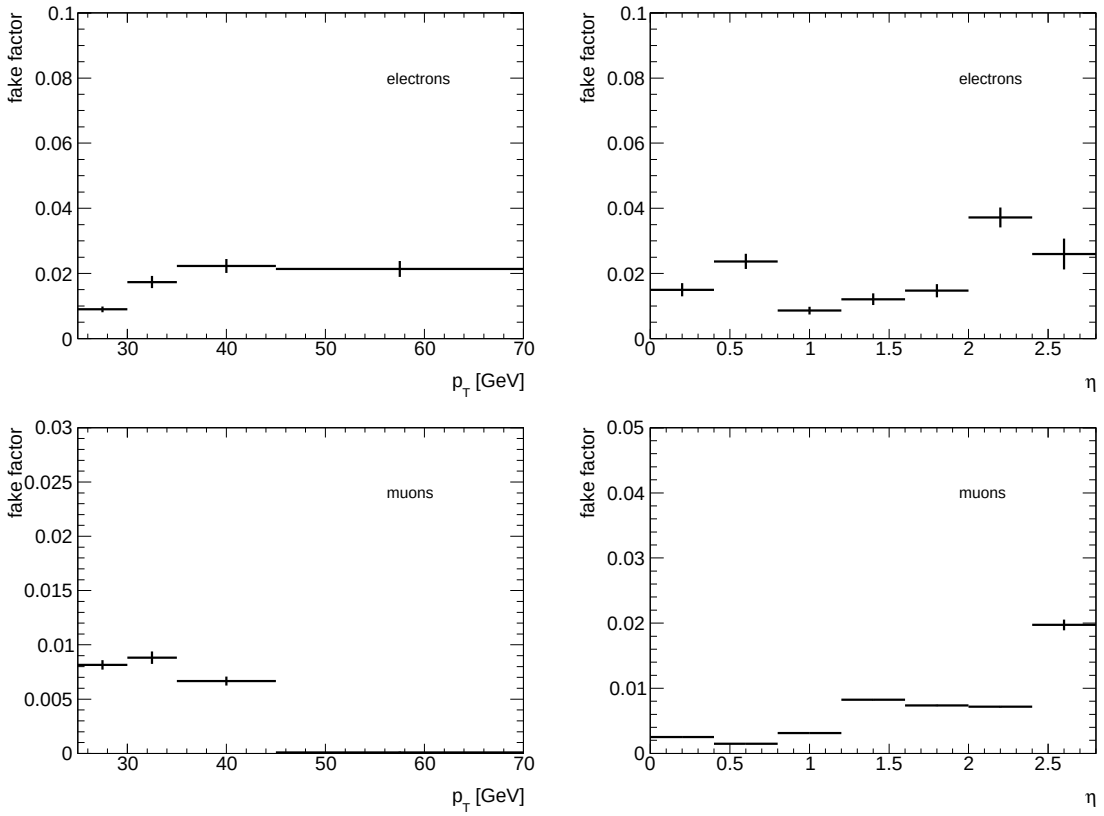

Figure 4.18: Fake factors measured using reweighted di-jet sample for electrons (top) and muons (bottom) as a function of the lepton p_{T} and η. The error bar contains only the statistical uncertainty.

slope of the mapping from non-prompt lepton $p_{\mathrm{T}} + E_{\mathrm{T}}^{\mathrm{cone30}}$ to the underlying jet p_{T} is found to be different between W+jets and $t\bar{t}$ MC samples. This difference can be covered by a 15% variation of the mapping slope measured using di-jet data sample. Thus to account for the systematic uncertainties due to the residual flavor dependence, the fake factors are measured again with the mapping slope varied by 15% and the resulting variations in the fake factors are quoted as the systematic uncertainties. The fake factors are shown in Figure 4.21 with such variations.

- Other selection cut dependence: The $m_{\mathrm{T}}(\ell, E_{\mathrm{T}}^{\mathrm{miss}}) < 40$ GeV cut and the $\Delta\phi(\ell, j) > 2.8$ cut is varied by 5 GeV and 0.1 respectively to check the effects of the cut dependence. These variations are found to be negligible compared to the other sources of sytematic uncertainties.

Fake factors with statistical uncertainties and all uncertainties combined are

shown in Figure 4.22 as a function of p_{T}.

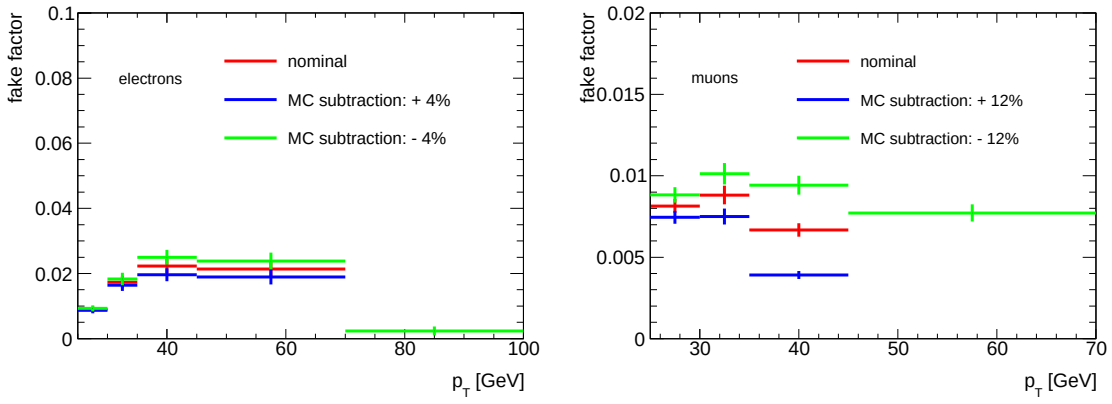

Figure 4.19: Fake factors as a function of the lepton p_{T} for electrons (left) and muons (right) with the prompt background estimation varied by 4% and 12% respectively. The fake factor for muons in the high-p_{T} region is consistent with zero given the uncertainties.

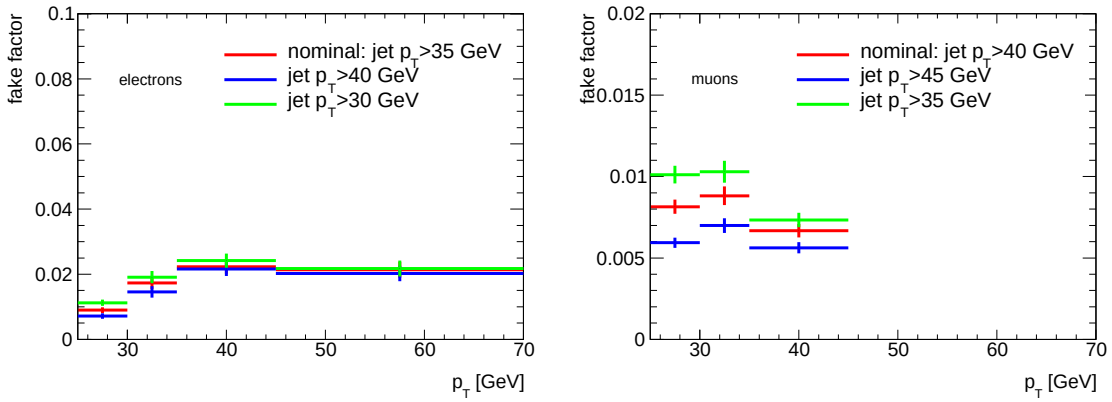

Figure 4.20: Fake factors as a function of the lepton p_{T} for electrons (left) and muons (right) with the tagging jet p_{T} cut value varied by 5 GeV.

4.6.2.2 Trigger Efficiency Correction for tight+loose Sample

The tight+loose sample is selected by requiring the same set of single lepton triggers `EF_e24vhi_medium1`, `EF_e60_medium1`, `EF_mu24i_tight`, or `EF_mu36_tight` as for the nominal analysis. With respect to the tight+tight sample for signal regions, the presence of the loose lepton in tight+loose sample introduces some trig-

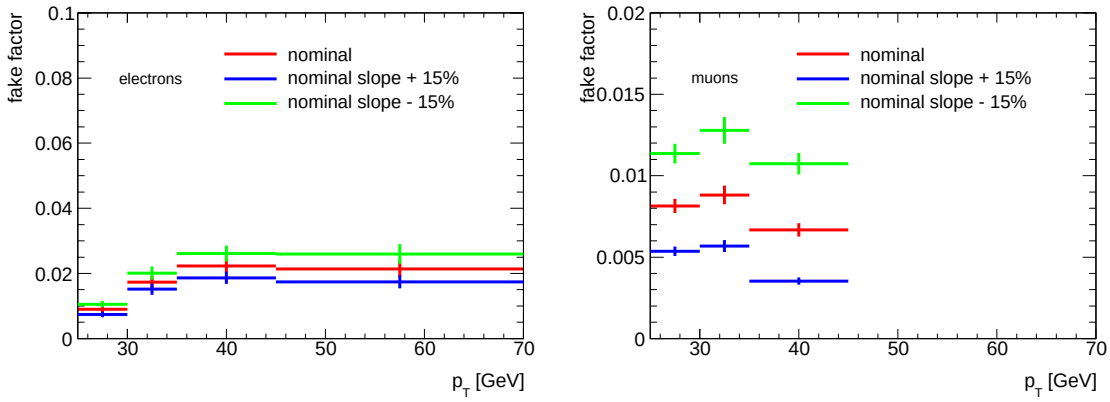

Figure 4.21: Fake factors as a function of the lepton p_{T} for electrons (left) and muons (right) with the mapping slope varied by 15% in deriving the underlying jet p_{T} distribution in the tight+loose sample.

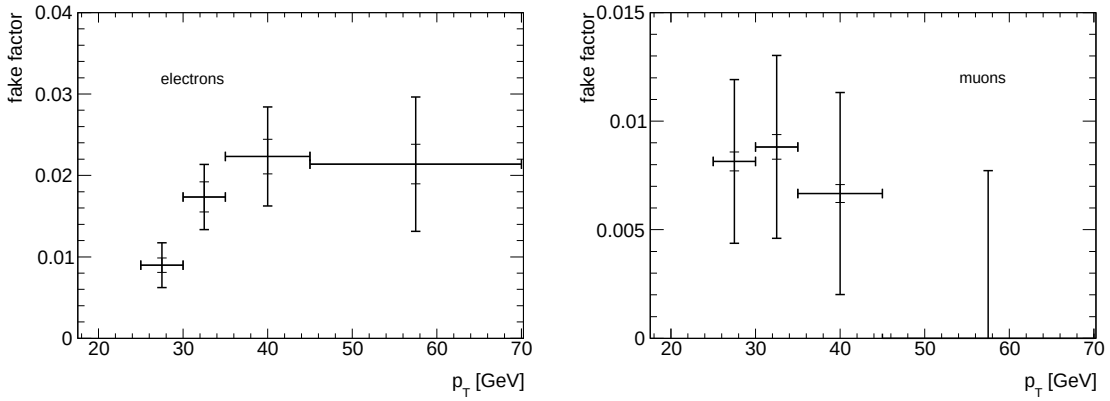

Figure 4.22: Fake factors as a function of the lepton p_{T} for electrons (left) and muons (right) with statistical uncertainties (inner error bar) and statistical and systematic uncertainties combined (outer error bar).

ger inefficiency. Given two leptons, the probability of at least one lepton firing the trigger is

$$\mathrm{P} = 1 - (1 - \epsilon_1)(1 - \epsilon_2), \tag{4.20}$$

where $\epsilon_{1,2}$ is the trigger efficiency for the two leptons respectively. To correct for the trigger inefficiency, the tight+loose sample should be applied with a scale factor

$$\mathrm{K} = \mathrm{P}_{\mathrm{tight+tight}}/\mathrm{P}_{\mathrm{tight+loose}} = \frac{1 - (1 - \epsilon_{1,\mathrm{tight}})(1 - \epsilon_{2,\mathrm{tight}})}{1 - (1 - \epsilon_{1,\mathrm{tight}})(1 - \epsilon_{2,\mathrm{loose}})}, \tag{4.21}$$

where we have labeled the tight lepton in tight+loose sample as 1 and the loose lepton as 2, and $\epsilon_{2,\text{tight}}$ is the trigger efficiency of a tight lepton with the same p_{T} and η as the loose lepton 2.

The trigger efficiencies of tight and loose leptons can be measured from Z+jets and W+jets data samples respectively and the trigger efficiency scale factors K can be calculated as a function of p_{T} and η of the two leptons. The η dependence of the scale factors are found to be flat and the scale factors are shown in Figure 4.23 as a function of the lepton p_{T}.

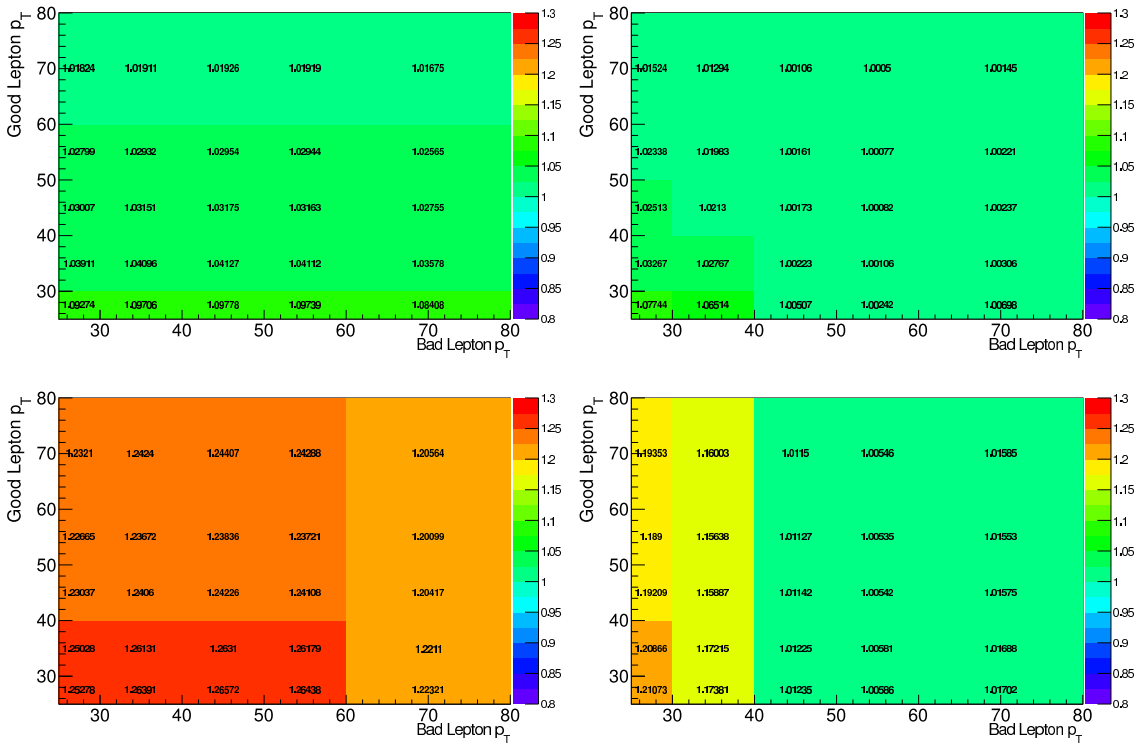

Figure 4.23: The trigger efficiency scale factors for tight e+loose e events (top left), tight e+loose μ events (top right), tight μ+loose e events (bottom left) and tight μ+loose μ events (bottom right). The scale factors are shown as a function of the loose lepton p_{T} (labeled here as *Bad Lepton* p_{T}) and tight lepton p_{T} (labeled as *Good Lepton* p_{T}.

The trigger efficiencies used for calculating the correction scale factors are measured in Z+jets data sample for tight leptons and W+jets data sample for loose leptons. In the tight+loose sample, there is also significant contribution from $t\bar{t}$ events. The trigger efficiencies measured in Z+jets, W+jets and $t\bar{t}$ MC samples are compared for systematic studies, as shown in Figure 4.24. The relative difference is

taken as systematic uncertainty for the trigger efficiencies as measured from data samples and propagated to the calculated scale factors. In measuring the trigger efficiencies, background estimation using MC is subtracted from the data sample and is assigned 100% uncertainty. These systematic uncertainties on the trigger efficiencies, as well as the statistical uncertainties, are all propagated to the trigger efficiency scale factors. The final systematic uncertainty on the scale factor ranges from a few percent to 30% depending on the p_{T} of the two leptons.

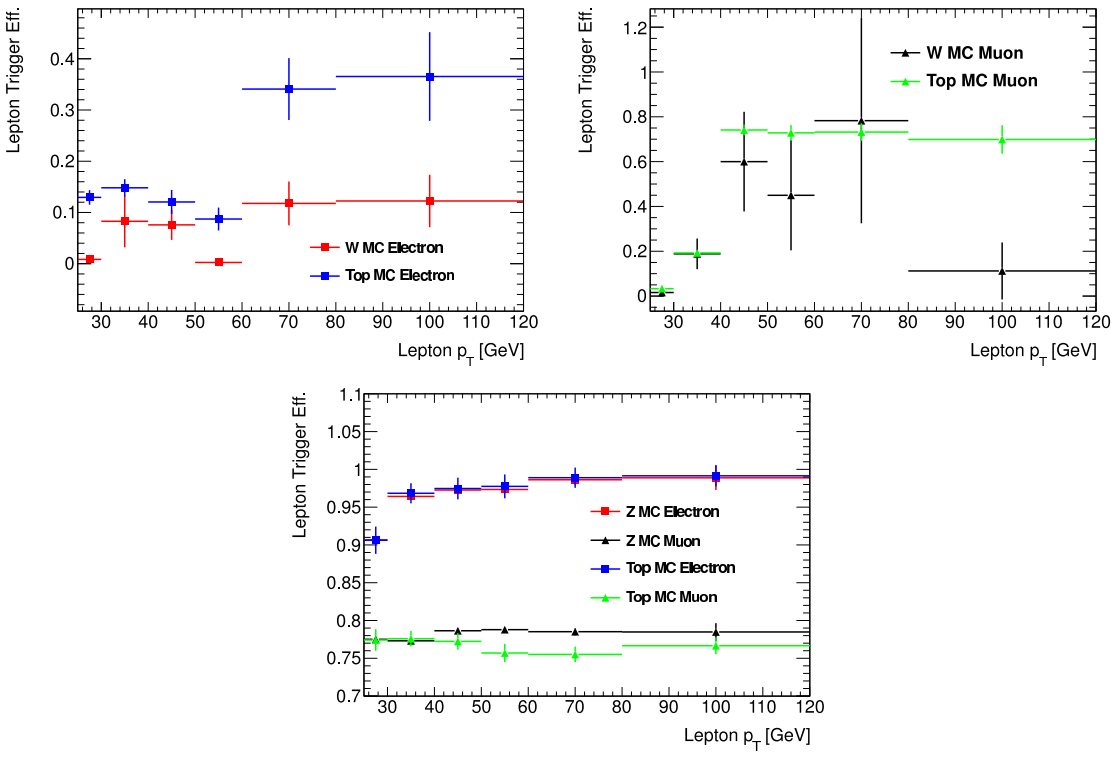

Figure 4.24: Trigger efficiencies measured in W+jets and $t\bar{t}$ MC samples for loose electrons (top left) and loose muons (top right) and trigger efficiencies measured in Z+jets and $t\bar{t}$ MC samples for tight electrons and muons (bottom).

4.6.2.3 Systematic Uncertainties and Non-prompt Background Control Region

The non-prompt background is estimated by scaling the tight+loose sample as in Equation 4.18. Systematic uncertainties for the estimation include:

- systematic uncertainties on the fake factors as described in Section 4.6.2.1,
- systematic uncertainties on the trigger efficiency correction scale factors as described in Section 4.6.2.2,

- a conservative 50% uncertainty on the prompt and charge mis-ID subtraction from the tight+loose sample estimated using MC simulation.

The non-prompt background estimation is checked in dedicated control regions where the non-prompt background has significant presence. Given the very tight lepton isolation in the nominal lepton definition, it is difficult to find such a control region with the non-prompt background dominating. A Top Control Region, which has all cuts up to the selection of two jets and requires further one jet tagged as a b-jet candidate, has 17% to 40% contribution from $t\bar{t}$ events as non-prompt background. The event yields in this region is shown in Table 4.11. The lepton p_{T} distributions are shown in Figure 4.25.

	ee channel	$e\mu$ channel	$\mu\mu$ channel
Non-prompt	6.7±2.5	20.0±7.7	10.3±5.3
Charge mis-ID	21.8±4.7	27.3±6.3	-
$WZ/\gamma*$	2.32±0.45	4.92±0.89	2.11±0.42
$W\gamma$	$1.75^{+0.74}_{-0.67}$	$2.29^{+0.91}_{-0.82}$	$0.21^{+0.22}_{-0.21}$
ZZ	-	-	0.09±0.08
$t\bar{t}+W/Z$	7.2±3.1	18.3±7.8	10.5±4.5
Tot. Bkg.	39.7±6.3	72.8±13.0	23.3±7.1
$W^{\pm}W^{\pm}jj$ ewk.+strong	0.81±0.10	2.57±0.28	1.55±0.18
Tot. Predicted	40.5±6.4	75.3±13.1	24.8±7.1
Data	46	82	36

Table 4.11: Expected and observed numbers of events in Top Control Region. The non-prompt background makes up 17% to 40% of the total background in different channels. Good agreement is observed between data and expectation.

4.6.2.4 Non-prompt Background in the Signal Regions

In Equation 4.18, the contribution from loose+loose sample is double counted and needs to be subtracted. Prompt and charge mis-ID contribution is also subtracted using MC simulation. The subtracted number of events is shown in Table 4.12.

The final non-prompt background estimation in signal regions is shown in Table 4.13 for the two signal regions in different channels.

4.6.3 Prompt Backgrounds

The dominating prompt background is $W^{\pm}Zjj$ which can be split into electroweak and strong productions as done for $W^{\pm}W^{\pm}jj$. The interference between the elec-

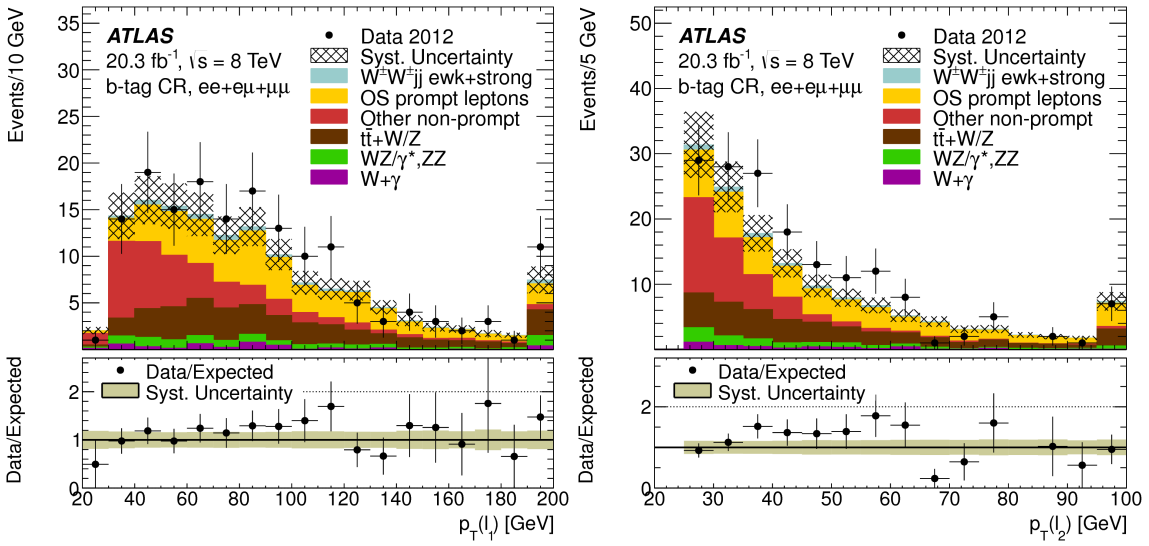

Figure 4.25: The leading lepton p_{T} distribution (left) and the sub-leading lepton p_{T} distribution (right) in the Top Control Region. The non-prompt background dominates the low p_{T} region. The error band includes all statistical and systematic uncertainties.

loose+loose contribution			
	ee channel	$e\mu$ channel	$\mu\mu$ channel
Inclusive SR	0.01	0.02	0.004
VBS SR	0.01	0.02	0.004
prompt+charge mis-ID contribution			
Inclusive SR	0.13	0.13	0.004
VBS SR	0.09	0.10	0.004

Table 4.12: Number of events subtracted for loose+loose, prompt and charge mis-ID contributions from the tight+loose estimation.

Signal Region	ee channel	$e\mu$ channel	$\mu\mu$ channel
Inclusive SR	0.61±0.17(stat.)±0.24(syst.)	1.85±0.20±0.74	0.41±0.06±0.21
VBS SR	0.50±0.16±0.20	1.50±0.18±0.60	0.34±0.06±0.18

Table 4.13: Expected non-prompt background contributions to the signal regions. Both statistical and systematic uncertainties are given.

troweak and strong productions for $W^{\pm}Zjj$ is highly suppressed and negligible. Both $W^{\pm}Zjj$-Ewk and $W^{\pm}Zjj$-Strong backgrounds are estimated using SHERPA MC simulation.

The $W^{\pm}Zjj$-Ewk production includes diagrams with b-quark in the initial state,

which is not included in any available NLO MC generators. This part is normalized to LO cross sections as predicted in SHERPA and assigned a conservative 50% uncertainty. The with-b diagrams contribute to around a third of the total fiducial cross section but will be highly suppressed after the b-jet veto cut in the signal region selections. The part without b-quark in the initial state is normalized to cross section calculated at NLO using VBFNLO and the uncertainties are evaluated at LO using VBFNLO given that VBFNLO can only output LO events. A summary of the systematic uncertainties on the $W^{\pm}Zjj$-Ewk without b-quark in the initial state is given in Table 4.14. The fiducial signal region definitions are modified for $WZ/\gamma*$ events, requiring three leptons instead of two with the $m_{\ell\ell}$ cut applied to all lepton pair combinations and no lepton charge requirement applied.

$W^{\pm}Zjj$-Ewk w/o b-quark in the initial state			
Source	Inclusive Fiducial SR	VBS Fiducial SR	Comment
MC stat. uncert.	1%	2%	
Parton shower	9%	10%	PYTHIA8 vs. HERWIG++
Scale	2%	5%	scale variations
PDF	6%	12%	CT10 eigenvector variations
Total	12%	17%	

Table 4.14: Summary of systematic uncertainties on $W^{\pm}Zjj$-Ewk (without b-quark in the initial state) production cross sections in the two fiducial regions.

The total $W^{\pm}Zjj$-Ewk production cross sections in the two fiducial regions, combining both with-b and without-b contributions, are:

$$\sigma^{W^{\pm}Zjj-\text{Ewk}}_{\text{Incl. Fid. SR}} = 0.395 \pm 0.091 \text{ fb}, \tag{4.22}$$

$$\sigma^{W^{\pm}Zjj-\text{Ewk}}_{\text{VBS Fid. SR}} = 0.34 \pm 0.91 \text{ fb}. \tag{4.23}$$

The extrapolated cross section for the SHERPA sample is 73 fb and 75 fb starting from the Inclusive Fiducial SR and VBS Fiducial SR respectively.

The $W^{\pm}Zjj$-Strong production cross section is evaluated in a similar way as for $W^{\pm}Zjj$-Ewk. An additional uncertainty arises from $WZ/\gamma*$ plus 0 or 1 parton events which show up in the fiducial signal regions after gaining extra jets from the parton showering. This is evaluated using dedicated MADGRAPH [80] MC samples. A summary of the systematic uncertainties on the $W^{\pm}Zjj$-Strong production cross sections in the two fiducial signal regions are given in Table 4.15.

$W^{\pm}Zjj$-Ewk without b-quark in the initial state			
Source	Inclusive Fiducial SR	VBS Fiducial SR	Comment
MC stat. uncert.	2%	2%	
Parton shower	12%	7%	PYTHIA8 vs. HERWIG++
$WZ/\gamma*+0$, 1 parton	6%	6%	Dedicated MADGRAPH sample
Scale	6%	6%	scale variations
PDF	5%	5%	CT10 eigenvector variations
Total	16%	12%	

Table 4.15: Summary of systematic uncertainties on $W^{\pm}Zjj$-Strong production cross sections in the two fiducial regions.

The $W^{\pm}Zjj$-Strong production cross sections with the uncertainties are:

$$\sigma^{W^{\pm}Zjj-\text{Strong}}_{\text{Incl. Fid. SR}} = 1.04 \pm 0.17 \text{ fb}, \tag{4.24}$$

$$\sigma^{W^{\pm}Zjj-\text{Strong}}_{\text{VBS Fid. SR}} = 0.640 \pm 0.077 \text{ fb}. \tag{4.25}$$

The extrapolated production cross sections for SHERPA sample is 12.4 fb and 12.8 fb starting from the Inclusive Fiducial SR and VBS Fiducial SR respectively.

The other less significant prompt backgrounds include:

- $W\gamma$: The $W\gamma$ background is estimated using ALPGEN [81–83] MC simulation showered with HERWIG++. The MC sample is normalized to NLO cross section with 17% total uncertainty, resulting from scale, PDF and differential cross section uncertainty for 2-jet and 3-jet bins.
- $t\bar{t}+W/Z$: The $t\bar{t}$ production in association with W/Z boson is estimated using MADGRAPH MC simulation normalized to NLO cross section with 30% uncertainty.
- $ZZjj$: The ZZ production in association with two jets is estimated using SHERPA MC simulation normalized to NLO cross section with an uncertainty of 19%.

A Tri-lepton Control Region is checked for validating the prompt background estimation. It is defined by requiring one third lepton present in the event passing the veto lepton definition apart from the two nominal leptons. At least two jets are required and no b-jet candidate should be present. The $E_{\text{T}}^{\text{miss}}$ is required to be greater than 40 GeV. No cuts on m_{jj} and $\Delta y(jj)$ are applied. The events selected in Tri-lepton CR are exactly the events thrown away by the third lepton veto and are dominated with WZ production. The event yields in Tri-lepton CR are shown in Table 4.16. Good agreement is observed between data and the expectation from

background estimation.

Tri-lepton Control Region				
Process	$e^{\pm}e^{\pm}\ell^{\mp}$	$e^{\pm}\mu^{\pm}\ell^{\mp}$	$\mu^{\pm}\mu^{\pm}\ell^{\mp}$	Total
$W^{\pm}W^{\pm}jj$-Ewk+Strong	0.01±0.01	0.11±0.02	-	0.12±0.02
$WZ/\gamma*$	32±5	96±16	57±10	186±31
ZZ	2.2±0.6	5.3±1.3	1.8±0.5	9.2±2.1
$t\bar{t}+W/Z$	0.65±0.28	2.4±1.0	1.0±0.5	4.1±1.7
Non-prompt	0.48±0.32	6±5	-	7±5
Total Predicted	36±6	110±18	60±10	206±33
Data	40	104	48	192

Table 4.16: Expected and observed numbers of events in the Tri-lepton CR. The uncertainties listed include both statistical and systematic uncertainties combined.

The m_{jj} and $\Delta y(jj)$ distributions in the Tri-lepton CR are shown in Figure 4.26. Both the two variables are well reproduced in the MC simulation.

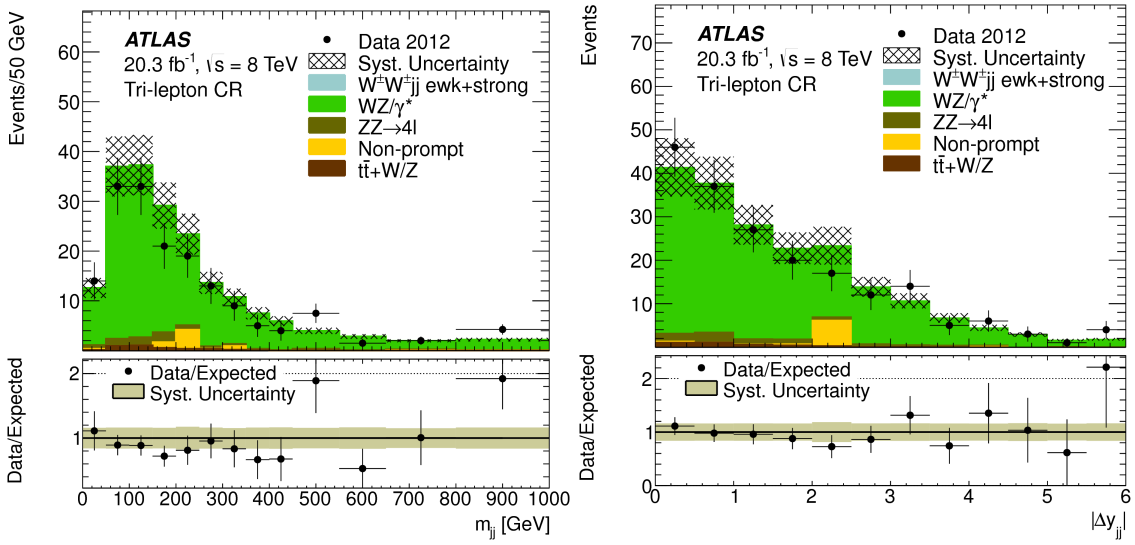

Figure 4.26: The m_{jj} (left) and $\Delta y(jj)$ (right) distributions in the Tri-lepton CR.

4.6.4 Low m_{jj} Control Region

In the two signal regions, the m_{jj} is required to be greater than 500 GeV. The region with m_{jj} below 500 GeV (after all other signal selection cuts except the $\Delta y(jj)$ cut) is used as a control region to check the overall background estimation. The expected and observed numbers of events in the Low m_{jj} CR are given in Table 4.17.

The $\Delta y(jj)$ distribution is shown in Figure 4.27. The jet and lepton η distributions are shown in Figure 4.28 and 4.29. Good agreement is seen between the expectation and data observation, demonstrating an excellent background estimation.

Low m_{jj} Control Region				
Process	$e^{\pm}e^{\pm}$	$e^{\pm}\mu^{\pm}$	$\mu^{\pm}\mu^{\pm}$	Total
$W^{\pm}W^{\pm}jj$-Ewk+Strong	6.5±0.7	18.8±1.9	11.4±1.2	37±4
$WZ/\gamma*,ZZ$	25±4	54±9	18.4±3.1	98±16
$W\gamma$	14±4	20±6	-	34±10
$t\bar{t}+W/Z$	1.7±0.7	3.8±1.6	2.4±1.0	7.9±3.4
Charge mis-ID	19.4±2.3	8.4±1.4	-	27.8±3.4
Non-prompt	9±4	21±8	8±4	39±10
Total Predicted	76±9	127±16	40±6	243±27
Data	78	120	30	228

Table 4.17: Expected and observed numbers of events in the Low m_{jj} CR. The uncertainties listed include both statistical and systematic uncertainties combined.

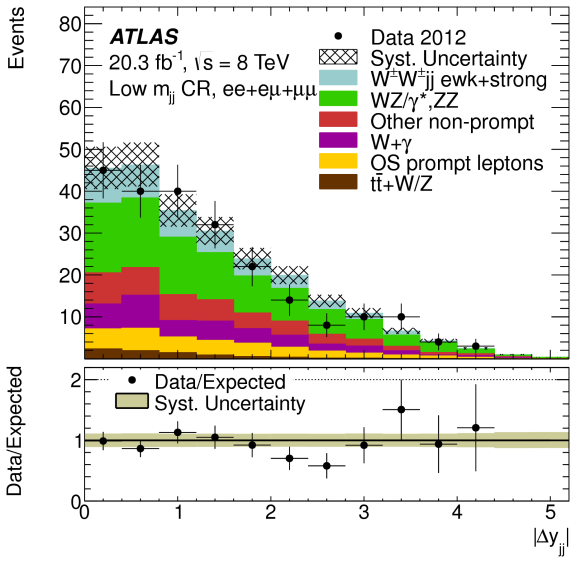

Figure 4.27: The $\Delta y(jj)$ distribution in the Low m_{jj} CR.

4.7 Systematic Uncertainty

The systematic uncertainties associated with the charge mis-ID background estimation and non-prompt background estimation have been presented in Section 4.6.1

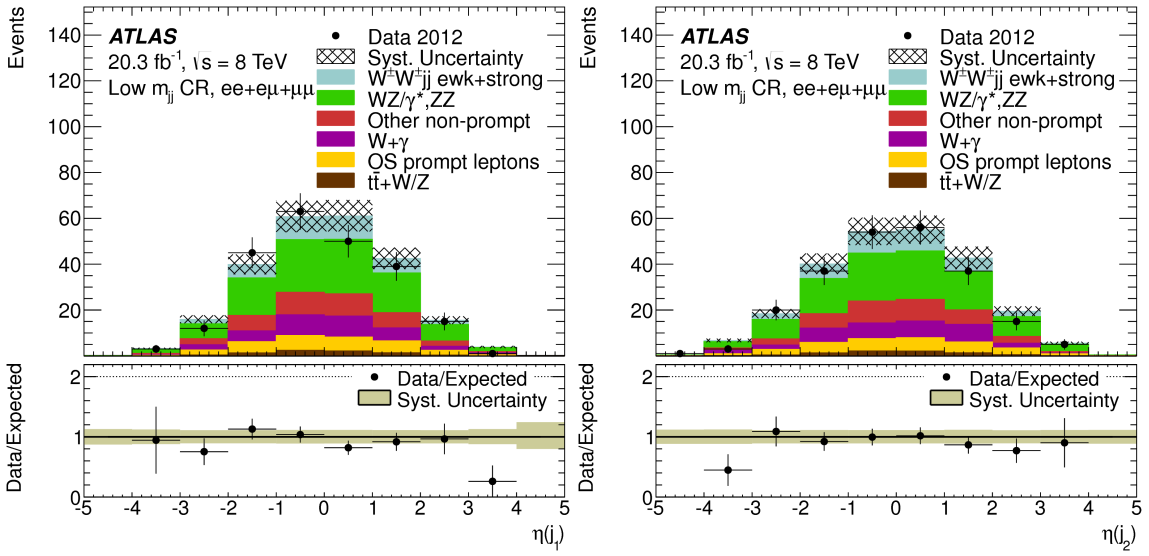

Figure 4.28: The leading-p_{T} and sub-leading-p_{T} jet η distribution in the Low m_{jj} CR.

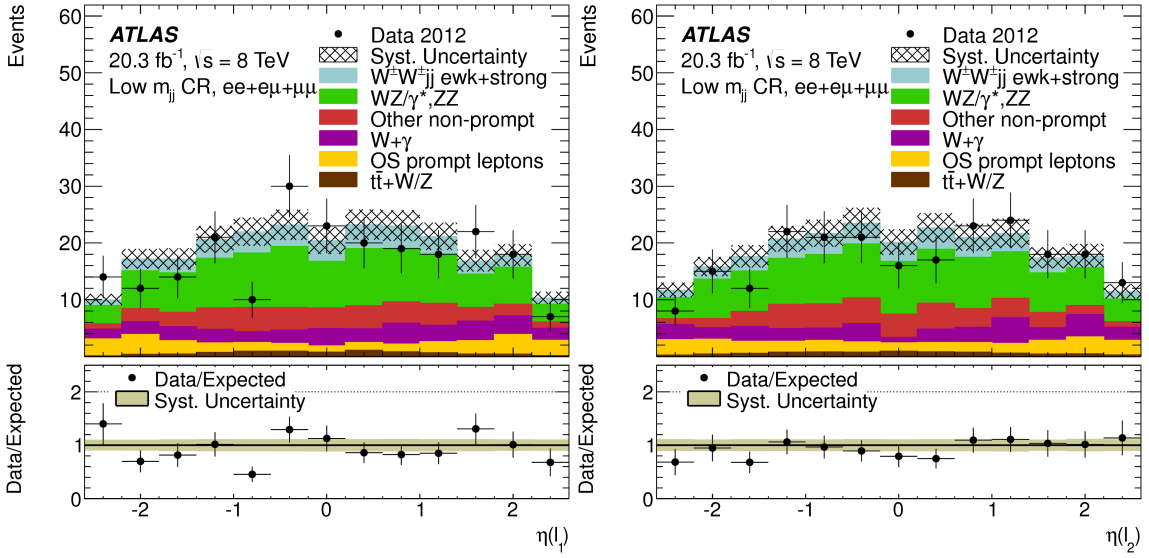

Figure 4.29: The leading-p_{T} and sub-leading-p_{T} lepton η distribution in the Low m_{jj} CR.

and Section 4.6.2 respectively. Theory uncertainties for the signal and prompt background simulation have been presented in Section 4.5 and Section 4.6.3. For the signal and background MC simulation, other sources of systematic uncertainties are also considered:

- Electron energy scale and resolution;
- Muon momentum scale and resolution;
- Electron reconstruction and identification efficiency scale factors;
- Muon reconstruction efficiency scale factors;
- Electron and muon trigger efficiency scale factors;
- JVF cut efficiency;
- Jet energy scale and resolution;
- b-jet tagging efficiency;
- Pile-up jets simulation;
- $E_{\mathrm{T}}^{\mathrm{miss}}$ scale and resolution associated with the soft terms not included in the lepton/jet energy uncertainties;
- Luminosity (2.8%);
- Photon conversion rate for $W\gamma$ background.

All these uncertainties are evaluated using performance packages provided by the ATLAS performance groups except the uncertainties associated with pile-up jet simulation and photon conversion rate for $W\gamma$ background. The uncertainties associated with pile-up jets are evaluated in a conservative way. In the MC at truth level, the jets can be matched to truth partons to decide whether the jets come from pile-up events. The jets which can not be matched to any partons are removed from the jet collections and the event yield is recalculated for estimating the uncertainties. Since this is the extreme case where no pile-up jets are simulated in the MC at all, the uncertainties are conservatively estimated. In Figure 4.7, the electron charge mis-ID rate is found to be different in high-η region between data and MC. Since the $W\gamma$ background is estimated using MC simulation and the $W\gamma$ event enters the signal region selections through photon conversion, the mis-modeling of the photon conversion rate brings biase to the $W\gamma$ background estimation. This is estimated by propagating the relative difference as observed in Figure 4.7 to the $W\gamma$ MC samples.

An additional uncertainty arises for the interference term of the signal production. As noted in Section 4.5, the interference contribution is included by scaling up the electroweak production component, assuming the interference term has the same detector efficiency as the electroweak production. The uncertainty on the detector efficiency for the interference component is estimated by assuming instead the detector efficiency to be the same as the strong production component and the overall difference is found to be 0.5% in both two signal regions.

Systematic Uncertainties in the Inclusive SR			
Source	$ee/e\mu/\mu\mu$	Signal	$ee/e\mu/\mu\mu$
Jet reconstruction	11/13/13	Jet reconstruction	5.7
Theory WZ/γ^*	5.6/7.7/11	Theory $W^{\pm}W^{\pm}jj$-ewk	4.7
MC statistics	8.2/5.9/8.4	Theory $W^{\pm}W^{\pm}jj$-strong	3.1
Non-prompt	3.5/7.1/7.2	Luminosity	2.8
Charge mis-ID	5.9/4.2/–	MC statistics	3.5/2.1/2.8
Theory $W\gamma$	2.8/2.6/–	$E_{\mathrm{T}}^{\mathrm{miss}}$ reconstruction	1.1
$E_{\mathrm{T}}^{\mathrm{miss}}$ reconstruction	2.2/2.4/1.8	Lepton reconstruction	1.9/1.0/0.7
Luminosity	1.7/2.1/2.4	b-tagging efficiency	0.6
Lepton reconstruction	1.6/1.2/1.2	Lepton trigger efficiency	0.1/0.3/0.5
b-tagging efficiency	1.0/1.1/1.0		
Lepton trigger efficiency	0.1/0.2/0.4		

Table 4.18: Summary of major systematic uncertainties in the Inclusive Signal Region. Relevant sources have been combined and the uncertainties are shown as relative uncertainties on the total number of background and signal events. The dominant source of uncertainty is the jet reconstruction uncertainties, including jet energy scale, jet energy resolution and pile-up jet simulation.

A summary of all systematic uncertainties is given in Table 4.18 for the Inclusive Signal Region and in Table 4.19 for the VBS Signal Region.

4.8 Signal Regions

The expected and observed numbers of events in the Inclusive Signal Region and VBS Signal Region are shown in Table 4.20 and Table 4.21 respectively. In both signal regions, significant excess is observed when comparing data to backgrounds only. The total expected number of events from signal and backgrounds combined agree well with observation in data.

The m_{jj} distribution after all selection cuts but before applying the $m_{jj} > 500$ GeV cut and the $\Delta y(jj) > 2.4$ cut is shown for ee, $e\mu$, $\mu\mu$ and the combined channel in Figure 4.30. The $\Delta y(jj)$ distribution after all selection cuts including the $m_{jj} > 500$ GeV cut but before the $\Delta y(jj) > 2.4$ cut, i.e. the Inclusive Signal region, is shown in Figure 4.31.

The lepton centrality ζ is a variable characterizing the orientation of the two leptons with respect to the two tagging jets. If we label the two leptons and two

Systematic Uncertainties in the VBS SR			
Source	$ee/e\mu/\mu\mu$	Signal	$ee/e\mu/\mu\mu$
Jet reconstruction	13/15/15	Theory $W^{\pm}W^{\pm}jj$-ewk	6.0
Theory WZ/γ^{*}	4.5/5.4/7.8	Jet reconstruction	5.1
MC statistics	8.9/6.4/8.4	Luminosity	2.8
Non-prompt	4.0/7.2/6.8	MC statistics	4.5/2.7/3.7
Charge mis-ID	5.5/4.4/–	$E_{\mathrm{T}}^{\mathrm{miss}}$ reconstruction	1.1
$E_{\mathrm{T}}^{\mathrm{miss}}$ reconstruction	2.9/3.2/1.4	Lepton reconstruction	1.9/1.0/0.7
Theory $W\gamma$	2.6/2.6/–	b-tagging efficiency	0.6
Luminosity	1.7/2.1/2.4	Lepton trigger efficiency	0.1/0.3/0.5
Theory $W^{\pm}W^{\pm}jj$-strong	0.9/1.5/2.6		
Lepton reconstruction	1.7/1.1/1.1		
b-tagging efficiency	0.8/0.9/0.7		
Lepton trigger efficiency	0.1/0.2/0.4		

Table 4.19: Summary of major systematic uncertainties in the VBS Signal Region. Relevant sources have been combined and the uncertainties are shown as relative uncertainties on the total number of background and signal events. The dominant source of uncertainty is the jet reconstruction uncertainties, including jet energy scale, jet energy resolution and pile-up jet simulation.

	Inclusive Signal Region		
Process	$e^{\pm}e^{\pm}$	$e^{\pm}\mu^{\pm}$	$\mu^{\pm}\mu^{\pm}$
$WZ/\gamma*$	2.74±0.64	5.6±1.3	2.42±0.57
Charge mis-ID	2.07±0.38	0.77±0.27	-
Non-prompt	0.61±0.30	1.85±0.76	0.41±0.22
$W\gamma$	1.11±0.61	1.59±0.78	-
ZZ	0.09±0.07	0.16±0.13	0.07±0.05
$t\bar{t}+W/Z$	0.15±0.06	0.25±0.10	0.11±0.05
$W^{\pm}W^{\pm}jj$-Ewk	3.07±0.30	9.00±0.80	4.90±0.50
$W^{\pm}W^{\pm}jj$-Strong	0.89±0.15	2.50±0.40	1.42±0.23
Total signal	3.96±0.41	11.4±1.1	6.29±0.62
Total background	6.8±1.2	10.3±2.0	3.01±0.63
Total predicted	10.7±1.4	21.7±2.6	9.3±1.0
Data	12	26	12

Table 4.20: Expected and observed numbers of events in the Inclusive Signal Region. In this signal region, the electroweak and strong production of $W^{\pm}W^{\pm}jj$ are both taken as the signal. The uncertainties listed include both the statistical and systematic uncertainties.

Process	VBS Signal Region $e^{\pm}e^{\pm}$	$e^{\pm}\mu^{\pm}$	$\mu^{\pm}\mu^{\pm}$
$WZ/\gamma*$	2.06±0.53	4.05±0.98	1.83±0.47
Charge mis-ID	1.39±0.27	0.64±0.24	-
Non-prompt	0.50±0.26	1.50±0.62	0.34±0.19
$W\gamma$	0.71±0.43	1.28±0.67	-
ZZ	0.04±0.04	0.05±0.04	0.01±0.01
$t\bar{t}+W/Z$	0.05±0.03	0.10±0.04	0.02±0.01
$W^{\pm}W^{\pm}jj$-Ewk	2.55±0.25	7.30±0.60	4.00±0.40
$W^{\pm}W^{\pm}jj$-Strong	0.25±0.06	0.71±0.14	0.38±0.08
Total signal	2.55±0.25	7.30±0.60	4.00±0.40
Total background	5.01±0.90	8.3±1.6	2.58±0.53
Total predicted	7.6±1.0	15.6±2.0	6.63±0.75
Data	6	18	10

Table 4.21: Expected and observed numbers of events in the VBS Signal Region. In this signal region, only the electroweak production of $W^{\pm}W^{\pm}jj$ is taken as the signal while the strong production is taken as a background. The uncertainties listed include both the statistical and systematic uncertainties.

jets such that $\eta(j_1) > \eta(j_2)$ and $\eta(\ell_1) > \eta(\ell_2)$, then lepton centrality is defined as:

$$\zeta = min\{\eta(j_1) - \eta(\ell_1), \eta(\ell_2) - \eta(j_2)\} \tag{4.26}$$

For a typical VBS event, where the two leptons are in the central region relative to the two jets or in other words $\eta(j_1) > \eta(\ell_1) > \eta(\ell_2) > \eta(j_2)$, the lepton centrality ζ is larger than zero. If any of the two lepton is outside the η gap between the two jets, ζ is smaller than zero. The lepton centrality distribution is shown in Figure 4.32 for the Inclusive Signal Region and VBS Signal Region. The $W^{\pm}W^{\pm}jj$-Electroweak is centered towards the positive direction and the backgrounds have a distribution centered around zero, indicating that in the background events the two leptons are oriented randomly with respect to the two jets.

The behavior of the di-boson invariant mass in high mass region is one of the most interesting feature for VBS. If the Higgs particle discovered is not exactly the SM one, enhancement of event rate at high mass should be observed. Given the presence of two neutrinos in the final state, the invariant mass of the $W^{\pm}W^{\pm}$ system can not be fully reconstructed. The transverse mass of the $\ell\ell$+$E_{\mathrm{T}}^{\mathrm{miss}}$ system is shown in Figure 4.33 for the VBS Signal Region. Due to the limited data sample size, the number of events expected in the high mass region is very small. More

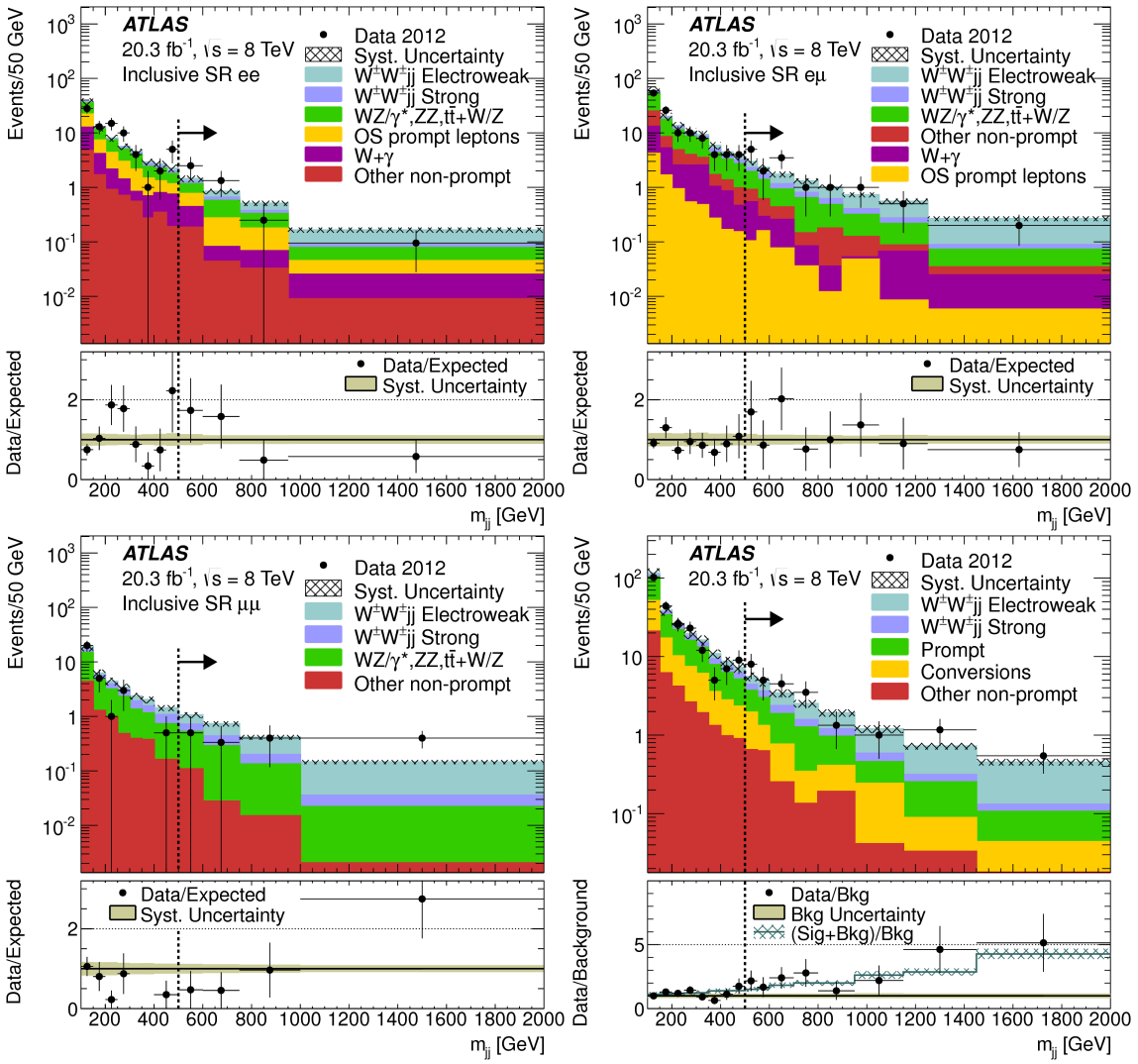

Figure 4.30: The m_{jj} distribution in ee, $e\mu$, $\mu\mu$ and combined channels before the $m_{jj} > 500$ GeV cut and the $\Delta y(jj) > 2.4$ cut. The dashed line marks the position of 500 GeV. The region on the right to the dashed line is defined as the Inclusive Signal Region. In the plot for the combined channel, the ratio of data over background only is shown in the bottom. As the m_{jj} gets large, the ratio deviates from one, indicating the background only assumption does not describes the data any more. After adding the signal expectation in, the gap between the background and data is nicely filled.

data is needed for studying the dynamics of the high mass region.

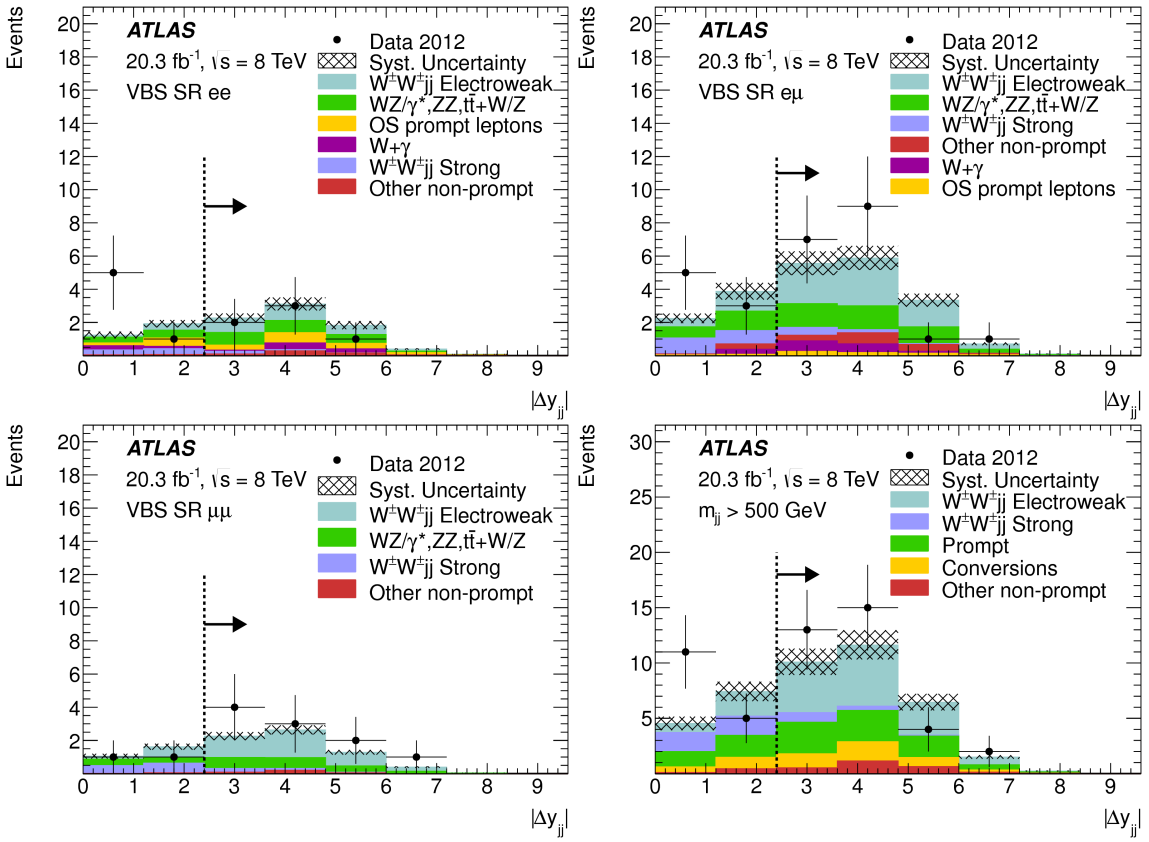

Figure 4.31: The $\Delta y(jj)$ distribution in ee, $e\mu$, $\mu\mu$ and combined channels in the Inclusive Signal Region. The dashed line marks the position of 2.4. The region on the right to the dashed line is defined as the VBS Signal Region. As can be seen from the plots, the cut $\Delta y(jj) > 2.4$ helps further remove the $W^{\pm}W^{\pm}jj$-Strong production.

4.9 Cross Section Measurement

As noted previously, in the Inclusive Signal Region $W^{\pm}W^{\pm}jj$-Ewk, $W^{\pm}W^{\pm}jj$-Strong and the interference combined is taken as the signal and in the VBS Signal Region only the $W^{\pm}W^{\pm}jj$-Ewk and the interference is taken as the signal. The production cross section of the signal in the two fiducial signal regions is extracted using a likelihood function.

Given either of the two fiducial signal regions, denote $\sigma_{W^{\pm}W^{\pm}jj}$ as the fiducial production cross section. Let A_i be the relative event yield for each of the di-lepton channels (ee, $e\mu$ or $\mu\mu$), which should be 25%:50%:25% given the lepton universality. The actual values of A_i as calculated at truth level using the SHERPA MC

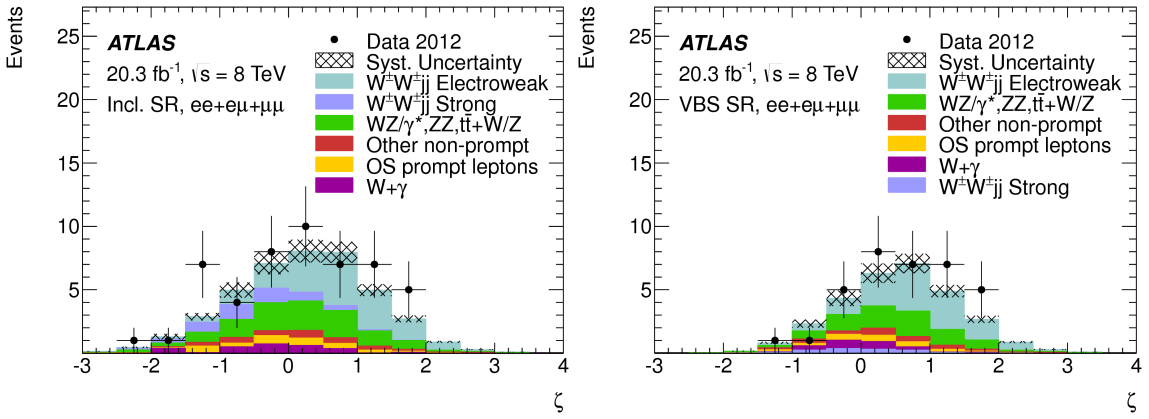

Figure 4.32: The lepton centrality (ξ) distribution for the combined channel in the Inclusive Signal Region (left) and the VBS Signal Region (right). The $\Delta y(jj) > 2.4$ cut applied for the VBS Signal Region has caused the ζ distribution for the background to shift towards the positive direction.

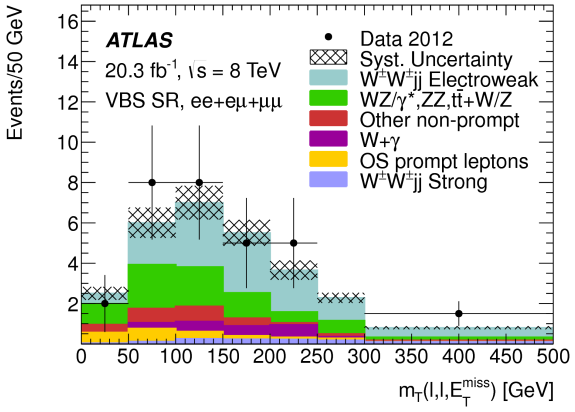

Figure 4.33: The $m_{\mathrm{T}}(\ell, \ell, E_{\mathrm{T}}^{\mathrm{miss}})$ distribution for the combined channel in the VBS Signal Region. In the highest bin (including overflow), 6 events are observed and 4 events are expected.

samples are given in Table 4.22. They differ from the expectation because the truth jet algorithm clusters electrons but not muons and causes slight difference in the treatment of the two flavors of leptons at truth level. Let ϵ_i denote the detector efficiency for the signal in each channel (shown in Table 4.23), θ_j the nuisance parameter which represents each of the systematic uncertainties and $\mathcal{L}$ the integrated luminosity of the data sample. The total expected number of events in channel i is

	A_i		
Signal Region	$e^{\pm}e^{\pm}$	$e^{\pm}\mu^{\pm}$	$\mu^{\pm}\mu^{\pm}$
Inclusive SR	23.2%	52.4%	26.5%
VBS SR	23.5%	52.7%	25.7%

Table 4.22: The fraction of each di-lepton channel relative to the total production as calculated at truth level using the SHERPA MC simulation.

then given by:

$$N^i_{\text{exp,tot}} = N^i_{\text{exp,sig.}} + N^i_{\text{exp,bkg}} \tag{4.27}$$

$$= \mathcal{L} \cdot \sigma_{W^{\pm}W^{\pm}jj} \cdot A_i \cdot \epsilon_i(\theta_j) + \sum_b N^i_b(\theta_j). \tag{4.28}$$

The sum over b runs over all background processes. The likelihood function is then defined as:

$$L(\sigma_{W^{\pm}W^{\pm}jj}, \theta_j) = \prod_i \text{Pois}(N^i_{\text{obs}}|N^i_{\text{exp,tot}}) \prod_j \text{Gauss}(\theta_j|\theta^0_j, 1). \tag{4.29}$$

The cross section is extracted by maximizing the likelihood function given the observed number of events in data. The uncertainties of the cross section are evaluated using a profiled likelihood ratio

$$\lambda(\sigma_{W^{\pm}W^{\pm}jj}) = \frac{L(\sigma_{W^{\pm}W^{\pm}jj}, \hat{\hat{\theta}}_j)}{L(\hat{\sigma}_{W^{\pm}W^{\pm}jj}, \hat{\theta}_j)} \tag{4.30}$$

where $\hat{\sigma}_{W^{\pm}W^{\pm}jj}$ and $\hat{\theta}_j$ maximize the denominator and $\hat{\hat{\theta}}_j$ maximizes the numerator given a specific value of $\sigma_{W^{\pm}W^{\pm}jj}$. The 68.3% confidence interval of $\sigma_{W^{\pm}W^{\pm}jj}$ is given by asking $-\ln\lambda$ =0.5 [84, 85].

The results of the cross section measurement are summarized in Table 4.24. A 4.5 σ signal significance is observed for the inclusive production of $W^{\pm}W^{\pm}jj$ and a 3.6 σ signal significance is observed for the electroweak production of $W^{\pm}W^{\pm}jj$. The measured production cross section in the Inclusive Fiducial SR is

$$\sigma^{W^{\pm}W^{\pm}jj-\text{Ewk+Strong+Int}}_{\text{Incl. Fid. SR}} = 2.1 \pm 0.5(\text{stat.}) \pm 0.3(\text{syst.}) \text{ fb}, \tag{4.31}$$

	ϵ_i		
Inclusive SR	$e^{\pm}e^{\pm}$	$e^{\pm}\mu^{\pm}$	$\mu^{\pm}\mu^{\pm}$
$W^{\pm}W^{\pm}jj$-Ewk	(56.7±1.5)%	(73.0±0.9)%	(80.4±1.1)%
$W^{\pm}W^{\pm}jj$-Strong	(54.5±2.3)%	(68.1±1.4)%	(77.3±1.8)%
VBS SR	$e^{\pm}e^{\pm}$	$e^{\pm}\mu^{\pm}$	$\mu^{\pm}\mu^{\pm}$
$W^{\pm}W^{\pm}jj$-Ewk	(57.2±1.6)%	(72.7±1.0)%	(82.7±1.2)%
$W^{\pm}W^{\pm}jj$-Strong	(53.4±3.8)%	(70.2±2.4)%	(73.7±3.2)%

Table 4.23: The detector efficiency for each channel of the signal region. The efficiency is calculated as the fraction of the total expected events in the fiducial signal region which are eventually selected in the signal region at reconstruction level. The uncertainties listed are only statistical uncertainties.

and in the VBS Fiducial SR

$$\sigma^{W^{\pm}W^{\pm}jj-\text{Ewk+Int}}_{\text{VBS Fid. SR}} = 1.3 \pm 0.4(\text{stat.}) \pm 0.2(\text{syst.})\ \text{fb}, \tag{4.32}$$

The expected production cross section is 1.52 ± 0.12 fb and 0.95 ± 0.07 fb in the Inclusive and VBS Fiducial Signal Segion respectively, as presented in Equation 4.9 and 4.10. The measured cross section is consistent with the SM expectation within one standard deviation.

4.10 aQGC Limits

Using the VBS Signal Region, we can set limits on the aQGC. The signal samples of $W^{\pm}W^{\pm}jj$-Ewk production with aQGC are generated using WHIZARD [86, 87] at LO for different values of α_4 and α_5 with K-matrix [25] unitarization. The aQGC points with fully simulated MC samples, together with the total cross section, the acceptance into the VBS Fiducial SR and the detector efficiencies are presented in Table 4.25. A finer grid of the fiducial cross section is shown in Figure 4.34. In this grid of fiducial cross section, an NLO/LO k-factor of 1.30 has been applied to all points. This k-factor is derived at the SM point by comparing the WHIZARD prediction of fiducial cross section at LO and at NLO as obtained in Section 4.5. The dependence of the k-factor on the aQGC points has been found to be flat and thus the same number is used for all points. The interference contribution is also added to the $W^{\pm}W^{\pm}jj$-Ewk for each aQGC point using the parameterization in Equation 4.8. The SM $W^{\pm}W^{\pm}jj$-Strong production cross section is used in the calcula-

Inclusive Fiducial SR			
Channel	Signal Significance (expected)	$\sigma_{W^{\pm}W^{\pm}jj}$ [fb]	95% CL Upper Limit [fb]
ee	1.6 (1.3)	$2.0^{+1.5}_{-1.3}$	-
$e\mu$	3.3 (2.6)	$2.1^{+0.8}_{-0.7}$	-
$\mu\mu$	3.5 (2.5)	$2.2^{+0.9}_{-0.8}$	-
combined	4.5 (3.4)	$2.1^{+0.6}_{-0.6}$	3.3
VBS Fiducial SR			
Channel	Signal Significance (expected)	$\sigma_{W^{\pm}W^{\pm}jj}$ [fb]	95% CL Upper Limit [fb]
ee	0.4 (1.1)	$0.4^{+1.1}_{-0.9}$	-
$e\mu$	2.4 (2.0)	$1.3^{+0.6}_{-0.6}$	-
$\mu\mu$	3.2 (2.1)	$1.7^{+0.8}_{-0.7}$	-
combined	3.6 (2.8)	$1.3^{+0.5}_{-0.4}$	2.2

Table 4.24: Summary of cross section measurement results. The signal significance is reported in units of standard deviation. The uncertainties on the measured cross section include both statistical and systematic uncertainties. The 95% CL upper limits are also reported given that the $W^{\pm}W^{\pm}jj$ production has not been observed at the LHC.

tion for all aQGC points.

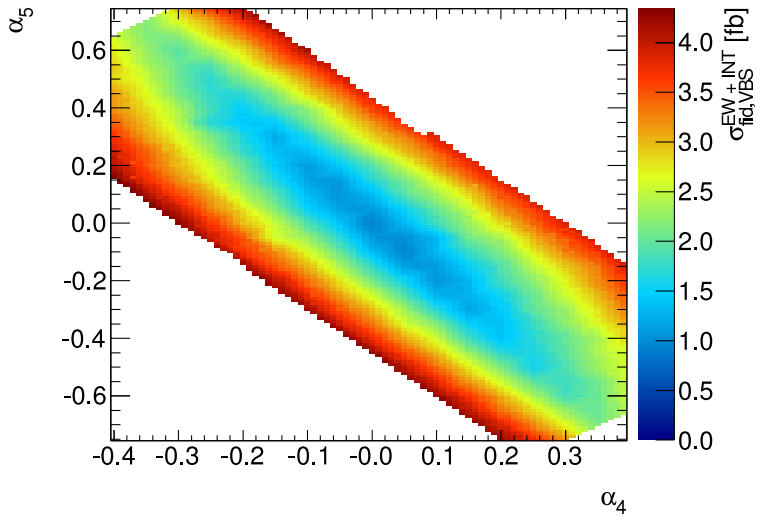

Figure 4.34: Production cross section of $W^{\pm}W^{\pm}jj$-Electroweak plus the interference term in the VBS Fiducial SR as a function of the aQGC parameters α_4 and α_5.

In the ideal case, the detector efficiency can be calculated for each point on the grid of Figure 4.34. Given the limited computing resources, it is impratical to generate a fully simulated sample for all these points. The detector efficiency is

α_4	α_5	$\sigma_{\text{sample PS}}$ [fb]	A [%]	ε_{ee} [%]	$\varepsilon_{e\mu}$ [%]	$\varepsilon_{\mu\mu}$ [%]
0.00	0.00	14.72 ± 0.02	4.61 ± 0.06	49.2 ± 2.3	62.5 ± 1.5	68.0 ± 2.1
0.00	0.10	16.93 ± 0.02	5.66 ± 0.06	55.1 ± 2.0	61.3 ± 1.4	71.9 ± 1.8
0.00	0.20	21.16 ± 0.02	6.63 ± 0.07	55.4 ± 1.8	70.2 ± 1.2	67.7 ± 1.7
0.00	-0.10	17.98 ± 0.02	5.61 ± 0.06	59.7 ± 1.9	66.7 ± 1.3	74.1 ± 1.8
0.00	-0.20	22.88 ± 0.02	7.09 ± 0.07	55.7 ± 1.7	66.5 ± 1.2	74.2 ± 1.6
0.10	0.00	19.13 ± 0.02	6.92 ± 0.07	54.8 ± 1.8	69.7 ± 1.2	69.6 ± 1.7
0.10	0.10	23.00 ± 0.02	7.32 ± 0.07	61.8 ± 1.6	65.9 ± 1.2	73.2 ± 1.6
0.10	-0.20	15.90 ± 0.02	4.75 ± 0.06	49.7 ± 2.2	66.0 ± 1.4	70.7 ± 2.1
0.10	-0.40	26.26 ± 0.02	7.04 ± 0.07	60.4 ± 1.7	68.8 ± 1.2	79.4 ± 1.5
0.20	-0.30	18.40 ± 0.02	5.76 ± 0.06	56.4 ± 1.9	66.8 ± 1.3	70.2 ± 1.8
0.30	-0.20	25.47 ± 0.03	7.78 ± 0.07	62.9 ± 1.6	71.0 ± 1.1	71.4 ± 1.5
0.30	-0.60	23.15 ± 0.02	5.86 ± 0.06	53.3 ± 1.9	62.0 ± 1.4	67.0 ± 1.9
-0.10	0.00	20.88 ± 0.02	6.64 ± 0.07	56.4 ± 1.8	66.3 ± 1.2	72.2 ± 1.7
-0.10	0.20	16.00 ± 0.02	5.15 ± 0.06	48.3 ± 2.0	62.1 ± 1.5	67.2 ± 2.0
-0.10	0.40	24.62 ± 0.02	6.83 ± 0.07	59.2 ± 1.7	69.2 ± 1.2	71.4 ± 1.7
-0.10	-0.10	25.62 ± 0.03	7.71 ± 0.07	61.6 ± 1.6	65.5 ± 1.2	69.1 ± 1.6
-0.20	0.30	19.28 ± 0.02	6.33 ± 0.07	54.1 ± 1.8	67.7 ± 1.3	68.4 ± 1.7
-0.30	0.20	28.60 ± 0.03	7.56 ± 0.07	58.8 ± 1.7	70.2 ± 1.1	68.1 ± 1.6
-0.30	0.60	23.13 ± 0.02	6.09 ± 0.07	55.1 ± 1.9	67.9 ± 1.2	72.4 ± 1.8

Table 4.25: The aQGC points with fully simulated MC samples. The cross section is given in the total produced sample phase space. The acceptance into the VBS Fiducial SR and the detector efficiency for each di-lepton channel are also presented. The uncertainties listed only include the statistical uncertainties.

checked using the 19 fully simulated MC samples as a function of the fiducial cross section. The results are shown in Figure 4.35. A linear parameterization is used for all points in the limit setting, which reads:

$$\epsilon_{ee} = 0.5222 + \frac{0.0565}{\text{fb}} \cdot \sigma^{W^{\pm}W^{\pm}jj-\text{Ewk, aQGC}}_{\text{VBS Fid. SR}}, \tag{4.33}$$

$$\epsilon_{e\mu} = 0.7004 + \frac{0.0301}{\text{fb}} \cdot \sigma^{W^{\pm}W^{\pm}jj-\text{Ewk, aQGC}}_{\text{VBS Fid. SR}}, \tag{4.34}$$

$$\epsilon_{\mu\mu} = 0.8144 + \frac{0.0143}{\text{fb}} \cdot \sigma^{W^{\pm}W^{\pm}jj-\text{Ewk, aQGC}}_{\text{VBS Fid. SR}}, \tag{4.35}$$

$$\tag{4.36}$$

The dependence on the fiducial cross section is rather flat. The stronger dependence in the ee channel is due to the Z mass window cut which is not applied to the other two channels.

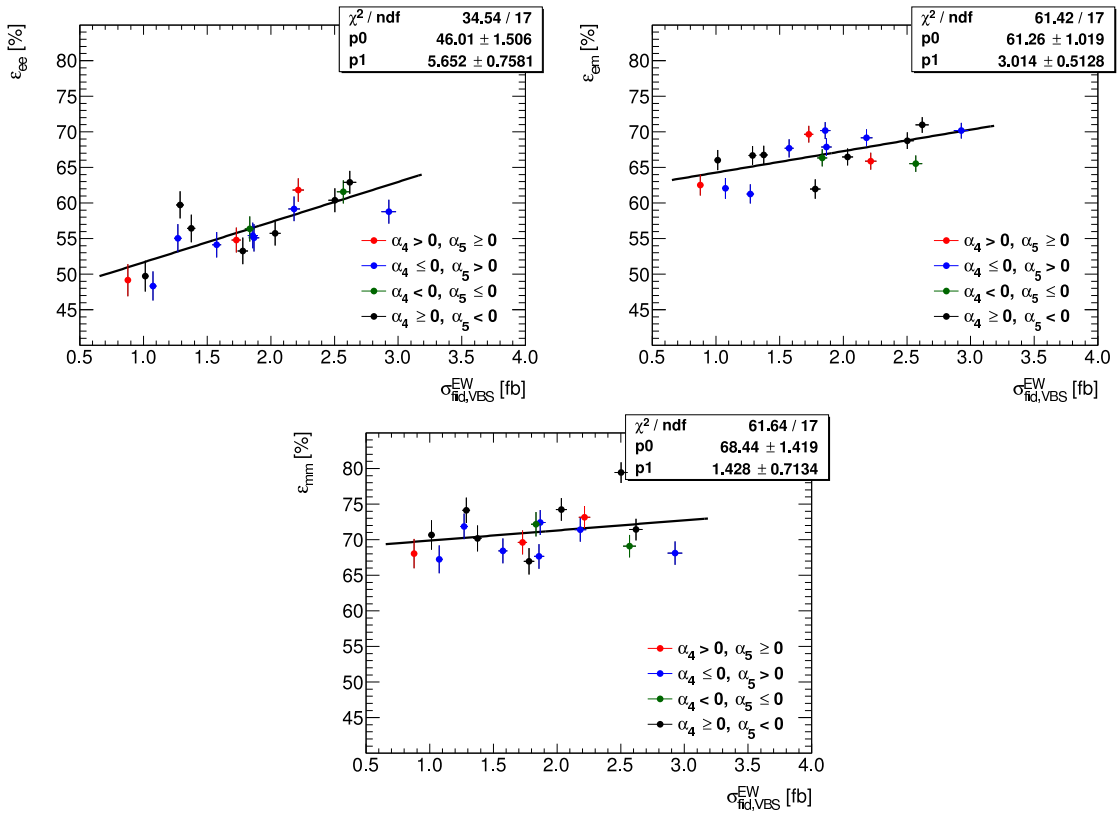

Figure 4.35: Detector efficiency for aQGC in ee (top left), $e\mu$ (top right) and $\mu\mu$ (bottom) channel as a function of the fiducial cross section.

Given a specific aQGC point (α_4, α_5), the expected number of events in the VBS

Signal Region in channel i should now become

$$N^{i,\text{aQGC}}_{\text{exp,tot}} = N^{i,\text{aQGC}}_{\text{exp,sig.}} + N^{i}_{\text{exp,bkg}} \tag{4.37}$$

$$= \mathcal{L} \cdot \sigma^{(\alpha_4,\alpha_5)}_{W^{\pm}W^{\pm}jj} \cdot A_i \cdot \epsilon_i(\theta_j, \sigma^{(\alpha_4,\alpha_5)}_{W^{\pm}W^{\pm}jj}) + \sum_b N^i_b(\theta_j). \tag{4.38}$$

We still take the likelihood function as a function of the cross section $\sigma^{(\alpha_4,\alpha_5)}_{W^{\pm}W^{\pm}jj}$ and the nuisance parameters θ_j, as in Equation 4.30. What is different now is the detector efficiency depends on the cross section for the aQGC point. The upper limits on the cross section are derived by asking the likelihood ratio $-\ln\lambda = 0.5$ at 68.3% CL and 1.92 at 95% CL [84, 85]. The limits on the cross section are then mapped onto the (α_4, α_5) plane as constraints on the aQGC. The results are shown in Figure 4.36. Due to slight excess observed in data in VBS Signal Region, the observed limits are slightly looser than the expected limits. These are the first set of constraints on the aQGC for $WWWW$ vertex.

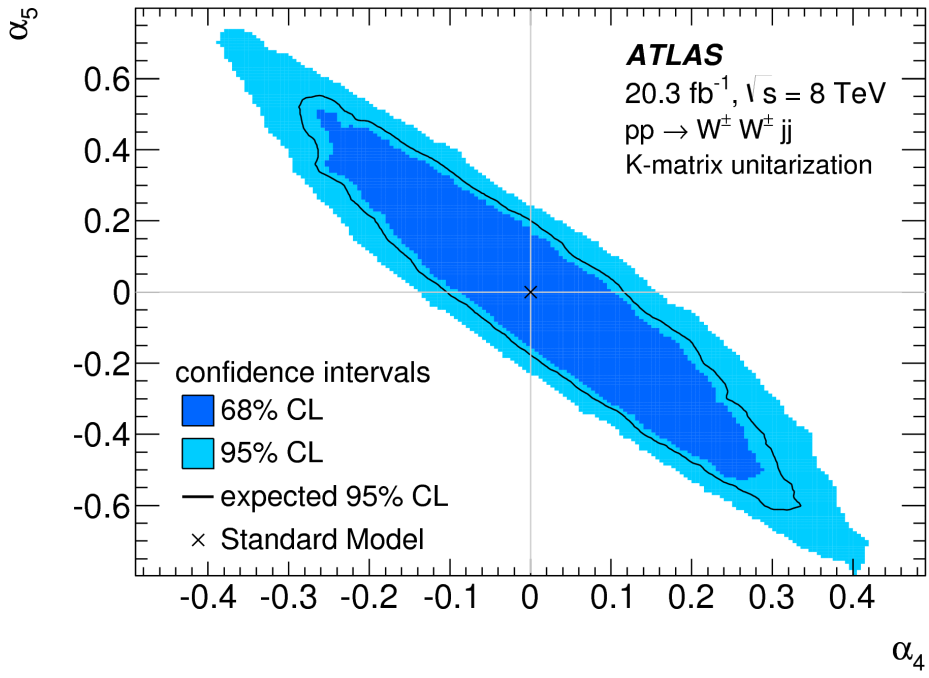

Figure 4.36: Exclusion limits on aQGC parameters (α_4, α_5). The limit contour is obtained by mapping the upper limit on the fiducial cross section onto the (α_4, α_5) plane. Points outside the light blue ellipse are excluded at 95% CL. Points outside the dark blue ellipse are excluded at 68% CL. The expected 95% CL exclusion is given by the solid line.

CHAPTER 5

Conclusion and Outlook

A first measurement of the $W^{\pm}W^{\pm}jj$ production at $\sqrt{s} = 8$ TeV has been presented, with 4.5 and 3.6 standard deviations of signal significance for the inclusive and electroweak production respectively. The measured cross section is found to be in agreement with the SM. Constraints are derived on the aQGC for $WWWW$ vertex. The results have been published in Ref. [88]. In Figure 5.1, a summary of all cross section measurements at ATLAS is presented. As of July 2014, the $W^{\pm}W^{\pm}jj$-Ewk fiducial production cross section is so far the smallest cross section measured at ATLAS and the first one to hit the fb line.

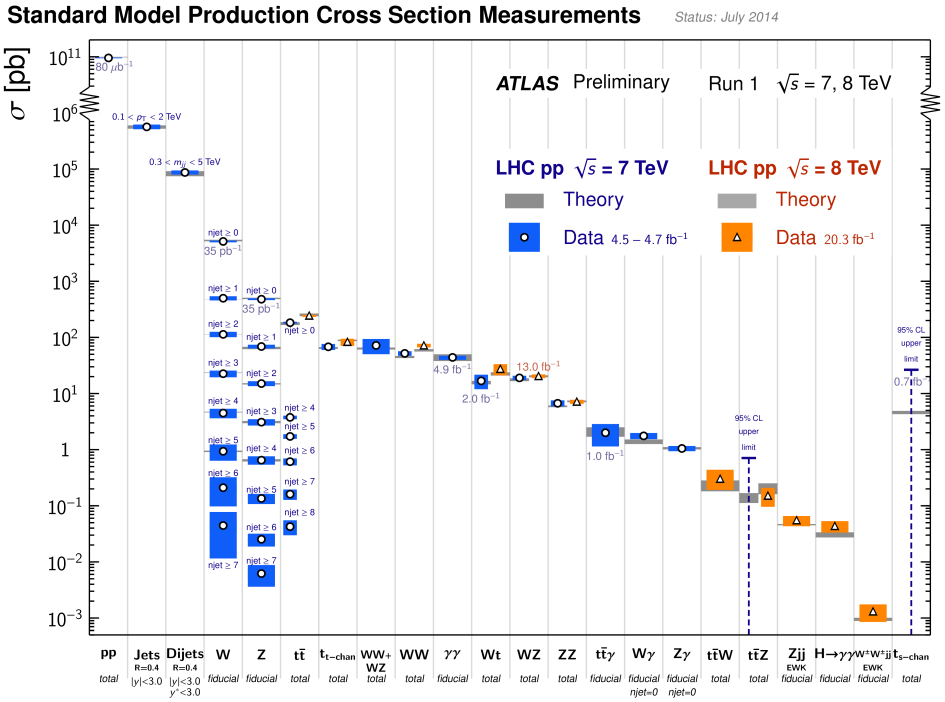

Figure 5.1: Summary of SM production cross section measurements at ATLAS, as of July 2014.

This analysis is still largely constrained by the statistical uncertainties associated with the data sample. In the coming year 2015, LHC will restart operation at an increased center-of-mass energy of $\sqrt{s} = 13$ TeV, which will increase the production cross section of $W^{\pm}W^{\pm}jj$ by a factor of $\sim$3. Significant improvement in signal sensitivity is expected with $\sim$10 fb^{-1} of data next year and $\sim$100 fb^{-1} of data in the next three years. More interesting studies can be done in the $WZ \to \ell\nu\ell\ell$ or $WV \to \ell\nu jj$ final state to extract the polarization information of the two W's which can be more sensitive to new physics contributing to the electroweak symmetry breaking [89].

APPENDIX A

Monte Carlo Samples

The Monte Carlo scamples used in this thesis are listed in the following tables.

Sample Name	Cross Section [pb]	k-Factor	Filter Efficiency
mc12_8TeV.185393.Sherpa_CT10_lnln_ls_EWK_MassiveCB	0.02762	0.8356	1.0
mc12_8TeV.185394.Sherpa_CT10_lnln_ls_QCD_MassiveCB	0.01608	1.0354	1.0
mc12_8TeV.185396.Sherpa_CT10_lllnu_WZ_EWK_MassiveCB	0.082102	0.8944	1.0
mc12_8TeV.179974.Sherpa_CT10_lllnu_WZ_MassiveCB.merge	9.7446	1.2704	1.0
mc12_8TeV.185397.Sherpa_CT10_lllnu_WZ_l10_MassiveCB	9.7446	1.2704	0.24041
mc12_8TeV.161982.Sherpa_CT10_llnunu_ZZ_EW6	0.0041	1.0	1.0
mc12_8TeV.147196.Sherpa_CT10_llljj_ZZjj_EW6	0.00691	1.0	1.0
mc12_8TeV.147193.Sherpa_CT10_lnlnjj_WWjj_EW6	0.09588	1.0	1.0
mc12_8TeV.126892.Sherpa_CT10_llnunu_WW	5.4982	1.06	1.0
mc12_8TeV.126895.Sherpa_CT10_llnunu_ZZ	0.4962	1.05	1.0
mc12_8TeV.126894.Sherpa_CT10_llll_ZZ	8.7345	1.0	1.0

Table A.1: Di-boson Monte Carlo samples used in this thesis.

Sample Name	Cross Section [pb]	k-Factor	Filter Efficiency
mc12_8TeV.110001.McAtNloJimmy_CT10_ttbar_dilepton	238.06	1.0	1.0
mc12_8TeV.105200.McAtNloJimmy_CT10_ttbar_LeptonFilter	238.06	1.0	1.0
mc12_8TeV.105204.McAtNloJimmy_AUET2CT10_ttbar_allhad	238.06	1.0	1.0
mc12_8TeV.119353.MadGraphPythia_AUET2BCTEQ6L1_ttbarW	0.1041	1.18	1.0
mc12_8TeV.174830.MadGraphPythia_AUET2BCTEQ6L1_ttbarWjExcl	0.053372	1.18	1.0
mc12_8TeV.174831.MadGraphPythia_AUET2BCTEQ6L1_ttbarWjjIncl	0.041482	1.18	1.0
mc12_8TeV.119355.MadGraphPythia_AUET2BCTEQ6L1_ttbarZ	0.0678	1.34	1.0
mc12_8TeV.174832.MadGraphPythia_AUET2BCTEQ6L1_ttbarZjExcl	0.045357	1.34	1.0
mc12_8TeV.174833.MadGraphPythia_AUET2BCTEQ6L1_ttbarZjjIncl	0.039772	1.34	1.0
mc12_8TeV.108343.McAtNloJimmy_CT10NLOME_AUET2CTEQ6L1MPI_SingleTopSChanWenu	0.606	1.0	1.0
mc12_8TeV.108344.McAtNloJimmy_CT10NLOME_AUET2CTEQ6L1MPI_SingleTopSChanWmunu	0.606	1.0	1.0
mc12_8TeV.108345.McAtNloJimmy_CT10NLOME_AUET2CTEQ6L1MPI_SingleTopSChanWtaunu	0.606	1.0	1.0
mc12_8TeV.108346.McAtNloJimmy_CT10NLOME_AUET2CTEQ6L1MPI_SingleTopWtChanIncl	22.37	1.0	1.0
mc12_8TeV.117360.AcerMCPythia_AUET2BCTEQ6L1_singletop_tchan_e	9.48	1.0	1.0
mc12_8TeV.117361.AcerMCPythia_AUET2BCTEQ6L1_singletop_tchan_mu	9.48	1.0	1.0
mc12_8TeV.117362.AcerMCPythia_AUET2BCTEQ6L1_singletop_tchan_tau	9.48	1.0	1.0

Table A.2: Top Monte Carlo samples used in this thesis.

Sample Name	Cross Section [pb]	k-Factor	Filter Efficiency
mc12_8TeV.107650.AlpgenJimmy_AUET2CTEQ6L1_ZeeNp0	712.	1.23	1.0
mc12_8TeV.107651.AlpgenJimmy_AUET2CTEQ6L1_ZeeNp1	155.	1.23	1.0
mc12_8TeV.107652.AlpgenJimmy_AUET2CTEQ6L1_ZeeNp2	48.8	1.23	1.0
mc12_8TeV.107653.AlpgenJimmy_AUET2CTEQ6L1_ZeeNp3	14.2	1.23	1.0
mc12_8TeV.107654.AlpgenJimmy_AUET2CTEQ6L1_ZeeNp4	3.77	1.23	1.0
mc12_8TeV.107655.AlpgenJimmy_AUET2CTEQ6L1_ZeeNp5	1.12	1.23	1.0
mc12_8TeV.107660.AlpgenJimmy_AUET2CTEQ6L1_ZmumuNp0	712.	1.23	1.0
mc12_8TeV.107661.AlpgenJimmy_AUET2CTEQ6L1_ZmumuNp1	155.	1.23	1.0
mc12_8TeV.107662.AlpgenJimmy_AUET2CTEQ6L1_ZmumuNp2	48.8	1.23	1.0
mc12_8TeV.107663.AlpgenJimmy_AUET2CTEQ6L1_ZmumuNp3	14.2	1.23	1.0
mc12_8TeV.107664.AlpgenJimmy_AUET2CTEQ6L1_ZmumuNp4	3.77	1.23	1.0
mc12_8TeV.107665.AlpgenJimmy_AUET2CTEQ6L1_ZmumuNp5	1.12	1.23	1.0
mc12_8TeV.107670.AlpgenJimmy_AUET2CTEQ6L1_ZtautauNp0	712.	1.23	1.0
mc12_8TeV.107671.AlpgenJimmy_AUET2CTEQ6L1_ZtautauNp1	155.	1.23	1.0
mc12_8TeV.107672.AlpgenJimmy_AUET2CTEQ6L1_ZtautauNp2	48.8	1.23	1.0
mc12_8TeV.107673.AlpgenJimmy_AUET2CTEQ6L1_ZtautauNp3	14.2	1.23	1.0
mc12_8TeV.107674.AlpgenJimmy_AUET2CTEQ6L1_ZtautauNp4	3.77	1.23	1.0
mc12_8TeV.107675.AlpgenJimmy_AUET2CTEQ6L1_ZtautauNp5	1.12	1.23	1.0
mc12_8TeV.109300.AlpgenJimmy_AUET2CTEQ6L1_ZeebbNp0	8.378	1.23	1.0
mc12_8TeV.109301.AlpgenJimmy_AUET2CTEQ6L1_ZeebbNp1	3.253	1.23	1.0
mc12_8TeV.109302.AlpgenJimmy_AUET2CTEQ6L1_ZeebbNp2	1.190	1.23	1.0
mc12_8TeV.109303.AlpgenJimmy_AUET2CTEQ6L1_ZeebbNp3	0.503	1.23	1.0
mc12_8TeV.109305.AlpgenJimmy_AUET2CTEQ6L1_ZmumubbNp0	8.374	1.23	1.0
mc12_8TeV.109306.AlpgenJimmy_AUET2CTEQ6L1_ZmumubbNp1	3.254	1.23	1.0
mc12_8TeV.109307.AlpgenJimmy_AUET2CTEQ6L1_ZmumubbNp2	1.181	1.23	1.0
mc12_8TeV.109308.AlpgenJimmy_AUET2CTEQ6L1_ZmumubbNp3	0.507	1.23	1.0
mc12_8TeV.109310.AlpgenJimmy_AUET2CTEQ6L1_ZtautaubbNp0	8.376	1.23	1.0
mc12_8TeV.109311.AlpgenJimmy_AUET2CTEQ6L1_ZtautaubbNp1	3.243	1.23	1.0
mc12_8TeV.109312.AlpgenJimmy_AUET2CTEQ6L1_ZtautaubbNp2	1.194	1.23	1.0
mc12_8TeV.109313.AlpgenJimmy_AUET2CTEQ6L1_ZtautaubbNp3	0.498	1.23	1.0
mc12_8TeV.126414.AlpgenJimmy_AUET2CTEQ6L1_ZeeccNp0	15.654	1.23	1.0
mc12_8TeV.126415.AlpgenJimmy_AUET2CTEQ6L1_ZeeccNp1	6.8946	1.23	1.0
mc12_8TeV.126416.AlpgenJimmy_AUET2CTEQ6L1_ZeeccNp2	2.9204	1.23	1.0
mc12_8TeV.126417.AlpgenJimmy_AUET2CTEQ6L1_ZeeccNp3	1.1411	1.23	1.0
mc12_8TeV.126418.AlpgenJimmy_AUET2CTEQ6L1_ZmumuccNp0	15.649	1.23	1.0
mc12_8TeV.126419.AlpgenJimmy_AUET2CTEQ6L1_ZmumuccNp1	6.8930	1.23	1.0
mc12_8TeV.126420.AlpgenJimmy_AUET2CTEQ6L1_ZmumuccNp2	2.9176	1.23	1.0
mc12_8TeV.126421.AlpgenJimmy_AUET2CTEQ6L1_ZmumuccNp3	1.1377	1.23	1.0
mc12_8TeV.117706.AlpgenJimmy_AUET2CTEQ6L1_ZtautauccNp0	15.652	1.23	1.0
mc12_8TeV.117707.AlpgenJimmy_AUET2CTEQ6L1_ZtautauccNp1	6.8979	1.23	1.0
mc12_8TeV.117708.AlpgenJimmy_AUET2CTEQ6L1_ZtautauccNp2	2.9100	1.23	1.0
mc12_8TeV.117709.AlpgenJimmy_AUET2CTEQ6L1_ZtautauccNp3	1.1340	1.23	1.0
mc12_8TeV.146830.AlpgenJimmy_Auto_AUET2CTEQ6L1_ZeeNp0Excl_Mll10to60	3480.	1.19	1.0
mc12_8TeV.146831.AlpgenJimmy_Auto_AUET2CTEQ6L1_ZeeNp1Excl_Mll10to60	110.	1.19	1.0
mc12_8TeV.146832.AlpgenJimmy_Auto_AUET2CTEQ6L1_ZeeNp2Excl_Mll10to60	52.3	1.19	1.0
mc12_8TeV.146833.AlpgenJimmy_Auto_AUET2CTEQ6L1_ZeeNp3Excl_Mll10to60	11.3	1.19	1.0
mc12_8TeV.146834.AlpgenJimmy_Auto_AUET2CTEQ6L1_ZeeNp4Excl_Mll10to60	2.59	1.19	1.0
mc12_8TeV.146835.AlpgenJimmy_Auto_AUET2CTEQ6L1_ZeeNp5Incl_Mll10to60	0.693	1.19	1.0
mc12_8TeV.146840.AlpgenJimmy_Auto_AUET2CTEQ6L1_ZmumuNp0Excl_Mll10to60	3480.	1.19	1.0
mc12_8TeV.146841.AlpgenJimmy_Auto_AUET2CTEQ6L1_ZmumuNp1Excl_Mll10to60	110.	1.19	1.0
mc12_8TeV.146842.AlpgenJimmy_Auto_AUET2CTEQ6L1_ZmumuNp2Excl_Mll10to60	52.3	1.19	1.0
mc12_8TeV.146843.AlpgenJimmy_Auto_AUET2CTEQ6L1_ZmumuNp3Excl_Mll10to60	11.3	1.19	1.0
mc12_8TeV.146844.AlpgenJimmy_Auto_AUET2CTEQ6L1_ZmumuNp4Excl_Mll10to60	2.59	1.19	1.0
mc12_8TeV.146845.AlpgenJimmy_Auto_AUET2CTEQ6L1_ZmumuNp5Incl_Mll10to60	0.693	1.19	1.0
mc12_8TeV.146850.AlpgenJimmy_Auto_AUET2CTEQ6L1_ZtautauNp0Excl_Mll10to60	3480.	1.19	1.0
mc12_8TeV.146851.AlpgenJimmy_Auto_AUET2CTEQ6L1_ZtautauNp1Excl_Mll10to60	110.	1.19	1.0
mc12_8TeV.146852.AlpgenJimmy_Auto_AUET2CTEQ6L1_ZtautauNp2Excl_Mll10to60	52.3	1.19	1.0
mc12_8TeV.146853.AlpgenJimmy_Auto_AUET2CTEQ6L1_ZtautauNp3Excl_Mll10to60	11.3	1.19	1.0
mc12_8TeV.146854.AlpgenJimmy_Auto_AUET3CTEQ6L1_ZtautauNp4Excl_Mll10to60	2.59	1.19	1.0
mc12_8TeV.146855.AlpgenJimmy_Auto_AUET2CTEQ6L1_ZtautauNp5Incl_Mll10to60	0.693	1.19	1.0

Table A.3: Z+jets Monte Carlo samples used in this thesis.

Sample Name	Cross Section [pb]	k-Factor	Filter Efficiency
mc12_8TeV.107680.AlpgenJimmy_AUET2CTEQ6L1_WenuNp0	8037.1	1.18	1.0
mc12_8TeV.107681.AlpgenJimmy_AUET2CTEQ6L1_WenuNp1	1579.2	1.18	1.0
mc12_8TeV.107682.AlpgenJimmy_AUET2CTEQ6L1_WenuNp2	477.2	1.18	1.0
mc12_8TeV.107683.AlpgenJimmy_AUET2CTEQ6L1_WenuNp3	133.9	1.18	1.0
mc12_8TeV.107684.AlpgenJimmy_AUET2CTEQ6L1_WenuNp4	35.62	1.18	1.0
mc12_8TeV.107685.AlpgenJimmy_AUET2CTEQ6L1_WenuNp5	10.55	1.18	1.0
mc12_8TeV.107690.AlpgenJimmy_AUET2CTEQ6L1_WmunuNp0	8040.0	1.18	1.0
mc12_8TeV.107691.AlpgenJimmy_AUET2CTEQ6L1_WmunuNp1	1580.3	1.18	1.0
mc12_8TeV.107692.AlpgenJimmy_AUET2CTEQ6L1_WmunuNp2	477.5	1.18	1.0
mc12_8TeV.107693.AlpgenJimmy_AUET2CTEQ6L1_WmunuNp3	133.9	1.18	1.0
mc12_8TeV.107694.AlpgenJimmy_AUET2CTEQ6L1_WmunuNp4	35.64	1.18	1.0
mc12_8TeV.107695.AlpgenJimmy_AUET2CTEQ6L1_WmunuNp5	10.57	1.18	1.0
mc12_8TeV.107700.AlpgenJimmy_AUET2CTEQ6L1_WtaunuNp0	8035.8	1.18	1.0
mc12_8TeV.107701.AlpgenJimmy_AUET2CTEQ6L1_WtaunuNp1	1579.8	1.18	1.0
mc12_8TeV.107702.AlpgenJimmy_AUET2CTEQ6L1_WtaunuNp2	477.6	1.18	1.0
mc12_8TeV.107703.AlpgenJimmy_AUET2CTEQ6L1_WtaunuNp3	133.8	1.18	1.0
mc12_8TeV.107704.AlpgenJimmy_AUET2CTEQ6L1_WtaunuNp4	35.6	1.18	1.0
mc12_8TeV.107705.AlpgenJimmy_AUET2CTEQ6L1_WtaunuNp5	10.5	1.18	1.0
mc12_8TeV.117284.AlpgenJimmy_AUET2CTEQ6L1_WccNp0	150.2	1.18	1.0
mc12_8TeV.117285.AlpgenJimmy_AUET2CTEQ6L1_WccNp1	132.7	1.18	1.0
mc12_8TeV.117286.AlpgenJimmy_AUET2CTEQ6L1_WccNp2	71.8	1.18	1.0
mc12_8TeV.117287.AlpgenJimmy_AUET2CTEQ6L1_WccNp3	30.3	1.18	1.0
mc12_8TeV.117293.AlpgenJimmy_AUET2CTEQ6L1_WcNp0	807.9	1.18	1.0
mc12_8TeV.117294.AlpgenJimmy_AUET2CTEQ6L1_WcNp1	267.6	1.18	1.0
mc12_8TeV.117295.AlpgenJimmy_AUET2CTEQ6L1_WcNp2	69.8	1.18	1.0
mc12_8TeV.117296.AlpgenJimmy_AUET2CTEQ6L1_WcNp3	20.6	1.18	1.0
mc12_8TeV.117297.AlpgenJimmy_AUET2CTEQ6L1_WcNp4	4.3	1.18	1.0
mc12_8TeV.107280.AlpgenJimmy_AUET2CTEQ6L1_WbbNp0	55.7	1.18	1.0
mc12_8TeV.107281.AlpgenJimmy_AUET2CTEQ6L1_WbbNp1	45.2	1.18	1.0
mc12_8TeV.107282.AlpgenJimmy_AUET2CTEQ6L1_WbbNp2	23.3	1.18	1.0
mc12_8TeV.107283.AlpgenJimmy_AUET2CTEQ6L1_WbbNp3	11.1	1.18	1.0

Table A.4: W+jets Monte Carlo samples used in this thesis.

Sample Name	Cross Section [pb]	k-Factor	Filter Efficiency
mc12_8TeV.146436.AlpgenJimmy_AUET2CTEQ6L1_WgammaNp0_LeptonPhotonFilter	230.	1.15	0.314
mc12_8TeV.146437.AlpgenJimmy_AUET2CTEQ6L1_WgammaNp1_LeptonPhotonFilter	59.5	1.15	0.449
mc12_8TeV.146438.AlpgenJimmy_AUET2CTEQ6L1_WgammaNp2_LeptonPhotonFilter	21.4	1.15	0.545
mc12_8TeV.146439.AlpgenJimmy_AUET2CTEQ6L1_WgammaNp3_LeptonPhotonFilter	7.12	1.15	0.630
mc12_8TeV.146434.AlpgenJimmy_AUET2CTEQ6L1_WgammaNp4	2.12	1.15	1.0
mc12_8TeV.146435.AlpgenJimmy_AUET2CTEQ6L1_WgammaNp5	0.467	1.15	1.0
mc12_8TeV.185304.Sherpa_CT10_Wenugamma2jetVBS.merge	0.4496	1.0	1.0
mc12_8TeV.185305.Sherpa_CT10_Wmunugamma2jetVBS.merge	0.4496	1.0	1.0
mc12_8TeV.185306.Sherpa_CT10_Wtaunugamma2jetVBS.merge	0.4496	1.0	1.0

Table A.5: $W\gamma$ Monte Carlo samples used in this thesis.

APPENDIX B

Non-prompt Background Estimation

B.1 EF_mu24_tight Trigger Efficiency

The di-jet sample is actually selected as jet+lepton sample with a single lepton trigger. For muon fake factor measurement, the sample is required to have trigger EF_mu24_tight fired and the trigger efficiency with respect to the tight and loose muons are not necessarily the same due to the difference in the isolation and impact parameter cuts. Possible biase could have been introducted from this difference in the efficiency. The trigger efficiencies are measured for the two different muon definitions.

1. EF_mu24_tight with respect to the tight muon: A usual tag-and-probe method is used. Two and only two tight muons with $p_{\mathrm{T}} > 25$ GeV are required to be present in the event, with dimuon invariant mass to be within a Z mass window of 10 GeV. The tag muon is required to be matched to the un-prescaled EF_mu24i_tight or EF_mu36_tight trigger. The probe muon is then looked at to see whether it can be matched to trigger EF_mu24_tight. The trigger efficiency is shown in Figure B.1 as a function of the muon p_{T}.

2. EF_mu24_tight with respect to the loose muon: A modified tag-and-probe method is used. The event selection is the same as for the tight+loose sample but without the $E_{\mathrm{T}}^{\mathrm{miss}}$ cut and the cuts after. One tight lepton and one loose lepton are present in the event with the same electric charge. The tight lepton in the event is required to be matched to the un-prescaled nominal trigger and the loose muon is checked to see whether it matches to EF_mu24_tight. The small prompt contributions other than W+jets and top are subtracted using MC. The trigger efficiency is shown in Figure B.1 as a function of the muon p_{T}.

By requiring the probe muon to be matched to the trigger `EF_mu24_tight`, we have pre-scaled the data sample by a factor ∼10, which results in a sample of 2.7 fb^{-1}.

The trigger efficiency with respect to the loose muon is relatively lower than for tight muons. The ratio of the trigger efficiencies with respect to the two muon definitions is shown in Figure B.2. This ratio would be applied to the measured muon fake factor as a correction for the trigger bias.

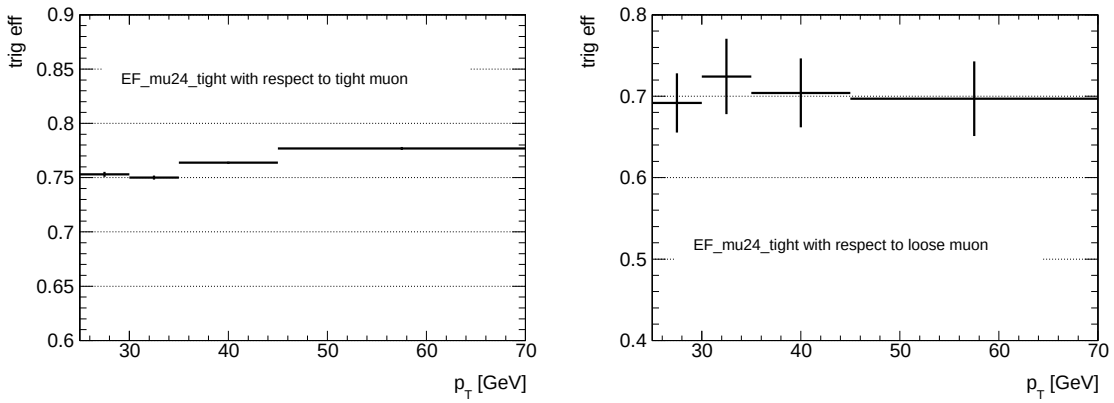

Figure B.1: The `EF_mu24_tight` trigger efficiency with respect to the tight (left) and loose (right) muon definitons.

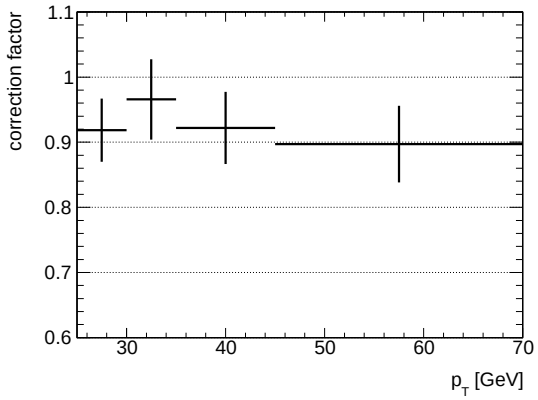

Figure B.2: The ratio between the `EF_mu24_tight` trigger efficiencies with respect to the loose and tight muon definitons.

B.2 Comparison Between Di-jet and Z+jets Sample

In this section, the effects of the underlying jet p_{T} on the non-prompt lepton isolation are investigated, by comparing di-jet data sample and Z+jets data sample. Reweighting the jet p_{T} distribution in the di-jet sample is found to be effective in resolving the difference between the two samples.

The event selection of the di-jet sample is the same as described in Section 4.6.2.1. The Z+jets sample is selected with two high quality tight leptons of the same flavor and opposite electric charge. The invariant mass of the two leptons is required to be within the Z mass window $|m_{\ell\ell} - m_Z| < 15$ GeV and these two leptons form a Z candidate. To suppress WZ events, the $E_{\mathrm{T}}^{\mathrm{miss}}$ is required to be below 40 GeV. Events with more than three nominal leptons are rejected to suppress the ZZ contribution. A third lepton is required to be present in the event passing the loose lepton definition and back-to-back with the Z candidte with $\Delta\phi > 2.5$.

Figure B.3 shows the comparison of the calorimeter isolation variable $E_{\mathrm{T}}^{\mathrm{cone30}}/p_{\mathrm{T}}$, and track isolation variable $p_{\mathrm{T}}^{\mathrm{cone30}}/p_{\mathrm{T}}$ in di-jet, Z+jets and the tight+loose sample corresponding to the events passing the $N_{jet} \geq 2$ cut in our nominal selections (see Section 4.4).

Assuming the p_{T} balance in the transverse plane, the tagging jet p_{T} and the Z p_{T} can be used as representitives of the underlying jet p_{T} in di-jet sample and Z+jets sample respectively. The underlying jets in the Z+jets sample are found to have similar p_{T} distribution to the tight+loose sample while the difference between the di-jet sample and the tight+loose sample is found to be larger, even though there are no obvious reasons why underlying jets in the Z+jets sample should have similar kinematics as underlying jets in the tight+loose sample. However, Z+jets samples often have limited statistics and can only be used to measure the average fake factor and can not measure the dependence on the fake lepton p_{T}.

It is found that if we reweight the tagging jet p_{T} distribution in the di-jet sample to the Z boson p_{T} distribution in the Z+jets sample, the differences in both the calorimeter and track isolation distributions between these two samples can be largely reduced, as shown in Fig. B.4.

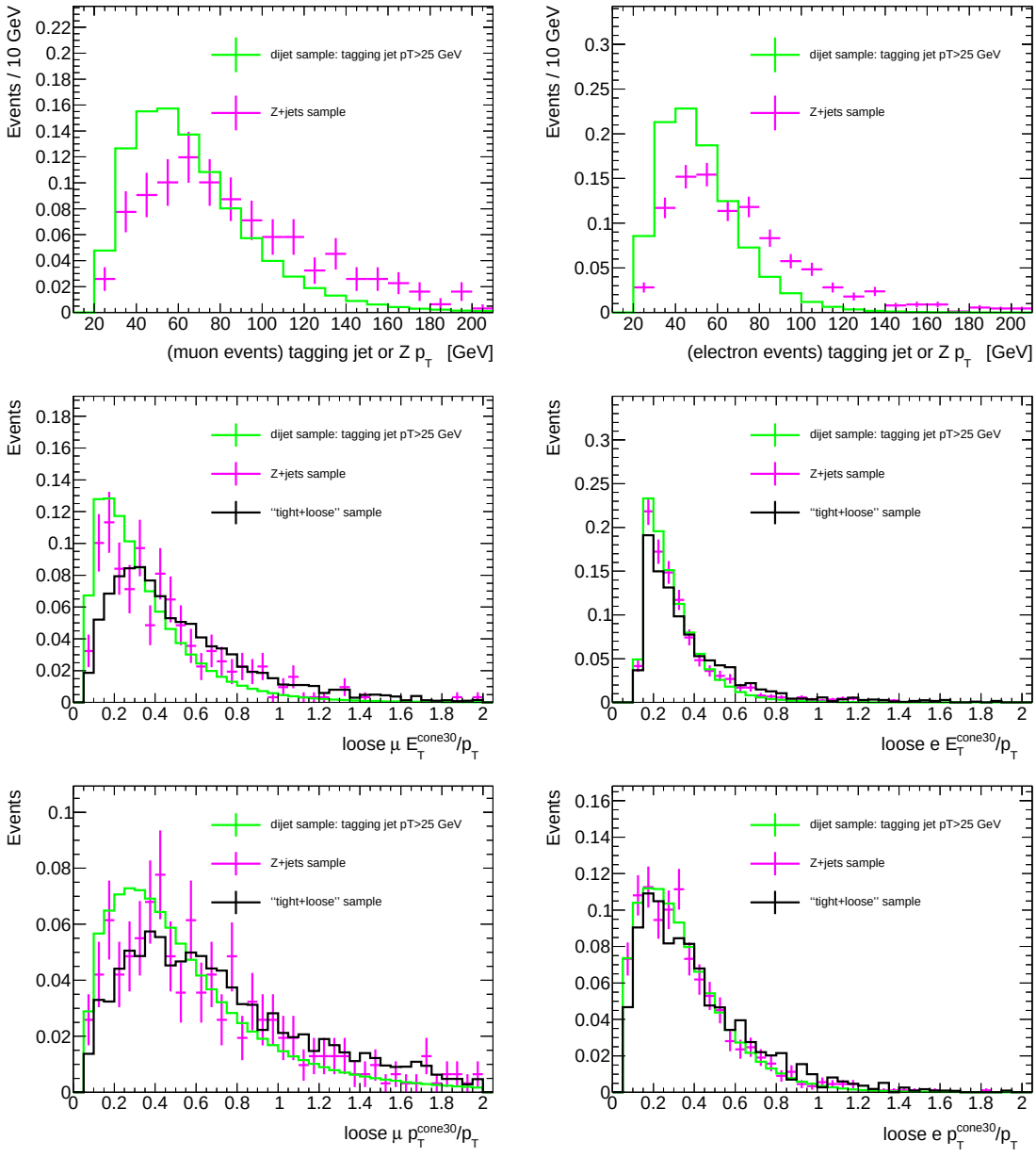

Figure B.3: From top to bottom: the tagging jet p_{T} and Z p_{T}, the $E_{\mathrm{T}}^{\mathrm{cone30}}/p_{\mathrm{T}}$ and $p_{\mathrm{T}}^{\mathrm{cone30}}/p_{\mathrm{T}}$ for the di-jet, Z+jets and tight+loose sample. The plots for muons are on the left and the electron on the right. The tight+loose sample is after the $N_{jet} \geq 2$ cut as in the nominal analysis.

B.3 Prompt Background in Di-jet Sample

In the selected di-jet sample, the contributions from W+jets and Z+jets processes are estimated using MC simulation and subtracted. A control region is used for

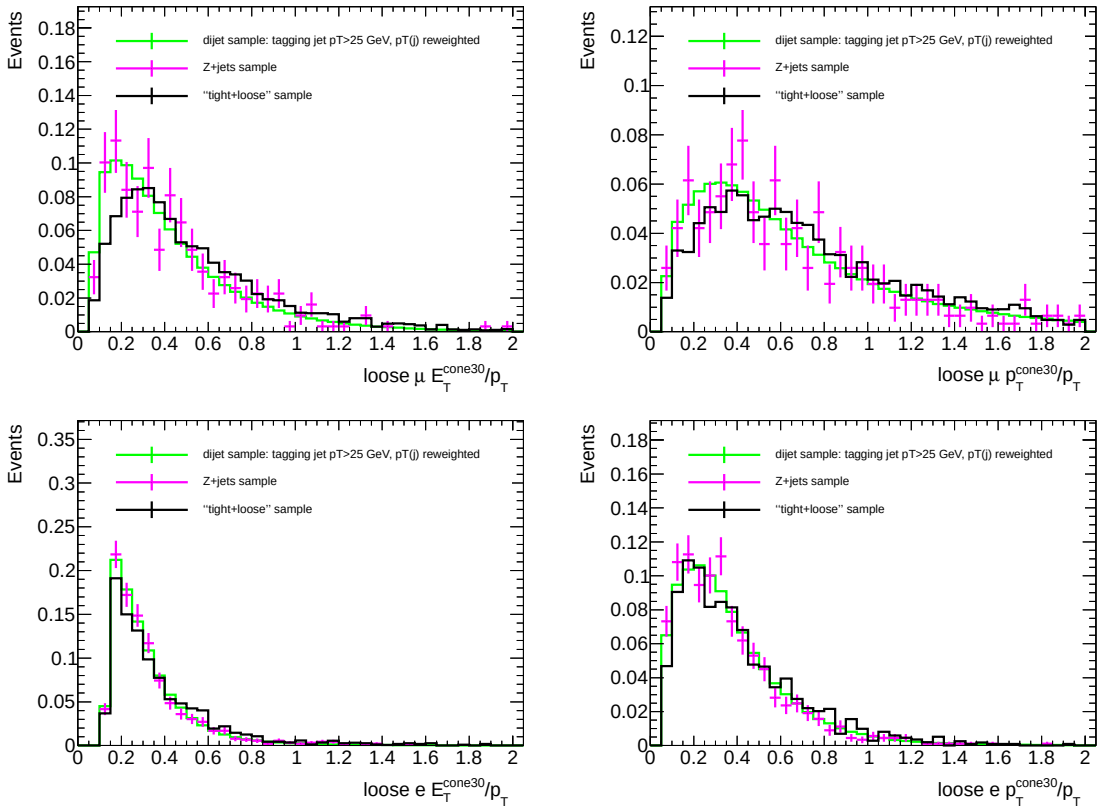

Figure B.4: The loose lepton $E_{\mathrm{T}}^{\mathrm{cone30}}/p_{\mathrm{T}}$ and $p_{\mathrm{T}}^{\mathrm{cone30}}/p_{\mathrm{T}}$ distributions for the di-jet, Z+jets and tight+loose sample after the tagging jet p_{T} distribution in the di-jet sample is reweighted to the Z boson p_{T} distribution in the Z+jets sample. These plots indicate that it is important to have the right jet kinematics for the fake factor measurement.

checking the MC simulation of these two processes. The prompt control region is defined as passing all other di-jet selections but without the $m_{\mathrm{T}}(\ell, E_{\mathrm{T}}^{\mathrm{miss}})$ cut and further require $\Delta\phi(\ell, j) < 2.0$. The $\Delta\phi(\ell, j)$ distribution of jet+tight lepton events is shown in Figure B.5 after all other selection cuts but the $m_{\mathrm{T}}(\ell, j)$ cut.

The observed and expected numbers of events in the control region are summarized in Table B.1.

The $m_{\mathrm{T}}(\ell, E_{\mathrm{T}}^{\mathrm{miss}})$ distribution after all other selections, including the $\Delta\phi(\ell, j)$ >2.8 cut, is shown in Figure B.6. The $\Delta\phi(\ell, j)$ distribution after all other selections, including the m_{T} <40 GeV cut, is shown in Figure B.7. The tight lepton p_{T} distribution after all selection cuts is shown in Figure B.8. It can be seen from these plots that the discrepancy between data and MC in the prompt process dominated region can be covered by the 4% and 12% uncertainty assigned to the electron and

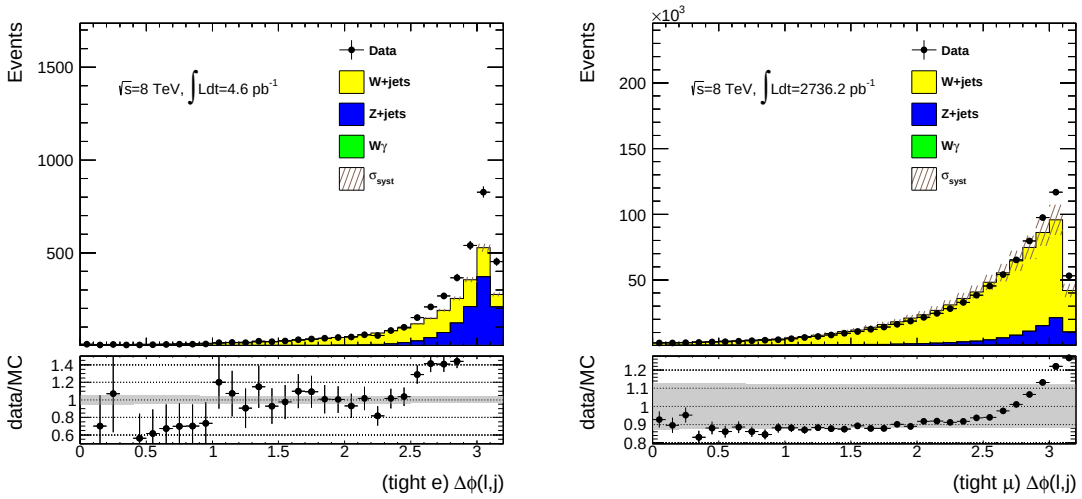

Figure B.5: The $\Delta\phi(\ell, j)$ distribution of jet+tight lepton events after all di-jet selections but the $m_{\mathrm{T}}(\ell, E_{\mathrm{T}}^{\mathrm{miss}})$ <40 GeV cut. The region $\Delta\phi < 2.0$ is defined as the control region for W+jets and Z+jets contribution. The error band corresponds to a 4% uncertainty for jet+tight electron channel and 12% uncertainty for jet+tight muon channel.

channel	Data	MC	(Data-MC)/MC
tight e	329	340.5±1.4 (stat.)	-0.034
tight μ	137622	155773.9±673.8 (stat.)	-0.117

Table B.1: The observed and expected numbers of events in the prompt process control region in di-jet sample. A 4% and 12% uncertainty on the overall W+jets and Z+jets MC prediction will be applied for the electron and muon channel respectively.

muon channel respectively.

B.4 Residual Flavor Dependence

After the jet p_{T} reweighting, the residual flavor dependence of the fake factors is checked by comparing the di-jet, W+jets and $t\bar{t}$ MC samples. The di-jet MC events are selected requiring one jet and one non-prompt lepton. The W+jets and $t\bar{t}$ MC events are selected with one prompt lepton and one non-prompt lepton instead, both with $p_{\mathrm{T}} > 25$ GeV. Prompt leptons are those from W decay and non-prompt leptons from hadron decay by looking at the truth information. The non-prompt leptons are then looked at to see whether it passes the tight or loose definition for

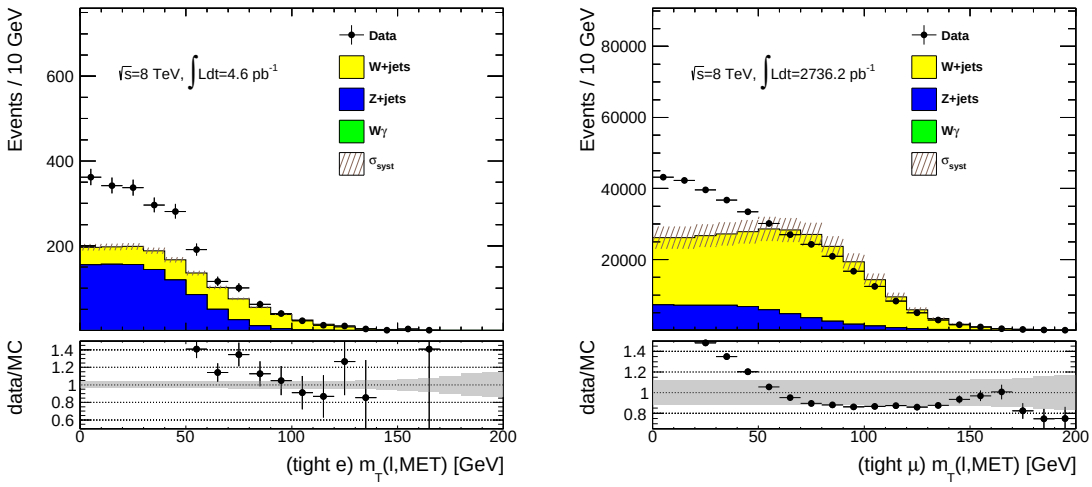

Figure B.6: The $m_{\mathrm{T}}(\ell, E_{\mathrm{T}}^{\mathrm{miss}})$ distribution of the jet+tight lepton events after all other selection cuts.

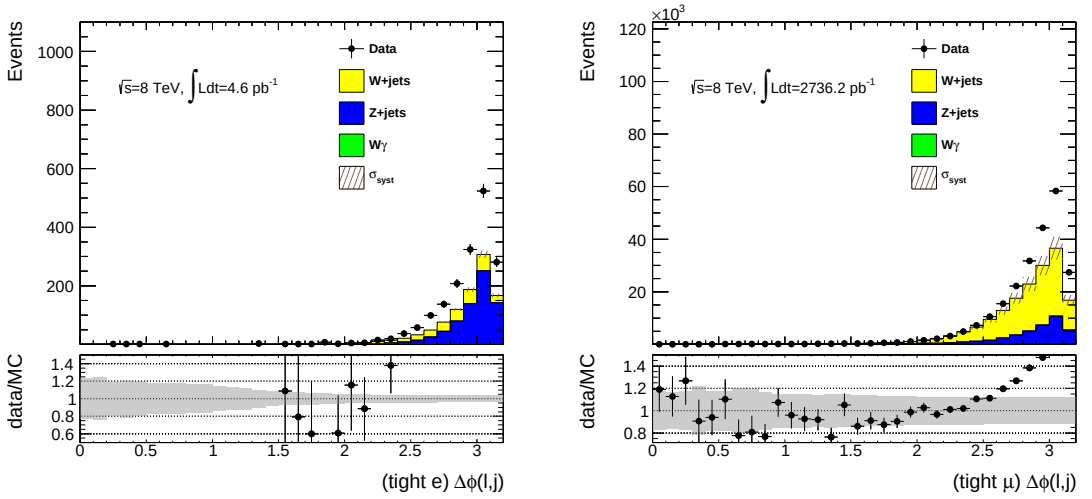

Figure B.7: The $m_{\mathrm{T}}(\ell, E_{\mathrm{T}}^{\mathrm{miss}})$ distribution of the jet+tight lepton events after all other selection cuts.

the fake factor calculation. Truth underlying jets are defined as the vector sum of all `AntiKt4Truth` jets, neutrinos and muons in the cone of $\Delta R = 0.3$ around the non-prompt lepton. (The `AntiKt4Truth` jets cluster all final state objects other than neutrinos and muons.) The truth underlying jet p_{T} distribution is shown in Figure B.9. The di-jet sample has soft underlying jet p_{T} spectrum compared to the other two. For W+jets and $t\bar{t}$ MC, the jets producing non-prompt electrons have very different p_{T} spectra, while the jets which decay to muons have similar p_{T} distributions. The fake factors without any underlying jet p_{T} reweighting are shown in Figure B.10.

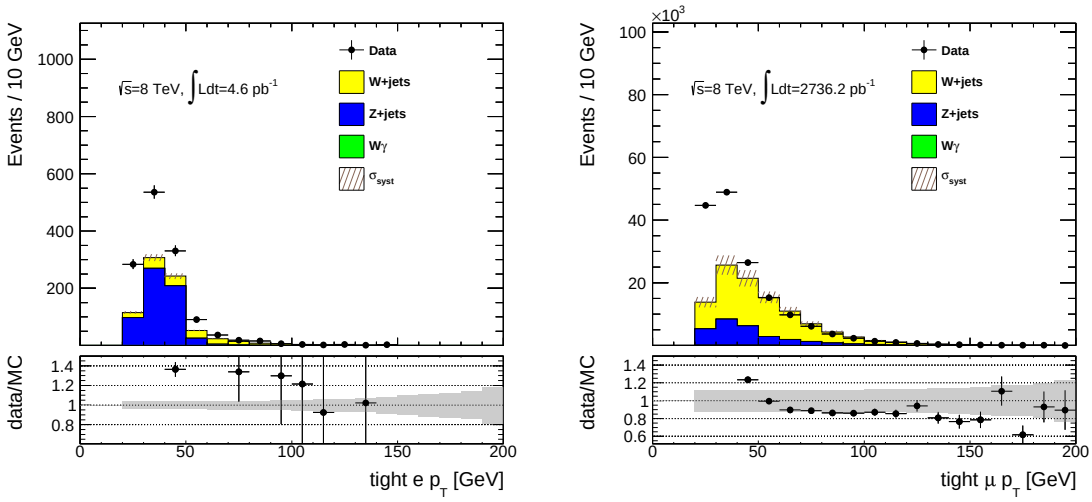

Figure B.8: The $m_{\mathrm{T}}(\ell, E_{\mathrm{T}}^{\mathrm{miss}})$ distribution of the jet+tight lepton events after all other selection cuts.

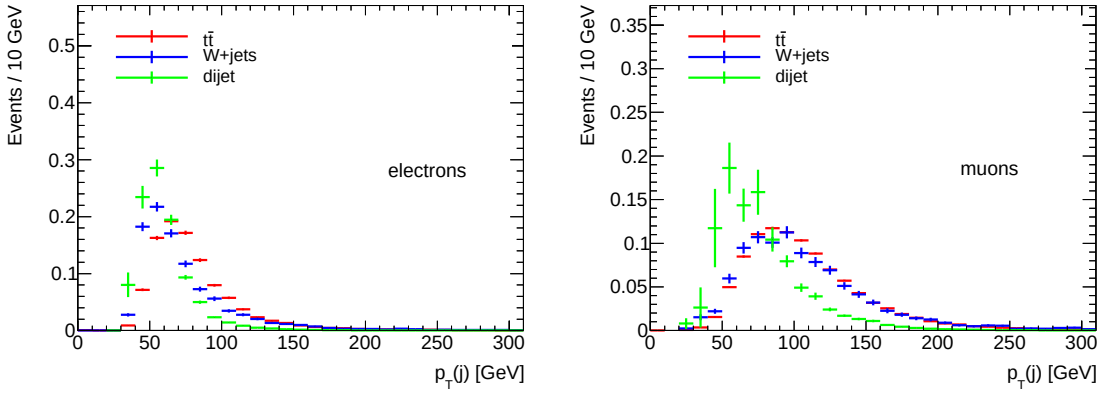

Figure B.9: The truth underlying jet p_{T} distributions for non-prompt electrons and muons.

As a closure check, we reweight the underlying jet p_{T} distribution of the di-jet MC sample to that of the W+jets or $t\bar{t}$ MC sample and require the underlying jet p_{T} to be larger than 40 (35) GeV for muon (electron) events in the di-jet sample and compare the fake factors between different MC samples. The fake factors are shown in Figure B.11 and B.12. The large statistical uncertainties associated with these fake factors make it difficult to reach any definitive conclusions.

The averaged truth underlying jet p_{T} versus the lepton $p_{\mathrm{T}} + E_{\mathrm{T}}^{\mathrm{cone30}}$ is shown in Figure B.13. The mapping slope is different for di-jet, W+jets amd $t\bar{t}$ MC samples, indicating the flavor or sample dependence. For electrons, the difference is small while for muons the difference is slightly larger. Compared to the mapping

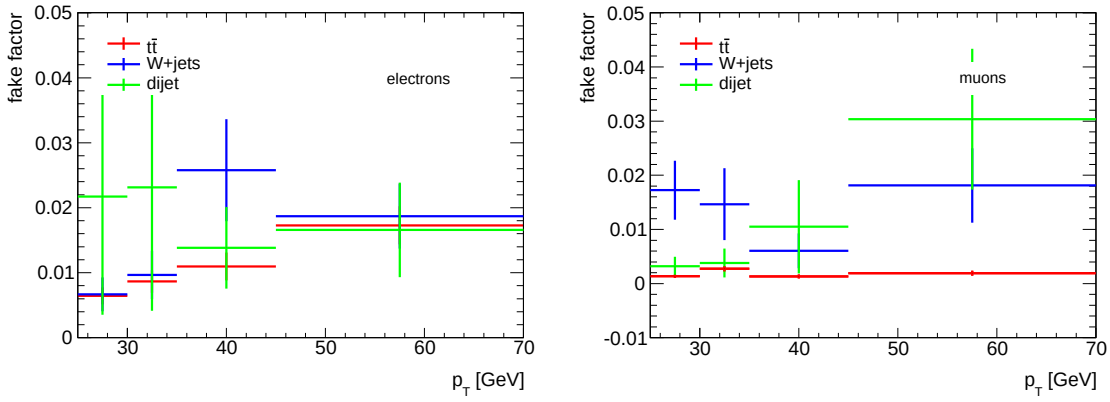

Figure B.10: The fake factors using the MC samples without any jet p_{T} reweighting.

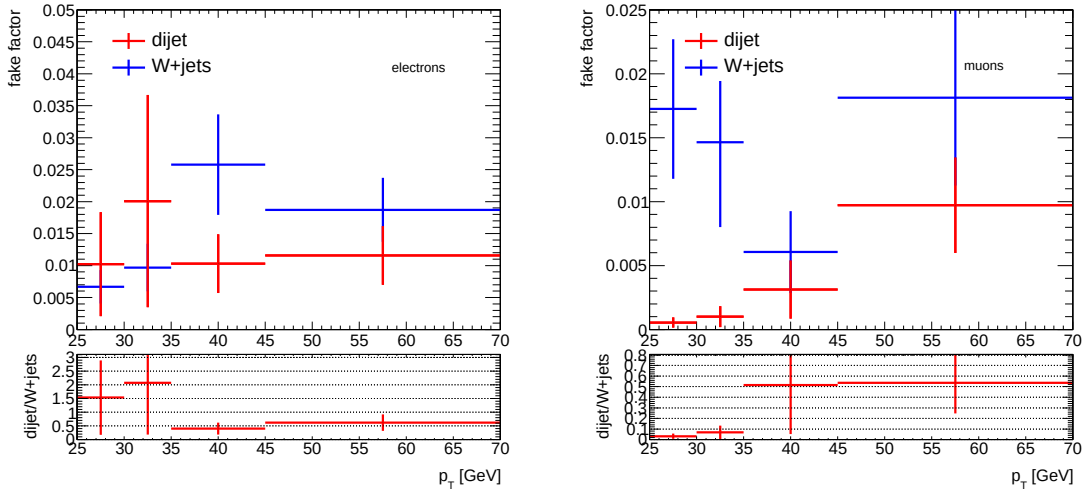

Figure B.11: The fake factors measured using the di-jet and W+jets MC samples. The truth underlying jet p_{T} distribution of the di-jet sample has been reweighted to that of the W+jets sample for electron events and muon events respectively. In the di-jet sample, the jet p_{T} threshold has been required to be larger than 40 (35) GeV for muon (electron) events to further suppress the low p_{T} jet events. The overall fake factor as a flat number in the di-jet sample is 0.012 ± 0.005 (stat.) for electrons and 0.003 ± 0.001 for muons. The overall fake factor as a flat number in the W+jets sample is 0.014 ± 0.002 (stat.) for electrons and 0.014 ± 0.003 for muons.

we have obtained with di-jet data sample, shown in Figure 4.15, a 15% variation is enough to cover the differences seen between all MC samples. Thus for the systematic uncertainty due to the residual flavor/sample dependence, the mapping slope is varied up and down by 15%. A comparison of the truth underlying jet p_{T} distribution and the derived underlying jet p_{T} distribution using different mapping slopes is shown in Figure B.14. The derived underlying jet p_{T} distribution is

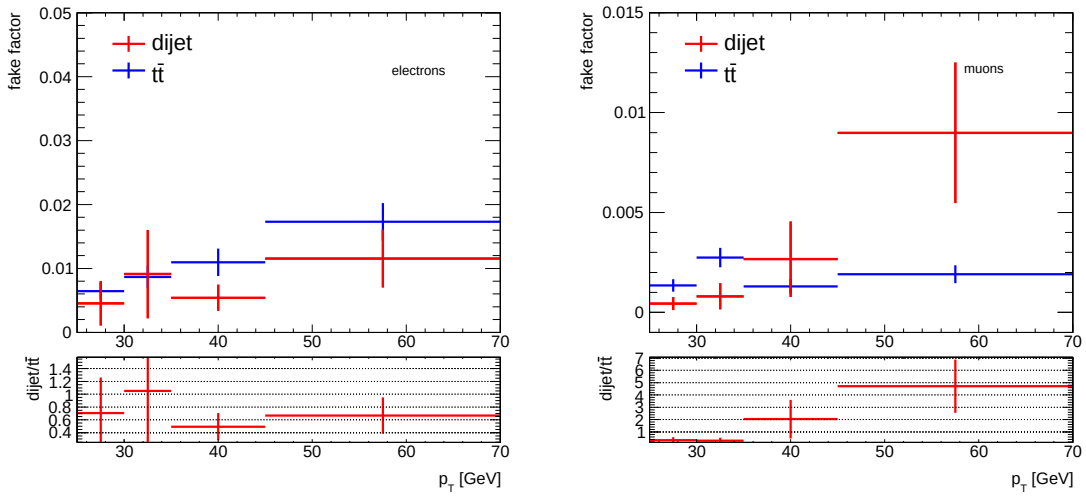

Figure B.12: The fake factors measured using the di-jet and $t\bar{t}$ MC samples. The truth underlying jet p_{T} distribution of the di-jet sample has been reweighted to that of the $t\bar{t}$ sample for electron events and muon events respectively. In the di-jet sample, the jet p_{T} threshold has been required to be larger than 40 (35) GeV for muon (electron) events to further suppress the low p_{T} jet events. The overall fake factor as a flat number in the di-jet sample is 0.007 ± 0.002 (stat.) for electrons and 0.003 ± 0.001 for muons. The overall fake factor as a flat number in the $t\bar{t}$ sample is 0.010 ± 0.001 (stat.) for electrons and 0.0018 ± 0.0002 for muons.

consistent with the truth underlying jet p_{T} distribution. When the slope is varied by 15%, the variations of the derived underlying jet p_{T} distribution sandwich the truth underlying jet p_{T} distribution.

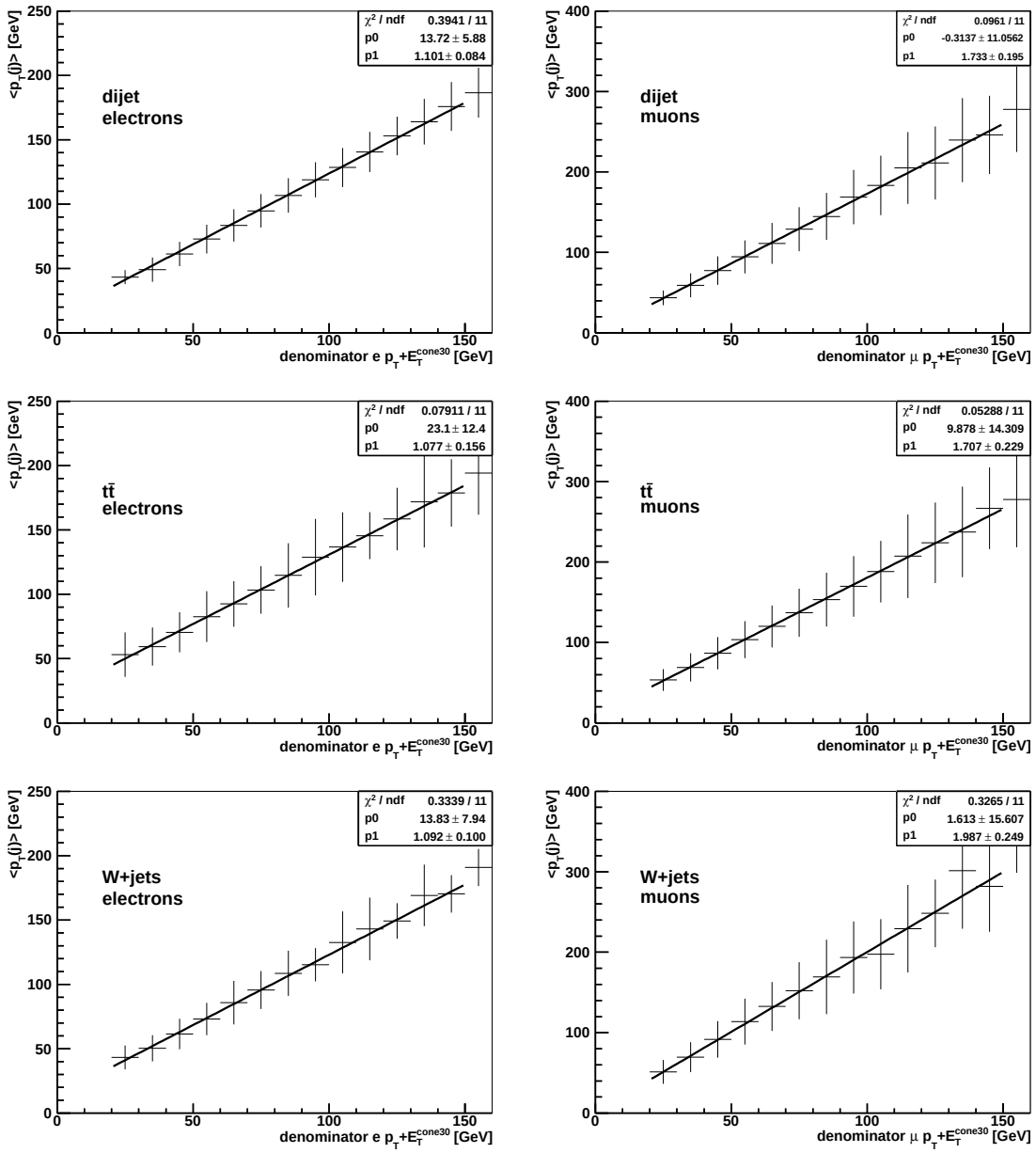

Figure B.13: The averaged truth underlying jet p_{T} versus the lepton $p_{\mathrm{T}} + E_{\mathrm{T}}^{\mathrm{cone30}}$.

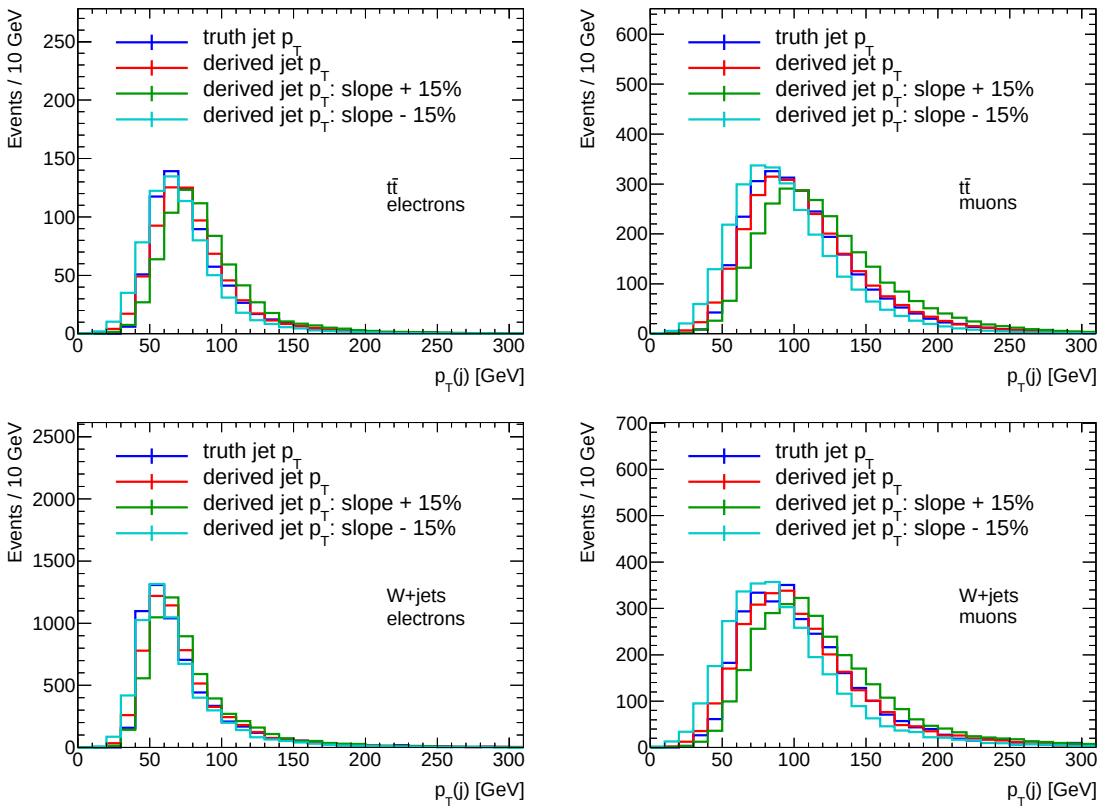

Figure B.14: The truth underlying jet p_{T} distribution and the derived underlying jet p_{T} distribution using the mapping with different slopes.

BIBLIOGRAPHY

[1] ATLAS Collaboration, *Observation of a new particle in the search for the Standard Model Higgs boson with the ATLAS detector at the LHC*, Phys. Lett. **B716** (2012) 1–29, arXiv:1207.7214 [hep-ex].

[2] CMS Collaboration, *Observation of a new boson at a mass of 125 GeV with the CMS experiment at the LHC*, Phys. Lett. **B716** (2012) 30–61, arXiv:1207.7235 [hep-ex].

[3] ATLAS Collaboration, *Evidence for the spin-0 nature of the Higgs boson using ATLAS data*, Phys. Lett. **B726** (2013) 120–144, arXiv:1307.1432 [hep-ex].

[4] CMS Collaboration, *Study of the Mass and Spin-Parity of the Higgs Boson Candidate Via Its Decays to Z Boson Pairs*, Phys. Rev. Lett. **110** (2013) 081803, arXiv:1212.6639 [hep-ex].

[5] M. J. G. Veltman, *Second Threshold in Weak Interactions*, Acta Phys. Polon. **B8** (1977) 475.

[6] B. W. Lee, C. Quigg, and H. B. Thacker, *The Strength of Weak Interactions at Very High-Energies and the Higgs Boson Mass*, Phys. Rev. Lett. **38** (1977) 883.

[7] B. W. Lee, C. Quigg, and H. B. Thacker, *Weak Interactions at Very High-Energies: The Role of the Higgs Boson Mass*, Phys. Rev. **D16** (1977) 1519.

[8] DELPHI Collaboration, *Measurement of the $e^+e^- \to W^+W^-\gamma$ Cross-section and Limits on Anomalous Quartic Gauge Couplings with DELPHI*, Eur. Phys. J. **C31** (2003), arXiv:hep-ex/0311004.

[9] OPAL Collaboration, *Constraints on Anomalous Quartic Gauge Boson Couplings from $\nu\bar{\nu}\gamma\gamma$ and $q\bar{q}\gamma\gamma$ Events at LEP2*, Phys. Rev. **D70** (2004) 032005, arXiv:hep-ex/0402021.

[10] L3 Collaboration, *Study of the $W^+W^-\gamma$ process and limits on anomalous quartic gauge boson couplings at LEP*, Phys. Lett. **B527** (2002) 29.

[11] CMS Collaboration, *A search for $WW\gamma$ and $WZ\gamma$ production and constraints on anomalous quartic gauge couplings in pp collisions at $\sqrt{s} = 8$ TeV*, Phys. Rev. **D90** (2014) 032008, arXiv:1404.4619 [hep-ex].

[12] CMS Collaboration, *Study of exclusive two-photon production of W^+W^- in pp collisions at $\sqrt{s} = 7$ TeV and constraints on anomalous quartic gauge couplings*, JHEP **07** (2013) 116, arXiv:1305.5596 [hep-ex].

[13] K.A. Olive *et al.* (Particle Data Group), *Review of Particle Physics*, Chin. Phys. **C38** (2014) 090001.

[14] P. Langacker, *The Standard Model and Beyond*,.

[15] F. Englert and R. Brout, *Broken Symmetry and the Mass of Gauge Vector Mesons*, Phys. Rev. Lett. **13** (1964) 321.

[16] P. W. Higgs, *Broken Symmetries and the Masses of Gauge Bosons*, Phys. Rev. Lett. **13** (1964) 508.

[17] G. S. Guralnik, C. R. Hagen, and T. W. B. Kibble, *Global Conservation Laws and Massless Particles*, Phys. Rev. Lett. **13** (1964) 585.

[18] J. Chang, K. Cheung, C.-T. Lu, and T.-C. Yuan, *WW scattering in the era of post-Higgs-boson discovery*, Phys. Rev. **D87** (2013) 093005.

[19] K. Cheung, C.-W. Chiang, and T.-C. Yuan, *Partially Strong WW Scattering*, Phys. Rev. **D78** (2008) 051701.

[20] S. Chang, S. K. Kang, J.-P. Lee, Y. K. Lee, S. C. Park, and J. Song, *Comprehensive study of two Higgs doublet model in light of the new boson with mass around 125 GeV*, 1210.3439 [hep-ph].

[21] C.-Y. Chen and D. Dawson, *Exploring Two Higgs Doublet Models Through Higgs Production*, Phys. Rev. **D87** (2013) 055016, arXiv:1301.0309 [hep-ph].

[22] A. Celis, V. Ilisie, and A. Pich, *LHC constraints on two-Higgs doublet models*, JHEP **07** (2013) 053, arXiv:1302.4022 [hep-ph].

[23] G. Wu and T. Appelquist, *The Electroweak Chiral Lagrangian and New Precision Measurements*, Phys. Rev. **D48** (1993) 3235–3241, arXiv:hep-ph/9304240.

[24] A. Alboteanu, W. Kilian, and J. Reuter, *Resonances and Unitarity in Weak Boson Scattering at the LHC*, JHEP **0811** (2008) 010, arXiv:0806.4145 [hep-ph].

[25] A. Alboteanu, W. Kilian, and J. Reuter, *Resonances and Unitarity in Weak Boson Scattering at the LHC*, JHEP **0811** (2008) 010, arXiv:0806.4145 [hep-ph].

[26] S. Chung, J. Brose, R. Hackmann, E. Klempt, S. Spanier, and C. Strassburger, *Partial wave analysis in K-matrix formalism*, Annalen der Physik **4** (1995) 404–430.

[27] M. S. Chanowitz, *Quantum corrections from nonresonant WW scattering*, Phys. Rept. **320** (1999) 139–146, arXiv:hep-ph/9903522.

[28] L. Evans and P. Bryant, *LHC Machine*, JINST **3** (2008) S08001.

[29] ATLAS Collaboration, *The ATLAS Experiment at the CERN Large Hadron Collider*, JINST **3** (2008) S08003.

[30] CMS Collaboration, *The CMS experiment at the CERN LHC*, JINST **3** (2008) S08004.

[31] LHCb Collaboration, *The LHCb Detector at the LHC*, JINST **3** (2008) S08005.

[32] ALICE Collaboration, *The ALICE experiment at the CERN LHC*, JINST **3** (2008) S08002.

[33] ATLAS Collaboration, *Readiness of the ATLAS liquid argon calorimeter for LHC collisions*, Eur. Phys. J. **C70** (2010) 723–753.

[34] ATLAS Collaboration, *A measurement of the ATLAS muon reconstruction and trigger efficiency using J/ψ decays*, ATLAS-CONF-2011-021. http://cds.cern.ch/record/1336750.

[35] ATLAS Collaboration, *Performance of the ATLAS Trigger System in 2010*, Eur. Phys. J. **C72** (2012) 1849, arXiv:1110.1530 [hep-ex].

[36] W. Lampl, S. Laplace, D. Lelas, P. Loch, H. Ma, S. Menke, S. Rajagopalan, D. Rousseau, S. Snyder, and G. Unal, *Calorimeter Clustering Algorithms: Description and Performance*, ATL-LARG-PUB-2008-002. https://cdsweb.cern.ch/record/1099735.

[37] ATLAS Collaboration, *Electron and photon energy calibration with the ATLAS detector using LHC Run 1 data*, Eur. Phys. J. **C74** (2014) 3071, arXiv:1407.5063 [hep-ex].

[38] ATLAS Collaboration, *Electron and photon energy calibration with the ATLAS detector using LHC Run 1 data*, Eur. Phys. J. **C74** (2014) 3071, arXiv:1407.5063 [hep-ex].

[39] ATLAS Collaboration, *Electron efficiency measurements with the ATLAS detector using the 2012 LHC proton-proton collision data*, ATLAS-CONF-2014-032. https://cds.cern.ch/record/1706245.

[40] S. Hassani, L. Chevalier, E. Lançon, J.-F. Laporte, R. Nicolaidou, and A. Ouraou, *A muon identification and combined reconstruction procedure for the ATLAS de-
tector at the LHC using the (MUONBOY, STACO, MuTag) reconstruction packages*, Nuclear Instruments and Methods in Physics Research Section A **572** (2007) 77–79.

[41] T. Lagouri, D. Adams, K. Assamagan, M. Biglietti, G. Carlina, G. Cataldi, F. Conventi, A. Farilla, Y. Fisyak, S. Goldfarb, E. Gorini, K. Mair, L. Merola, A. Nairz, A. Poppleton, M. Primavera, S. Rosati, J. Shank, S. Spagnolo, L. Spogli, G. Stavropoulos, M. Verducci, and T. Wenaus, *A muon identification and combined reconstruction procedure for the ATLAS detector at the LHC at CERN*, Nuclear Science, IEEE Transactions **51** (2004) 3030–3033.

[42] ATLAS Collaboration, *Measurement of the muon reconstruction performance of the ATLAS detector using 2011 and 2012 LHC proton-proton collision data*, arXiv:1407.3935 [hep-ex].

[43] M. Cacciari, G. P. Salam, and G. Soyez, *The anti-k_t jet clustering algorithm*, JHEP **0804** (2008) 063, arXiv:0802.1189.

[44] ATLAS Collaboration, *Jet energy measurement and its systematic uncertainty in proton-proton collisions at $\sqrt{s} = 7$ TeV with the ATLAS detector*, arXiv:1406.0076 [hep-ex].

[45] ATLAS Collaboration, *Jet energy resolution in proton-proton collisions at $\sqrt{s} = 7$ TeV recorded in 2010 with the ATLAS detector*, Eur. Phys. J. **C73** (2013) 2306, arXiv:1210.6210 [hep-ex].

[46] ATLAS Collaboration, *Performance of Missing Transverse Momentum Reconstruction in ATLAS studied in Proton-Proton Collisions recorded in 2012 at $\sqrt{s}$=8 TeV*, ATLAS-CONF-2013-082. https://cds.cern.ch/record/1570993.

[47] ATLAS Collaboration, *Performance of Impact Parameter-Based b-tagging Algorithm with the ATLAS Detector using Proton-Proton Collisions at $\sqrt{s} = 7$ TeV*, ATLAS-CONF-2010-091. https://cds.cern.ch/record/1299106.

[48] ATLAS Collaboration, *Performance of the ATLAS Secondary Vertex b-tagging Algorithm in 7 TeV Collision Data*, ATLAS-CONF-2010-042. https://cds.cern.ch/record/1277682.

[49] G. Piacquadio and C. Weiser, *A new inclusive secondary vertex algorithm for b-jet tagging in ATLAS*, J. Phys.: Conf. Ser. **119** (2008) 032032.

[50] ATLAS Collaboration, *Calibration of b-tagging using dileptonic top pair events in a combinatorial likelihood approach with the ATLAS experiment*, ATLAS-CONF-2014-004. https://cds.cern.ch/record/1664335.

[51] ATLAS Collaboration, *Measurement of the Mistag Rate of b-tagging algorithms with 5 fb^{-1} of Data Collected by the ATLAS Detector*, ATLAS-CONF-2012-040. https://cds.cern.ch/record/1435194.

[52] E. Accomando, A. Ballestrero, A. Belhouari, and E. Maina, *Isolating vector boson scattering at the CERN LHC: Gauge cancellations and the equivalent vector boson approximation versus complete calculations*, Phys. Rev. **D74** (2006) 073010.

[53] T. Gleisberg, S. Höche, F. Krauss, M. Schönherr, S. Schumann, F. Siegert, and J. Winter, *Event generation with SHERPA 1.1*, J. High Energy Phys. **02** (2009) 007.

[54] T. Gleisberg and S. Höche, *Comix, a new matrix element generator*, J. High Energy Phys. **12** (2008) 039.

[55] S. Schumann and F. Krauss, *A parton shower algorithm based on Catani-Seymour dipole factorisation*, J. High Energy Phys. **03** (2008) 038.

[56] S. Höche, F. Krauss, S. Schumann, and F. Siegert, *QCD matrix elements and truncated showers*, J. High Energy Phys. **05** (2009) 053.

[57] ATLAS Collaboration, *Improved luminosity determination in pp collisions at $\sqrt{s} = 7$ TeV using the ATLAS detector at the LHC*, Eur. Phys. J. **C73** (2013) 2518.

[58] S. Agostinelli *et al.*, GEANT4 - *a simulation toolkit*, Nuclear Instruments and Methods in Physics Research Section A **506** (2003) 250–303.

[59] T. Sjöstrand, S. Mrenna, and P Skands, *PYTHIA 6.4 Physics and Manual*, JHEP **0605** (2006) 026.

[60] T. Sjöstrand, S. Mrenna, and P Skands, *A brief introduction to PYTHIA 8.1*, Comput. Phys. Comm. **178** (2008) 852–867.

[61] S. Hoeche, F. Krauss, S. Schumann, and F. Siegert, *QCD matrix elements and truncated showers*, JHEP **0905** (2009) 053.

[62] H.-L. Lai, M. Guzzi, J. Huston, Z. Li, P. M. Nadolsky, J. Pumplin, and C.-P. Yuan, *New parton distributions for collider physics*, Phys. Rev. **D82** (2010) 074024.

[63] P. Nason, *A New Method for Combining NLO QCD with Shower Monte Carlo Algorithms*, JHEP **0411** (2004) 040.

[64] S. Frixione, P. Nason, and C. Oleari, *Matching NLO QCD computations with Parton Shower simulations: the POWHEG method*, JHEP **11** (2007) 070.

[65] S. Alioli, P. Nason, C. Oleari, and E. Re, *A general framework for implementing NLO calculations in shower Monte Carlo programs: the POWHEG BOX*, JHEP **1006** (2010) 043.

[66] B. Jäger, C. Oleari, and D. Zeppenfeld, *Next-to-leading order QCD corrections to W^+W^+jj and W^-W^-jj production via weak-boson fusion*, Phys. Rev. **D80** (2009) 034022.

[67] B. Jäger and G. Zanderighi, *NLO corrections to electroweak and QCD production of W^+W^+ plus two jets in the POWHEG BOX*, JHEP **11** (2011) 055.

[68] T. Melia, K. Melnikov, R. Rontsch, and G. Zanderighi, *Next-to-leading order QCD predictions for W^+W^+jj production at the LHC*, JHEP **12** (2010) 053.

[69] T. Melia, P. Nason, R. Rontsch, and G. Zanderighi, *W^+W^+ plus dijet production in the POWHEG BOX*, Eur. Phys. J. **C71** (2011) 1670.

[70] K. Arnold *et al.*, *VBFNLO: A parton level Monte Carlo for processes with electroweak bosons*, Comput. Phys. Commun. **180** (2009) 1661–1670.

[71] J. Baglio *et al.*, *VBFNLO: A parton level Monte Carlo for processes with electroweak bosons – Manual for Version 2.7.0*, arXiv:1107.4038 [hep-ph].

[72] K. Arnold *et al.*, *Release Note – Vbfnlo-2.6.0*, arXiv:1207.4975 [hep-ph].

[73] *Rivet code for acceptance calculation in 8 TeV $W^\pm W^\pm jj$ analysis*, https://svnweb.cern.ch/trac/atlasphys/browser/Physics/StandardModel/ElectroWeak/Development/VBSWW/Generators/Rivet/MC_VBSVAL.

[74] ATLAS Collaboration, *Jet energy measurement with the ATLAS detector in proton-proton collisions at $\sqrt{s} = 7$ TeV*, Eur. Phys. J. **C73** (2013) 2304, arXiv:1112.6426 [hep-ex].

[75] *Data Preparation Checklist for Physics Analysis*, https://twiki.cern.ch/Atlas/DataPreparationCheckListForPhysicsAnalysis.

[76] M. Bahr *et al.*, *Herwig++ Physics and Manual*, Eur. Phys. J. **C58** (2008) 639–707, arXiv:0803.0883 [hep-ph].

[77] A. Martin, W. Stirling, R. Thorne, and G. Watt, *Parton distributions for the LHC*, Eur. Phys. J. **C63** (2009) 189–285, arXiv:0901.0002 [hep-ph].

[78] A. Martin, W. Stirling, R. Thorne, and G. Watt, *Uncertainties on α_S in global PDF analyses and implications for predicted hadronic cross sections*, Eur. Phys. J.**C64** 653–680, arXiv:0905.3531 [hep-ph].

[79] A. Martin, W. Stirling, R. Thorne, and G. Watt, *Heavy-quark mass dependence in global PDF analyses and 3- and 4-flavour parton distributions*, Eur. Phys. J.**C70** 51–72, arXiv:1007.2624 [hep-ph].

[80] J. Alwall *et al.*, *The automated computation of tree-level and next-to-leading order differential cross sections, and their matching to parton shower simulations*, JHEP **07** (2014) 079, arXiv:arXiv:1405.0301 [hep-ph].

[81] M. Mangano, M. Moretti, F. Piccinini, R. Pittau, and A. Polosa, *ALPGEN, a generator for hard multiparton processes in hadronic collisions*, JHEP **0307** (2003) 001, arXiv:hep-ph/0206293.

[82] M. Mangano, M. Moretti, and R. Pittau, *Multijet matrix elements and shower evolution in hadronic collisions: $Wb\bar{b} + n$ jets as a case study*, Nucl. Phys. **B632** (2002) 343–362, arXiv:hep-ph/0108069.

[83] F. Caravaglios, M. Mangano, M. Moretti, and R. Pittau, *A new approach to multi-jet calculations in hadron collisions*, Nucl. Phys. **B539** (1999) 215–232, arXiv:hep-ph/9807570.

[84] G. Cowan, K. Cranmer, E. Gross, and O. Vitells, *Asymptotic formulae for likelihood-based tests of new physics*, Eur. Phys. J. **C71** (2011) 1554, arXiv:1007.1727.

[85] G. Cowan, K. Cranmer, E. Gross, and O. Vitells, *Asymptotic distribution for two-sided tests with lower and upper boundaries on the parameter of interest*, arXiv:1210.6948.

[86] W. Kilian, T. Ohl, and J. Reuter, *WHIZARD: Simulating Multi-Particle Processes at LHC and ILC*, Eur. Phys. J. **C71** (2011) 1742, arXiv:0708.4233 [hep-ph].

[87] M. Moretti, T. Ohl, and J. Reuter, *O'Mega: An Optimizing Matrix Element Generator*, arXiv:hep-ph/0102195.

[88] ATLAS Collaboration, *Evidence for Electroweak Production of $W^{\pm}W^{\pm}jj$ in pp Collisions at $\sqrt{s} = 8$ TeV with the ATLAS Detector* , Phys. Rev. Lett. **113** (2014) 141803, arXiv:1405.6241 [hep-ex].

[89] T. Han, D. Krohn, L.-T. Wang, and Z. Wenhan, *New Physics Signals in Longitudinal Gauge Boson Scattering at the LHC*, JHEP **03** (2010) 082, arXiv:0911.3656 [hep-ph].